Università di Genova

PhD PROGRAM
SECURITY
RISK
VULNERABILITY

Doctoral Dissertation
Doctoral Program in Security, Risk and Vulnerability
Risk, Climate Change and Sustainable Development Curriculum (XXXVIII cycle)

Understanding Extreme Weather in a Warming European-Mediterranean Region: From Localized Convection to Organized Cyclones

By

Lisa Bernini

******

Supervisors:
Dr. A. Parodi, CIMA Research Foundation
Prof. C. Pasquero, University of Milan-Bicocca

Doctoral Examination Committee:
Dr. V. Kotroni, Referee, National Observatory of Athens
Prof. M. M. Miglietta, Referee, Institute of Atmospheric Sciences and Climate

University of Genoa
2026

Finanziato dall'Unione europea NextGenerationEU
Ministero dell'Università e della Ricerca
Italiadomani
PIANO NAZIONALE DI RIPRESA E RESILIENZA

Declaration

I hereby declare that, the contents and organization of this dissertation constitute my own original work and does not compromise in any way the rights of third parties, including those relating to the security of personal data.

Lisa Bernini
2026

* This dissertation is presented in partial fulfillment of the requirements for **Ph.D. degree** in the University of Genoa (UniGe).

Je dédie cette thèse à mes parents qui m'ont donné le courage, la force, la résilience, le support émotionnel et matériel, et l'enthousiasme pour mener à bien ce projet.

Acknowledgements

This doctoral scholarship was co-funded by European Union resources - NextGeneration EU with the Italian program "Piano Nazionale di Ripresa e Resilienza (PNRR), Missione 4, componente 2 (“Dalla Ricerca all’Impresa”)". The other co-funder of this thesis was the CIMA Research Foundation (Italy), to which I extend my sincere gratitude for the financial support and for access to material resources and professional expertise.

During my Ph.D., I was a visiting student at the Department of Earth and Environmental Sciences of the University of Milano-Bicocca (Italy) and at the Institute of Meteorology of the Free University of Berlin (Germany). I am grateful to both institutions for their hospitality and for the administrative and logistical support that made these research stays possible.

Beyond these institutional acknowledgments, I would like to express my deepest gratitude to my supervisors, Dr. A. Parodi (CIMA Research Foundation) and Prof. C. Pasquero (University of Milano-Bicocca). Their guidance and constant support over the past four years have been invaluable, and I am deeply appreciative of their mentorship and the trust they placed in me throughout this journey.

I am grateful to Dr. V. Kotroni (National Observatory of Athens) and Prof. M. M. Miglietta (Italian National Research Council) for agreeing to serve as reviewers and for their time and effort in evaluating this work.

I warmly thank my colleagues from the Meteorology and Climate Department of the CIMA Research Foundation and from the OCCAM group at the University of Milano-Bicocca. I am grateful for their helpful advice, constructive feedback, collaborative spirit, and, ultimately, for their kindness and friendship, which made the daily work both enriching and enjoyable.

I would also like to give special thanks to Dr. S. Pfahl (Free University of Berlin) and his research group for hosting me for six months at their institute. I am particularly grateful to Dr Pfahl for his insightful ideas and valuable advice, as well as to his team for the welcoming atmosphere and the stimulating scientific discussions.

Finally, I would like to give my deepest thanks to my family and my friends for the joy, laughter, tears, hugs, screams, songs, silence, endless discussions, *gelati al pistacchio*, and soap bubbles that helped me through this major step in my life. Your love and friendship are what make my life beautiful. Thank you <3

Abstract

Extreme precipitation and high-impact cyclones represent some of the most damaging manifestations of climate variability within the European–Mediterranean region. While driven by global thermodynamic trends, the impacts of these events are governed by atmospheric processes spanning a broad range of spatial and temporal scales. This thesis investigates convective extremes by integrating high-resolution, convection-permitting regional climate modeling with large-scale reanalysis diagnostics. This dual approach characterizes both local precipitation dynamics and the synoptic environments conducive to intense Mediterranean cyclones.

The first part of this thesis evaluates extreme precipitation and its sensitivity to recent warming using a newly developed dataset: "Computational Hydrometeorology with Advanced Performance to Enhanced Realism" (CHAPTER). CHAPTER provides a high-resolution (3 km) dynamical downscaling of the ERA5 reanalysis over Europe and the Mediterranean basin, using the Weather Research and Forecasting (WRF) model. The added value of this dataset is rigorously validated against daily precipitation and near-surface temperature observations. This evaluation demonstrates that CHAPTER accurately reproduces observed climatological patterns and extremes, establishing a physically consistent foundation for investigating long-term trends.

Analysis of the simulation reveals a marked increase in precipitation extremes over recent decades. To interpret these shifts, a diagnostic framework was used to decompose trends into thermodynamic and dynamic contributions. On one hand, thermodynamic effects, directly driven by increased atmospheric moisture at warmer temperatures, produce a broadly positive and uniform signal. On the other hand, changes in convective dynamics, primarily linked to vertical motion, emerge as the primary driver of regional intensity and structure. Furthermore, the results highlight a critical coupling between land–atmosphere interactions and convective intensity mediated by surface moisture availability. In regions where soil moisture and marine moisture supply remain abundant, enhanced evaporation supports deeper convection, leading to increases in both mean seasonal precipitation and hourly extremes. Conversely, declining soil moisture levels limit surface evaporation, which is associated with a reduction in extreme hourly rainfall intensity.

The second part of the thesis examines Mediterranean cyclones, with particular emphasis on systems that develop a deep warm core. By comparing the large-scale environments of classical baroclinic cyclones, intense cold-core systems, and disturbances with a deep warm core, the analysis identifies the key factors favoring the development of tropical-like characteristics.

These include substantially higher potential intensity and weaker vertical wind shear. Enhanced potential intensity arises from the combined effect of elevated sea surface temperatures and strong upper-level intrusions that destabilize the atmospheric column.

Overall, this thesis builds on the central role of atmospheric dynamics in both convective processes and cyclone evolution to control extreme weather in the Euro-Mediterranean region. The present work underscores the importance of high-resolution modeling for understanding and anticipating climate-driven changes in extremes.

Contents

List of Figures

List of Tables

Chapter 1

Introduction

1.1 The European–Mediterranean Region in a Warming Climate

Due to their complex geography, climatic contrasts, and tectonic activity, Europe and the Mediterranean Basin (**fig. 1.1**) are highly exposed to a broad range of natural hazards that already exert significant environmental, economic, and societal impacts [7, 8].

Fig. 1.1 Political map of Europe and the Mediterranean basin. Source: GISGeography.com

Focusing on extreme weather events, floods regularly affect large river basins like the Danube, Po, and Nile deltas [9–11], as well as low-lying coastal zones prone to storm surges [12–14]. The region also faces powerful windstorms [15, 16] and intense Mediterranean cyclones that can bring torrential rain and destructive winds [17]. In northern and mountainous continental areas,

severe storms, heavy snowfalls, landslides, and avalanches remain significant threats [18, 19], while the Mediterranean basin is highly exposed to heatwaves [20], droughts [21], desertification [22], and wildfires [23]. Coastal erosion and soil degradation further endanger fragile ecosystems and densely populated coastlines across this diverse region [24, 25].

The consequences of these hazards extend beyond immediate physical damage, affecting agriculture, energy production, transportation networks, and public health systems [26]. However, the overall risk posed by these hazards is not determined by their physical occurrence alone. It is also shaped by exposure, like the presence of people, infrastructure, and assets in hazard-prone areas, and by vulnerability, which reflects the capacity of societies to anticipate, cope with, and recover from disasters [27, 28].

In the Mediterranean region, exposure to natural hazards is particularly high due to dense coastal populations: over 500 million people live along its shores [29]. Maritime transport is another key exposure factor: in 2022, the Mediterranean Sea accounted for approximately 20 % of global ocean traffic and 10 % of cargo shipping [30]. Moreover, the spatial distribution of essential facilities such as hospitals, ports, and power stations along the coast plays a major role in determining vulnerability patterns during emergencies [29]. Across Europe as a whole, exposure remains significant, with a population exceeding 740 million people [31], many of whom are concentrated in urban areas along river valleys or flood-prone plains [32]. Continental regions such as the Rhine corridor, the North Sea coast, and the Danube basin are particularly exposed due to high population densities, industrial facilities, and dense transport networks located in areas sensitive to flooding or extreme weather events [28, 33, 34].

Socioeconomic factors further amplify vulnerability [35–37]. Regions with limited financial resources often lack adequate civil protection and recovery capacities, resulting in greater losses when extreme events occur [38]. Age demographics also play a role: populations with large fractions of very young or elderly people are generally more susceptible to extreme weather impacts [39–41].

For example, rural areas in southern Italy and Sicily are characterised by low income, ageing populations and limited infrastructure, making them especially vulnerable to prolonged droughts or wild-fire exposure [35]. Similarly, regions such as inland Greece (e.g., Evrytania) and north-western Spain (e.g., Ourense) hold some of the highest proportions of elderly residents in Europe, compounding their sensitivity to heatwaves, floods, or service disruptions in emergencies [42, 43]. In addition, areas in southern and south-eastern Europe (including certain municipalities in Bulgaria, Croatia, Greece, and Portugal) are characterised by lower incomes, higher unemployment, and larger older-age shares, which means exposure to extreme heat and other hazards is more likely to result in negative health and economic outcomes [44]. Finally, transient and highly vulnerable migrant groups crossing the Mediterranean Sea or the English Channel face acute exposure to sea storms and extreme maritime conditions, with catastrophic human consequences during severe events [45, 46].

Taken together, these factors reveal that Europe and the Mediterranean Basin combine high hazard exposure with significant vulnerability and a dense concentration of assets, making them critical regions for assessing how extreme events translate into risk. Understanding this interplay is particularly urgent as the climate continues to warm, since both the frequency and intensity of many weather-related hazards are being reshaped by climate change worldwide [47].

Indeed, Europe and the Mediterranean are widely recognised as global warming hotspots, where the pace and magnitude of change exceed the global average. They are warming faster than the global mean, amplifying existing vulnerabilities and challenging adaptation capacity [48–50]. Over the past decades, average land temperatures in Europe have risen by approximately 2.1 °C relative to pre-industrial levels, which nearly double the global mean increase of 1.17 °C [51]. For the Mediterranean Sea, projections indicate a mean warming of 2–4 °C by mid-century [52], further intensifying regional climate contrasts and environmental stressors.

With global warming, many of the weather-related natural hazards in Europe and the wider Mediterranean Basin are expected to intensify. Rising air and sea temperatures will likely make heatwaves [53, 54], droughts [55], and wildfires [56] more frequent and severe, particularly in southern Europe, North Africa, and the Middle East. Although mean precipitation is projected to decrease, especially during summer, the intensity and frequency of high-impact rainfall events are expected to rise [57–59]. This will increase the risk of flash floods and landslides [60, 61]. Melting glaciers and permafrost in the Alps and other mountain ranges will continue to heighten the danger of floods, avalanches risks, and rockfalls [62–64], while the warmer Mediterranean Sea is projected to fuel stronger and more frequent intense cyclones [65, 66], producing heavy rainfall, flash floods, and coastal damage. Sea-level rise will exacerbate coastal flooding and erosion throughout the region [67–69], threatening major cities and tourism hubs. Although the direct link between global warming and the frequency of earthquakes or volcanic eruptions is hard to assess [70–72], it may indirectly influence geohazards through changes in land stability, soil moisture, and groundwater pressure [73].

Overall, global warming is projected to magnify the natural risks already present in the Mediterranean Basin and continental Europe, with profound and interconnected consequences for ecosystems, economies, and human well-being. These changes heighten the urgency of understanding the physical processes that govern extreme weather events, enabling the anticipation of their future evolution, improvement of predictive capabilities, and strengthening of the scientific basis for risk assessment and climate adaptation strategies across the region.

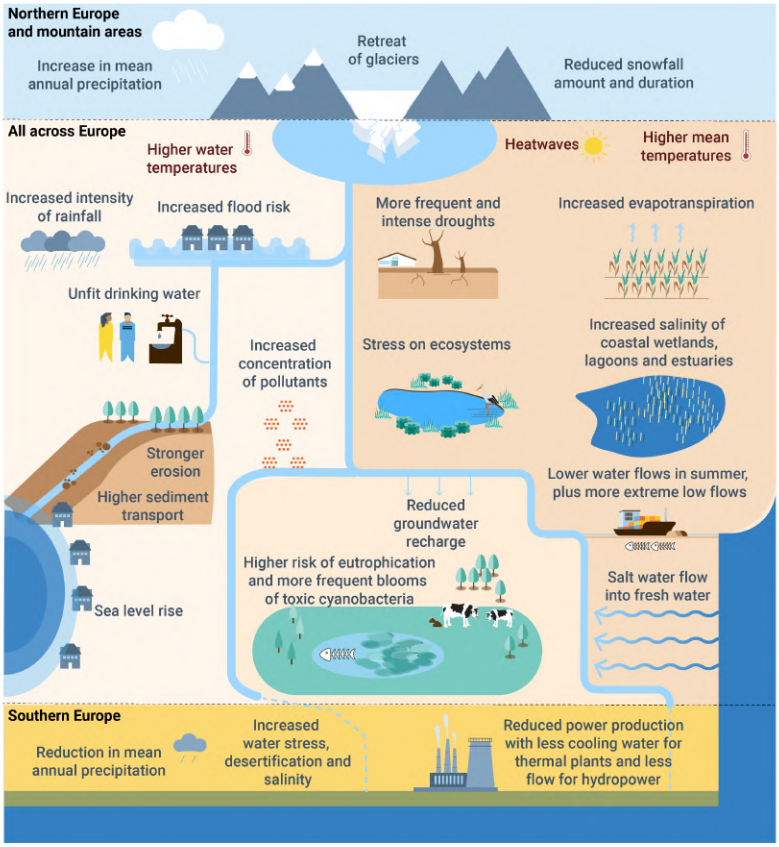

Fig. 1.2 Schematic of climate change impacts on the water cycle in Europe. Source: [1].

1.2 Atmospheric Convection and Its Role in Extreme Events

1.2.1 Convective Precipitation

Among the physical processes that control extreme weather events in the Mediterranean region, atmospheric convection is of particular importance. It plays a central role in the development of intense precipitation and storm systems, especially those occurring on local and mesoscale ranges.

Atmospheric convection is the vertical transport of air masses driven by buoyancy forces arising from unstable density stratification. Depending on its depth, convection can be classified as shallow, linked to cumulus clouds, or deep, associated with mesoscale systems and thunderstorms. Moist convection plays a fundamental role in the Earth's energy and water cycles, governing the vertical exchange of heat, momentum, and moisture between the surface and the free troposphere [74, 75].

A key concept for understanding the energy available for convection is moist static energy (MSE), which represents the sum of an air parcel's internal energy, potential energy, and latent heat due to water vapor. MSE is a conserved variable in moist adiabatic processes and is crucial

for assessing the potential for deep convection. Higher MSE values indicate greater energy available for convective development, especially in warm, humid environments.

Two other useful concepts for evaluating convective potential are convective available potential energy (CAPE) and convective inhibition (CIN). CAPE measures the integral of positive buoyancy that an air parcel would experience if lifted from a given level to its level of neutral buoyancy, effectively representing the potential energy for deep convection. MSE and CAPE are closely linked: as MSE increases, so does the likelihood of higher CAPE values, since both reflect the energy available to fuel convective updrafts. On the other hand, CIN quantifies the energy barrier that must be overcome for parcels to rise to levels where they become buoyant.

The combination of MSE, CAPE, CIN, ambient humidity, and triggering mechanisms, such as frontal lifting, orography, convergence, or cyclonic ascent, governs whether and how convection initiates and organizes. When these conditions favor the initiation and growth of convection, the resulting buoyant updrafts promote condensation and cloud formation, ultimately producing convective precipitation.

Such precipitation typically occurs in localized, short-lived bursts characterized by high rainfall rates, reflecting the concentrated nature of the ascending moist air. [5] showed that heavy convective precipitation is the most common severe weather type in Europe, with thunderstorms occurring frequently over mountain ranges such as the Alps, the Carpathians, and the Balkan Peninsula, as well as over the Mediterranean Sea itself. Despite their frequency, forecasting these events remains highly challenging, as convective development is modulated by the complex interactions mentioned previously.

1.2.2 Tropical-Like Cyclones

Beyond these local effects, organized convection can strongly influence the surrounding atmosphere and participate in the development of tropical-like cyclones. Thus, convection links small-scale storm dynamics with the evolution of larger-scale weather systems.

Tropical cyclones (TC) are intense rotating low-pressure systems that form over warm ocean waters and derive their energy primarily from the release of latent heat through deep moist convection [76]. They are fundamentally thermodynamic systems, maintained by a positive feedback between surface heat fluxes and convective updrafts. Warm sea surface temperatures (SST) promote evaporation and increase the moisture content of the lower atmosphere; when this moist air rises and condenses, the resulting latent heat release warms the core of the system, fostering a warm-core structure [77]. This process enhances pressure falls at the center [78], strengthening the cyclonic circulation and further sustaining convection. This feedback, called the wind induced surface heat exchange (WISHE; [79]) is illustrated **fig. 1.3**. However, tropical cyclones do not typically arise spontaneously: their development generally requires a pre-

existing large-scale disturbance, such as a synoptic-scale wave or trough, which provides the initial vorticity and convergence necessary to organize convection into a coherent system [80].

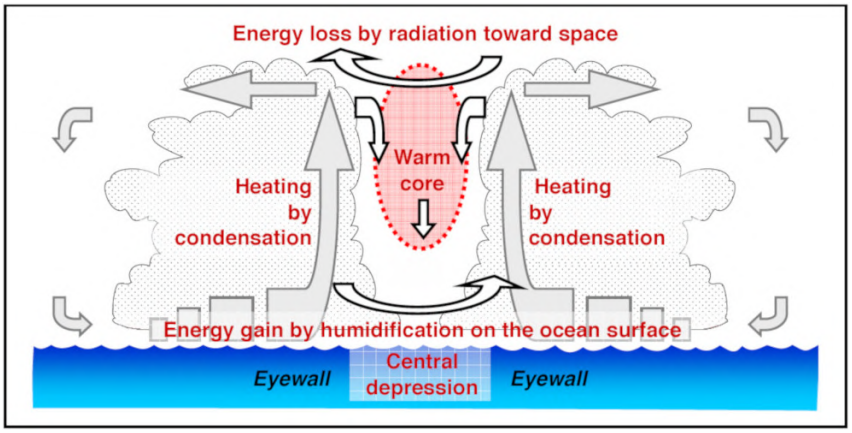

Fig. 1.3 Schematic of the thermodynamic cycle of a mature tropical cyclone. Source: [2].

In contrast to this convectively driven mechanism is the formation of extra-tropical cyclones (ETC). These systems are large-scale low-pressure disturbances that develop outside the tropics and are characterized by frontal structures and strong horizontal temperature gradients [81]. Their formation is closely tied to baroclinic instability, which occurs in the presence of pronounced temperature contrasts between air masses. This gradient generates density differences that favor the development of waves along the boundary between warm and cold air, which can then amplify and lead to cyclogenesis [82–84]. This formation process is illustrated **fig. 1.4**. Unlike tropical cyclones, ETC exhibit a cold-core structure and are typically asymmetric [85], reflecting their dependence on baroclinic processes rather than vertically aligned convection.

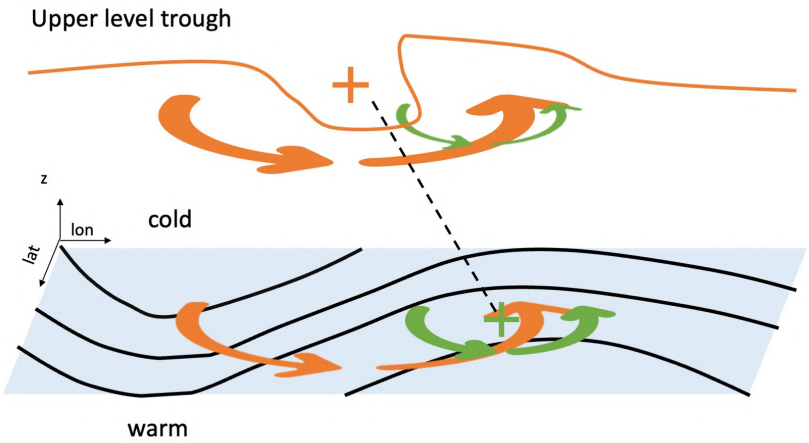

Fig. 1.4 Schematic of the interaction of upper and lower PV anomalies for extra-tropical cyclogenesis. The figure is an update of a schematic showing the arrival of an upper-level trough over a low-level baroclinic region (indicated by the black solid lines). The orange "plus" indicates the positive PV anomaly associated with the upper-level trough, and the orange arrows show the circulation associated with this anomaly. The green "plus" and arrow indicate the positive PV and circulation associated with the warm temperature anomaly induced by low-level advection. Source: Adapted from [3] by [4].

In the Mediterranean region, most cyclonic systems follow this extra-tropical paradigm. Baroclinic instability is often triggered by the meandering of the jet stream, which enhances the interaction between warm subtropical air and cooler mid-latitude air masses [86–88]. Furthermore, orography plays a crucial role in extra-tropical cyclogenesis: mountain ranges such as the Alps or the Atlas can deflect and channel airflow, intensify horizontal temperature contrasts, and generate localized vorticity. These effects make certain areas more prone to cyclone development, as the terrain acts both as a barrier and a catalyst for atmospheric instabilities [89–91].

While the majority of Mediterranean cyclogenesis is driven by classical baroclinic instability, a subset of systems evolves beyond the typical extra-tropical structure to exhibit characteristics remarkably similar to tropical cyclones. These systems are referred to as Mediterranean tropical-like cyclones (MTLC), or Medicanes, a portmanteau of Mediterranean Hurricanes. They occupy an intermediate position along the continuum between pure extra-tropical and pure tropical systems. In their mature stage, they often display a deep warm core, an axisymmetric cloud structure, and a distinct, cloud-free center surrounded by a primary eyewall of deep convection and intense winds [87, 92]. Despite the restricted fetch of the Mediterranean, these cyclones can be particularly destructive, with peak wind speeds occasionally reaching the equivalent of Category 1 on the Saffir–Simpson scale [93].

Although MTLC share many morphological features with TC, they emerge under significantly different environmental constraints. Most notably, they form over much colder sea surface temperatures [92, 94], and while TC are primarily maintained by thermodynamic air-sea interactions, MTLC develop in environments where baroclinic disturbances play a more prominent and sustained role. They typically arise from conventional extratropical cyclones, often triggered by the intrusion of an upper-level Potential Vorticity (PV) streamer into the basin [95, 96]. This initial baroclinic forcing provides the dynamic ascent necessary to initiate deep, organized convection within the disturbance.

The evolution of a Medicane is thus best understood through the paradigm of tropical transition (TT). Formalized by [97, 98] and supported by global climatologies [99, 100], the TT framework describes the process by which an initially cold-core, baroclinic cyclone progressively transforms into a warm-core system. As organized convection develops, the associated latent heat release begins to modify the system's thermal structure. Under favorable conditions, diabatic processes become increasingly dominant, and the system transitions toward a state maintained by the WISHE mechanism [79] rather than by horizontal temperature gradients.

This paradigm emphasizes the physical continuity between baroclinic cyclogenesis and tropical development. It acknowledges that while most tropical systems—including classical TC—benefit from an initial baroclinic "seed" or precursor disturbance to initiate, MTLC rely on a particularly robust and sustained baroclinic "kickstart" to overcome the thermodynamic inhibitions of the Mediterranean environment. In this sense, MTLC represent a specific regional manifestation of the TT process, where strong synoptic-scale forcing compensates for the lack of the high-energy tropical environments typically associated with TC formation.

1.2.3 Convective Precipitation and Cyclones-Related Hazards

Convective storms and tropical-like cyclones, despite their differences in spatial and temporal scales, expose affected regions to a broadly similar spectrum of hydrometeorological hazards. Both types of systems can generate intense precipitation capable of producing destructive floods, including rapidly developing flash floods in small, responsive catchments [101, 102]. The ensuing hydrological impacts depend on a combination of basin morphology, antecedent soil moisture, infiltration properties, and land-use patterns [103–105], while urbanization or fire-altered soils can further enhance surface runoff and aggravate flood severity. The same heavy rainfall can destabilize slopes, promoting shallow landslides or debris flows, particularly where the terrain is steep or soils are already saturated.

Electrically active storm environments in both mesoscale convective systems and cyclone-like vortices produce frequent lightning, which poses direct threats to life and infrastructure and, under sufficiently dry surface conditions, can ignite wildfires [17]. Strong winds represent another shared hazard: whether arising from localized convective downbursts or the broader circulation of a tropical-like cyclone, high wind speeds can uproot vegetation, damage buildings, and create airborne debris that amplifies other impacts [106, 107]. These winds frequently support large wave development over open water, with wave heights capable of endangering vessels and eroding coastal structures [108].

Coastal areas are additionally vulnerable when wind-driven waves coincide with storm-induced rises in sea level. Such conditions can lead to compound coastal flooding and geomorphological change, including beach erosion and, in some cases, slope failures near the shoreline [61]. In conjunction with wind and precipitation extremes, the turbulent, dust-laden inflows sometimes associated with these systems may facilitate the transport of fine particulates and increase respiratory health risks [17].

Together, these processes illustrate that both small-scale convective storms and larger tropical-like cyclones can produce an intertwined set of hazards summarized **fig. 1.5**: floods, landslides, windstorms, storm surge, waves, lightning, and even wildfires. The impacts of such hazards depend on environmental vulnerability as much as on the storms themselves. Their consequences are not merely physical: in recent decades, such events have recurrently affected the countries of the Euro-Mediterranean region, leading to loss of life, widespread environmental degradation, and economic damages amounting to billions of euros [109, 7, 110].

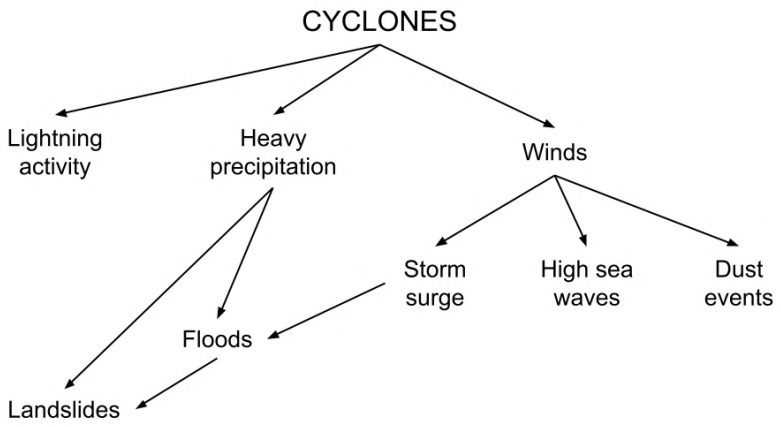

Fig. 1.5 Schematic of cyclone-induced hazards and their interactions.

1.3 Response of Convective Extremes to a Warming Climate

1.3.1 Projected changes in CAPE and CIN

The hazards associated with convective precipitation and tropical-like cyclones are intrinsically tied to the intensity and organization of atmospheric convection. Consequently, understanding the sensitivity of convective environments to anthropogenic warming is essential for assessing evolving risk profiles in the Euro-Mediterranean region. This evolution is governed by the interplay between increasing thermodynamic potential and tightening kinematic or structural constraints. Central to this response is the Clausius-Clapeyron relationship, which dictates that the saturation vapor pressure increases by approximately 7% per degree of warming. Under the assumption of quasi-constant relative humidity, this implies a commensurate increase in atmospheric moisture content [111], effectively raising the latent energy available for convective processes.

However, the vertical thermal structure of the convective atmosphere does not respond uniformly to this moisture increase. While traditional models have approximated the tropical and Mediterranean summer profiles using a moist-adiabatic lapse rate, this idealized framework fails to account for the persistent observation that the environment is often more unstable than a pure moist adiabat would suggest [112]. [113] demonstrated that this discrepancy arises from the entrainment of unsaturated environmental air into rising convective plumes. In their "zero-buoyancy" framework, the environmental temperature profile is determined by the requirement that a diluted, entraining plume (in opposition to an idealized, non-interacting parcel) remains neutrally buoyant relative to its surroundings.

In a warming climate, the resulting increase in the saturation deficit ($q_{sat} - q$) heightens the buoyancy reduction incurred during entrainment. Rising plumes experience more vigorous evaporative cooling as they entrain environmental air with a higher capacity for moisture absorp-

tion. To sustain neutral buoyancy under these conditions, the macro-scale environment must adjust toward a steeper vertical temperature gradient, characterized by colder temperatures aloft relative to the surface. Crucially, because the standard definition of the Convective Available Potential Energy (CAPE) is calculated based on a theoretical, non-entraining parcel that does not experience this evaporative cooling, it benefits fully from both the steeper lapse rate and increased boundary-layer moisture. This physical decoupling explains why CAPE is projected to increase significantly [114], often exceeding the rate suggested by Clausius-Clapeyron. This represents a shift toward a more energetically charged but structurally constrained convective environment.

In the Euro–Mediterranean sector, this thermodynamic potential is further modified by pronounced land–sea thermal contrasts. Land surfaces in this region are warming at a higher rate than the adjacent Mediterranean Sea and Atlantic Ocean [115, 116]. Because near-surface moisture over land is largely supplied by oceanic advection, surface specific humidity over land often fails to increase at the Clausius-Clapeyron rate [117, 118]. The resulting decline in near-surface relative humidity alters the surface energy balance, partitioning energy into stronger sensible heat fluxes. This process drives the development of a deeper, more turbulent planetary boundary layer (the lowest part of the atmosphere in direct contact with, and influenced by, the Earth's surface). This deepening of the mixed layer further reduces near-surface moisture through the entrainment of dry air from the free atmosphere above. Because the air near the ground is now warmer and drier, a rising air parcel must be lifted much higher before it cools sufficiently to reach saturation and condense into a cloud.

These factors collectively raise the lifting condensation level (LCL), significantly increasing the Convective Inhibition (CIN) that a parcel must overcome to reach its level of free convection. This culminates in a state of heightened convective latency: while a larger magnitude of buoyant energy accumulates as CAPE, it remains inaccessible to weak or moderate lifting mechanisms [119]. Consequently, warming in the Euro-Mediterranean region may lead to an atmosphere characterized by increased potential instability but reduced convective frequency, where the release of accumulated energy is restricted to scenarios involving sufficiently strong dynamical forcing.

1.3.2 Implications for convective storms and tropical-like cyclones

The thermodynamic environment described above has important implications for convective hazards. Although stronger CIN may limit the frequency of convective initiation, episodes in which this inhibition is overcome allow storms to access both enhanced CAPE and a moister atmosphere [111]. Consequently, once deep convection is triggered, storms have the potential to produce more intense rainfall rates [120].

Beyond its direct impact on precipitation efficiency, increased moisture also amplifies latent heat release during condensation, strengthening vertical updrafts and enhancing storm organi-

zation [121]. These feedbacks can accelerate storm dynamics, potentially leading to so-called "super-CC" scaling, in which precipitation intensity increases exceed the canonical 7% per degree warming predicted by thermodynamic considerations alone [122, 123]. Such behavior is particularly relevant for intense convective storms and tropical-like cyclones, where strong forcing mechanisms can unlock stored instability and convert it into extreme impacts.

These mechanisms provide a consistent explanation for observed and projected trends in the Euro-Mediterranean region: a decrease in mean precipitation, accompanied by an increase in extreme rainfall and high-impact thunderstorms [124–127]. A similar tendency is also observed for the future evolution of Mediterranean Tropical-Like Cyclones: a projected decrease in overall frequency, contrasted by an increase in intensity and hazardousness.

Regarding frequency, the reduction is driven by the changing vertical thermal structure of the atmosphere. In a warmed climate, the upper troposphere warms faster than the ocean, decreasing the mean temperature difference between the sea surface and the upper levels. While the frequency of cold anomalies in the high troposphere remains mostly unchanged, the shift in the mean temperature value implies that a significantly larger anomaly is required to reach the instability threshold necessary for genesis. Because such extreme anomalies are naturally less frequent, the probability of cyclone formation decreases [65, 128].

Conversely, regarding intensity, the tropical-like cyclones that do form in the late century in the Mediterranean Sea are expected to be substantially more hazardous. Projections indicate these storms will last longer and produce stronger winds and rainfall, developing a more robust, hurricane-like structure. This intensification is primarily confined to the autumn season, consistent with enhanced autumn SST warming. These higher SST positively influence the intensity of the cyclones through alterations of the surface energy flux, fueling more energetic and dangerous systems despite their reduced occurrence [66].

This interplay of reinforcing and counteracting factors means that, despite strong theoretical guidance, the overall evolution of extreme convective events in a warming climate remains far from trivial to assess. While some thermodynamic responses point robustly toward intensification, others modulate these tendencies depending on regional moisture availability and dynamic changes. Consequently, understanding how convective extremes will change with global warming demands integrated approaches that combine theory, observations, and high-resolution modeling [129–132].

1.4 Research Questions and Thesis Structure

The discussion above highlights that predicting the response of convective extremes to climate warming remains an open and scale-dependent problem. To address this challenge in the context of the European–Mediterranean region, this thesis adopts a multi-scale investigation. While

thermodynamic responses act globally, their manifestation varies drastically depending on the scale of the weather system, from the localized updrafts of a thunderstorm to the organized rotation of a Mediterranean cyclone. Consequently, this thesis utilizes high-resolution convection-permitting modeling to resolve fine-scale precipitation dynamics, alongside reanalysis data to characterize the synoptic environments of organized cyclones.

The overarching objective of this work is to characterize convective extremes in the European-Mediterranean region by examining both their internal dynamic drivers and their large-scale environmental precursors. To this end, the thesis addresses three specific research questions:

1. Can a convection-permitting dynamical downscaling accurately reproduce the statistics and spatial distribution of extreme precipitation events in the complex topography of the Euro-Mediterranean domain? (Addressed in Chapter 2)

2. How do thermodynamic constraints versus dynamic modulation contribute to observed changes in hourly extreme precipitation at the local scale? (Addressed in Chapter 3)

3. What are the specific large-scale environmental characteristics that distinguish the development of Mediterranean deep warm-core cyclones from standard cold-core baroclinic systems? (Addressed in Chapter 4)

The manuscript is structured into five chapters, organizing the research from methodological validation to localized event analysis, and finally to organized system analysis.

Chapter 2 lays the groundwork for analyzing fine-scale extremes. It presents the implementation and validation of a Convection-Permitting Model (CPM) run derived from dynamically downscaling the ERA5 reanalysis. Given the limitations of parameterized convection in capturing short-duration extremes, this chapter assesses the performance of the high-resolution simulation over the complex terrain and land-sea contrasts of the study domain.

Chapter 3 focuses on localized convection, utilizing the high-resolution dataset validated in the previous chapter. Here, the investigation centers on hourly extreme precipitation, a phenomenon intimately linked to explicit convective processes. By decomposing precipitation changes into thermodynamic (moisture-dependent) and dynamic (vertical velocity-dependent) components, this chapter isolates the drivers of intensity trends that coarser models might obscure.

Chapter 4 shifts the focus to organized cyclones, specifically Mediterranean Cyclones with tropical-like features. As these systems are governed by larger-scale environmental interactions, this study utilizes the ERA5 reanalysis to examine the synoptic and thermodynamic surroundings of these storms. This chapter characterizes the specific environmental ingredients that favor the development of a deep warm core in the Mediterranean Sea.

Chapter 5 synthesizes the main results of the thesis by integrating insights from the analysis of localized extreme precipitation using the convection-permitting model and from the reanalysis-

based study of organized cyclones. It first consolidates the key research findings, then discusses the scientific contributions and limitations of the work, and finally outlines perspectives for future research. Together, these sections aim to provide a cohesive and comprehensive understanding of extreme weather in the region.

Parts of the contents and figures of this thesis have already been published or submitted in the following articles:

Bernini, L., Lagasio, M., Milelli, M., Oberto, E., Parodi, A., Hachinger, S., ... & Tartaglione, N. (2025). Convection-permitting dynamical downscaling of ERA5 for Europe and the Mediterranean basin. *Quarterly Journal of the Royal Meteorological Society*, *151*(772), e5014.

Bernini, L., Cavicchia, L., Desbiolles, F., Scoccimarro, E., & Pasquero, C. (2026). Environmental characteristics associated with the development of deep warm core Mediterranean Cyclones. *Weather and Climate Dynamics*, *7*(1), 367-391.

Chapter 2

A Convection-Permitting Dynamical Downscaling of ERA5 for Extreme Event Analysis

2.1 Context and Significance

In response to the escalating challenges posed by extreme weather, there is a growing imperative to deepen our understanding of these phenomena through advanced modeling and analysis techniques [129–132]. One promising avenue is the development and use of convection-permitting regional climate models (CP-RCM), which operate at unprecedented spatial resolutions, typically under 4 km. This fine resolution enables more realistic simulations of local-scale weather systems and has led to clear improvements in reproducing extreme precipitation events, diurnal variability, spatial distribution, and intensity gradients compared to traditional climate models [133–135]. Moreover, CP-RCM capture surface heterogeneities with enhanced fidelity [136], including mountains [137], coastal regions [138], and urban areas [139]. They also represent land–atmosphere interactions more accurately, which is crucial for simulating extreme weather phenomena [140, 141].

Studying the evolution of convective processes under global warming remains difficult at the global scale because convection cannot be directly represented in global climate models. Their grid spacing is far larger than the typical scales of convective updrafts and downdrafts, making convection parameterization unavoidable and contributing to large inter-model spread [142]. In contrast, on regional domains, it is feasible to reach horizontal resolutions on the order of 4 km or finer, sufficient to explicitly resolve deep convection. CP-RCM therefore provide a physically consistent framework for investigating convective processes and their response to climate change, at a much lower computational cost than running convection-resolving simulations globally [135, 143].

In parallel, the advent of high-resolution climate reanalysis datasets has revolutionized our ability to reconstruct past weather conditions and monitor ongoing climate trends. By assimilating historical observations from diverse sources, these reanalysis products provide a comprehensive and consistent depiction of the atmospheric state, facilitating a deeper understanding of weather-related phenomena [144]. Notably, the European Centre for Medium-Range Weather Forecasts (ECMWF) has released ERA5, the fifth-generation global reanalysis dataset offering unprecedented spatial and temporal resolution [145]. In the present study, a dynamical downscaling of the ERA5 global reanalysis (31 km $\times$ 31 km grid) has been used. This downscaling, called Computational Hydrometeorology with Advanced Performance to Enhanced Realism (CHAPTER), has been made with the mesoscale numerical weather prediction model WRF-ARW [146] over Europe and the Mediterranean region on a grid of 3 km $\times$ 3 km from 1981 to 2022.

The availability of these meteorological fields at such high-spatial temporal resolution over the European continental scale is, to the author's best knowledge, currently unique in international climatological research. Different sub-continental reanalyses exist, as the European CORDEX domain (Coordinated Regional Downscaling EXperiment, cordex.org), COSMO-REA6 [147], the HIRLAM-based reanalysis [148], the Copernicus European Regional ReAnalysis (CERRA) datasets [149, 150], and MERIDA covering the Italian peninsula [26]. However, convection remains parameterized in these regional reanalyses due to the significant computational expenses associated with generating datasets at kilometer-scale grid resolution, especially for extensive domains. Convection-permitting resolution has thus far been attained solely for national or even smaller geographic areas. For example, MERA (Met Eireann ReAnalysis) covers Ireland and the United Kingdom with a horizontal resolution of 2.5 km [151], COSMO-REA2, a 2-km resolution dataset covers Central Europe [152], and finally, SPHERA [153, 154] and VHR-REA-IT [155] are two high-resolution downscaling of ERA5 at a 2.2 km grid scale level but only for Italy.

The domain of CHAPTER spans from the Atlantic Ocean to the Black Sea and from the Sahara desert to the southern regions of Scandinavia. With a dataset covering 42 years of data terrain-following model levels, CHAPTER offers a comprehensive resource for investigating the evolution, drivers, and impacts of extreme weather events at both local and regional scales over the past decades. Subsequent sections provide an overview of the model configuration and an assessment of CHAPTER's performance in accurately representing precipitation and temperature compared to state-of-the-art datasets.

2.2 Materials & Methods

2.2.1 Model configuration

The downscaling was performed using the numerical model WRF, with ERA5 data used as initial and boundary conditions. ERA5 is a state-of-the-art global climate reanalysis dataset developed

by ECMWF as part of the Copernicus Climate Change Service (C3S). This dataset represents the fifth generation of ECMWF reanalysis products, succeeding ERA-Interim. ERA5 offers significant advancements over its predecessor, ERA-Interim, boasting higher spatial and temporal resolutions, with grid resolutions of approximately 31 kilometers and temporal resolutions of 1 hour. It incorporates a wealth of observational data, including ozone-sensitive infrared radiance and reprocessed datasets not utilized in previous versions. The data assimilation system of ERA5 is based on Cycle 41r2 of the Integrated Forecast System, operating within 12-hour time windows. Released in 2017, ERA5 provides comprehensive coverage from 1940 to the present, continuously updated with a 2-month delay.

ERA5 data were retrieved with an hourly temporal resolution for CHAPTER computation to ensure good temporal consistency. They served as initial and boundary conditions for the model runs. The computational domains consist of 2 grids with a horizontal resolution of 9 km (30W-52E, 14N-65N, 716x634x50 grid points) and 3 km (20W-42E, 23.5N-60N, 1640x1352x50 grid points), respectively (**Figure 2.1**). For each day, the WRF model is initialized at 1800 UTC and integrated for 30 h. The first 6 h of each simulation are considered as spin-up time and are therefore discarded, so that only the remaining 24 h are retained for the analysis. Consequently, each run provides a continuous 24 h period from 0000 UTC to 2400 UTC. Each new simulation is re-initialized from ERA5 after 30 h, making all daily runs independent from one another. This daily re-initialization from ERA5 prevents the simulated fields from drifting away from the large-scale atmospheric conditions of the reanalysis and explains why spectral nudging was not applied.

The WRF version used is 4.1.1. The model physical setup is derived to a large extent from [133] and [156] studies with finer grid spacing (from 4 to 3 km), very well suited for severe weather phenomena dynamical downscaling, and covers a significantly larger area than those previous works. In particular, the Yonsei University scheme [157] is chosen for the planetary boundary layer turbulence closure; the RRTMG shortwave and longwave schemes are used for radiation [158–160]; and the Rapid Update Cycle scheme is chosen as a multi-level soil model (6 levels) with higher resolution in the upper soil layer: 0, 5, 20, 40, 160, and 300 cm [161, 162]. No cumulus scheme was activated in the innermost domains (d02) because the grid spacing allows the convection dynamics to be resolved. The convection scheme used in the outer domain (d01) is the New Simplified Arakawa–Schubert (NewSAS) scheme [163]. The NewSAS is a mass flux scheme based on [164] with revisions made to the entrainment and detrainment formulation following large-eddy simulation studies. The deep convection was made stronger by increasing the maximum allowable mass flux at the cloud base.

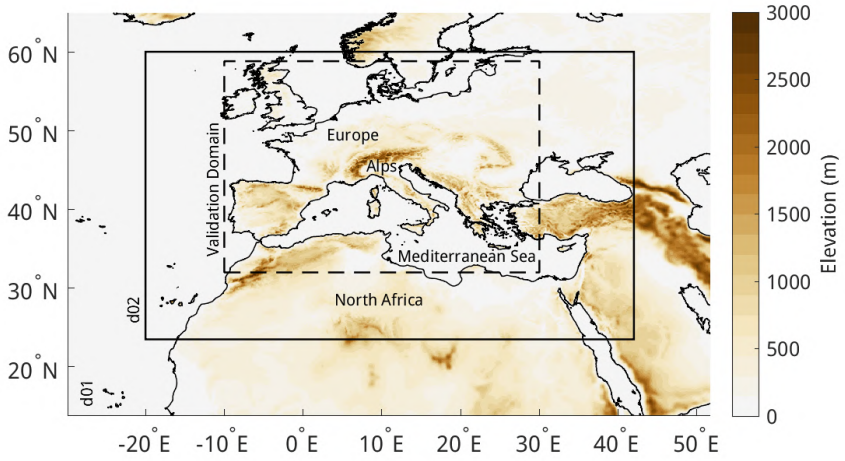

Fig. 2.1 Domain of the CHAPTER dataset with a resolution of 3 km by 3 km (entire graph) and domain used for the validation (internal black rectangle).

2.2.2 Validation

Observation datasets and comparative downscalings

The performances of CHAPTER have been evaluated on 24h precipitation accumulation and 2-m daily mean temperature. They are compared to the performance of the ERA5-Land reanalysis [165] and to the high-resolution precipitation dataset CHELSA [166]. The observation datasets used to confront the models' outputs are E-OBS [167], both for temperature and precipitation, and EURADCLIM [168], only for precipitation. A description of each dataset is provided hereafter. All the datasets are publicly available.

ERA5-Land is a refinement of ERA5, achieved through a process of physical downscaling. It utilizes high-resolution global numerical integration of the ECMWF land surface model, driven by meteorological data downscaled from ERA5 climate reanalysis. Notably, an elevation correction is applied to enhance the accuracy of near-surface thermodynamic conditions. While inheriting most parameterizations from ERA5, ERA5-Land distinguishes itself with a significantly improved horizontal resolution of $\sim$ 10 km ($0.1^\circ \times 0.1^\circ$) compared to ERA5's 31 km. Both datasets maintain an hourly temporal resolution. Evaluations against various independent datasets demonstrate ERA5-Land's performance in depicting the hydrological cycle [169].

CHELSA utilizes a statistical downscaling approach to enhance the resolution of daily precipitation estimates. This method integrates high-resolution satellite-derived cloud frequency data (30 arcsecs, approximately 1 km) with orographic predictors such as wind fields, valley exposition, and boundary layer height. The downscaling process involves bias correction to refine the results. By applying this approach to the ERA5 precipitation archive and MODIS monthly cloud cover frequency, a daily gridded precipitation time series in 1 km resolution from 2003 to 2016 is generated. Comparative analyses with existing datasets and station data, the Global

Historical Climatology Network daily [170], reveal improved spatio-temporal performance in precipitation prediction.

E-OBS is a daily gridded land-only observational dataset covering Europe at a horizontal resolution of 0.1° ($\sim$ 10 km), sourced from the European Climate Assessment & Dataset (ECA&D) project. This dataset includes precipitation amount, temperature, relative humidity, sea level pressure, and surface shortwave downwelling radiation. Initially developed for model validation, E-OBS is now widely used for climate monitoring, offering a unique combination of spatial resolution, daily resolution, and multiple variables. While valuable for climate research, E-OBS has limitations [171], including potential underestimation of precipitation and systematic errors, particularly for convective rainfall. In addition, the dataset's reliance on station data with varying densities across countries and variations in the 24-hour observation period highlights the need for careful interpretation [172].

Finally, EURADCLIM, the European climatological gauge-adjusted radar precipitation dataset, provides high-resolution, sub-daily precipitation estimates across Europe. Updated annually, it offers 1-hour and 24-hour precipitation accumulations at a 2-km spatial resolution for the 2013–2023 period. The dataset is constructed from EUMETNET OPERA gridded radar composites, which undergo rigorous filtering to remove non-meteorological echoes. These radar-based estimates are subsequently merged with rain gauge observations from ECA&D, a process that substantially improves the overall data quality [168]. Because of this dependency, the spatial coverage of EURADCLIM is strictly determined by the availability of the underlying OPERA data. As a result, the EURADCLIM domain is more limited than that of CHAPTER, particularly over Italy and, more generally, across large parts of the Mediterranean basin. Consequently, when EURADCLIM is used as a reference for evaluating CHAPTER precipitation performance, the analysis is restricted to the geographical areas common to both datasets.

Validation techniques

A fuzzy verification approach, as described by [173], is utilized to compare the precipitation performances of CHAPTER, CHELSA, and ERA5-Land. Unlike traditional nearest-point verifications, which seek exact matches between forecast and observation pairs, fuzzy verification methods relax matching conditions between the model and observations. In this approach, forecasts are required to be in approximate agreement with observations, considering factors such as proximity in space, time, or other quantities. This is particularly beneficial for high-resolution models where matching observations with absolute precision is challenging, as it mitigates "double-penalty" issues [174], where correct forecasting may still be penalized for being offset from observations. Moreover, due to the sparse nature of rain-gauge observations, a spatial aggregation is necessary to objectively assess the quality of model simulations and compensate for representativeness limitations that affect individual point observations.

This study adopted the "anywhere-in-the-window" fuzzy verification approach, as described by [173]. This is a special case of the “minimum coverage” technique, an example of the Neighbourhood Observation-Neighbourhood Forecast strategy. In particular, the Fraction Skill Score (FSS) serves as a primary index summarizing the potential of fuzzy verification logic, comparing forecast and observation fields within defined event areas. It is given by:

$$\mathrm{FSS} = 1 - \frac{\frac{1}{N}\sum_{i=1}^{N}(P_{mod,i} - P_{obs,i})^2}{\frac{1}{N}\sum_{i=1}^{N}P_{mod,i}^2 + \frac{1}{N}\sum_{i=1}^{N}P_{obs,i}^2} \tag{2.1}$$

with N the number of verification boxes in the domain under study and P the fraction of every single box in which the event occurs (the subscripts *mod* and *obs* stand for “forecast” and “observed”, respectively). The FSS ranges from 0 (complete disagreement) to 1 (perfect agreement). The FSS is equal to 0 if there are no expected events, but they do occur, or vice versa, if events that have been foreseen do not occur.

The FSS value above which the forecast is considered useful (better than the random data) is given by $FSS_{useful} = 0.5 + \frac{f_0}{2}$, where f_0 is the fraction of the domain covered by the observed event [175]. The smallest spatial window for which $FSS \geq FSS_{useful}$ is considered to be the useful scale. As the dimensions of the spatial windows increase, the index tends asymptotically to a value between 0 and 1. The closer this value is to 1, the less biased the forecast is.

Two other complementary scores are considered in this Fuzzy verification approach: the False Alarm Ratio (FAR) and the Probability Of Detection (POD). The FAR indicates the rate at which false detection occurs (range: 0–1, perfect value: 0). It is calculated as

$$\mathrm{FAR} = \frac{false\,alarms}{hits + false\,alarms} \tag{2.2}$$

The POD on the other hand is the rate at which real events are successfully detected (range: 0–1, perfect value: 1). It is given by:

$$\mathrm{POD} = \frac{hits}{hits + misses} \tag{2.3}$$

For precipitation, a last score is also computed but not following a fuzzy Fuzzy approach, the percent bias, defined as:

$$\mathrm{Percent\ \ Bias} = \frac{1}{N}\sum_{n=1}^{N}\frac{M_i - O_i}{O_i} \times 100 \tag{2.4}$$

with N the size of the sample data, M_i the model predictions and O_i the observations.

To compare the scores obtained by CHAPTER and CHELSA with respect to the EURADCLIM dataset (**Fig. 2.6 & 2.7**), CHAPTER, CHELSA and EURADCLIM have been regridded

thanks to a nearest neighbor remapping to a 3 km by 3 km regular grid. Because of the available period in EURADCLIM and CHELSA, this first comparison is made taking only into account the years from 2013 to 2016. In the same way, to obtain the scores by CHAPTER, CHELSA, and ERA5-Land computed with respect to E-OBS, all datasets have been regridded to a 10 km by 10 km regular grid, using a first order conservative remapping. For those datasets, the available period is from 2003 to 2016. Finally, for both analyses, to take into account the different spatial coverage, the validation domain retained is 10W-30E; 32N-58.8N (401 $\times$ 269 grid points, **Fig. 2.1**).

The same validation domain is used for temperature. Temperature fields have been validated by comparing the bias (or mean error) and the root-mean-square error (RMSE) obtained by CHAPTER and ERA5-Land in confront to E-OBS daily temperature.

$$\text{Bias} = \frac{1}{N}\sum_{n=1}^{N} M_i - O_i \tag{2.5}$$

$$\text{RMSE} = \sqrt{\frac{1}{N}\sum_{n=1}^{N} (M_i - O_i)^2} \tag{2.6}$$

Still with N the size of the sample data, M_i the model predictions and O_i the observations.

Again, the data of CHAPTER, ERA5-Land, and E-OBS have been re-gridded on the same 10 km by 10 km regular grid. For temperature, a correction with a constant lapse rate of 6.5 $K.km^{-1}$ has been applied to account for the differences in the elevation grid cells of the different datasets.

The seasonal means of the bias and the RMSE have been computed at each grid point and over the entire domain. A bootstrap technique [176] has been adopted to estimate the error of the global seasonal means. Each seasonal mean of the bias and the RMSE has been re-computed 1000 times each time, taking into account only 5% of all the data. The differences between the 97.5 percentile and the 2.5 percentile of this distribution of means, the boundaries of the 95% confidence interval, are the final errors present in **Tables 2.1 & 2.2**.

Finally, for both temperature and precipitation, the Added Value (AV) was computed as defined in [177] (range: -1 to 1; perfect value: 1):

$$AV = \frac{(X_{ERA5} - X_{E-OBS})^2 - (X_{CHAPTER} - X_{E-OBS})^2}{Max((X_{ERA5} - X_{E-OBS})^2, (X_{CHAPTER} - X_{E-OBS})^2)} \tag{2.7}$$

With X the spatial distribution of the considered variable.

The AV is a way of assessing where CHAPTER shows improvement over ERA5, taking E-OBS as the ground truth. Over the points where the AV is negative, ERA5 is more in agreement with E-OBS than CHAPTER. On the opposite, over the points where the AV is

positive, CHAPTER has generated added value in comparison to ERA5. For this last analysis, both E-OBS and CHAPTER have been upscaled at the resolution of ERA5, 31 km by 31 km.

2.3 Results

2.3.1 Precipitation

Bias

Figure 2.2 represents the seasonal spatial distribution of the percent bias of precipitation accumulation at 24 hours of ERA5-Land and CHAPTER enhanced on a 10 km by 10 km grid assuming E-OBS as reference. With respect to ERA5, CHAPTER has a higher positive bias, especially in summer over continental Europe. It is known that WRF simulations show a systematic positive precipitation bias and an overestimation of wet-day frequency [178]. In terms of spatial distribution, both datasets underestimate the precipitation over the African coast of the Mediterranean region, while the Alps are the main region where precipitation is overestimated. In both regions underestimation and overestimation are partially due to the low density of the E-OBS network.

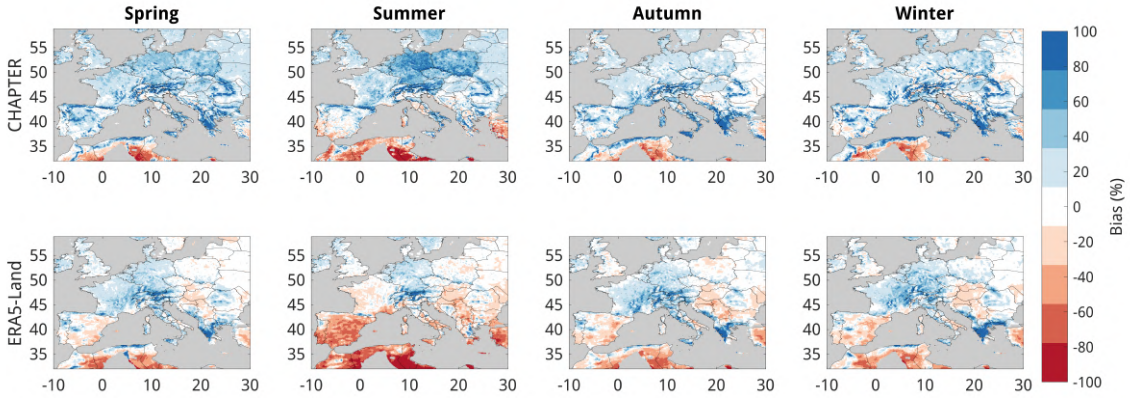

Fig. 2.2 Percent bias of the daily precipitation accumulation of CHAPTER (top) at 10 km and ERA5-Land (bottom) compared to E-OBS for the period 1981-2022.

Fuzzy Verification Scores

To have a more comprehensive view of the model's capability to represent precipitation fields, the FSS, FAR, and POD scores have been analyzed: a good performance corresponds to high FSS and POD values but low FAR values. In particular, the indices are shown as functions of spatial scale (abscissas) and precipitation threshold (ordinates), namely the dimension of the side of the verification box. In this way, by looking at the lower right corner of these charts, it is possible to assess the model performances for events characterized by small spatial scales and high intensity, which are of primary importance in developing strong convective events.

Therefore, eight thresholds of precipitation intensities are considered, namely, 0.5, 1.0, 2.0, 5.0, 8.0, 12.0, 16.0, and 20.0 mm per day. The agreements between the models and the observations are evaluated starting from a single grid pixel (i.e. 3 km by 3 km cells for the comparisons with the EURADCLIM dataset and 10km by 10 km cells for the comparisons with the E-OBS dataset) up to squares with 11 pixels (i.e. 33 km by 33 km cells for the comparisons with the EURADCLIM dataset and 110 km by 110 km cells for the comparisons with the E-OBS dataset).

For the comparison between the upscaled version of CHAPTER and CHELSA, and ERA5-Land, with E-OBS, considered as the ground truth, all datasets have better performance in autumn and winter. Both FSS scores (**Fig. 2.3**) and POD scores (**Fig. 2.5**) are high while the FAR scores (**Fig. 2.4**) are low, meaning true events are correctly represented and the ratio of non-existing events is low. For autumn and winter, the models are reliable for a spatial scale of 30 km and an intensity of 8 mm per day as indicated by the dots in **Fig. 2.3**. The worst scores are, however, found in summer, where the FSS and POD scores are low and the frequency of false detection increases. In summer, the reliable intensity decreases to 5 mm per day for a spatial scale of 30 km, meaning that strong localized convective events are more poorly represented.

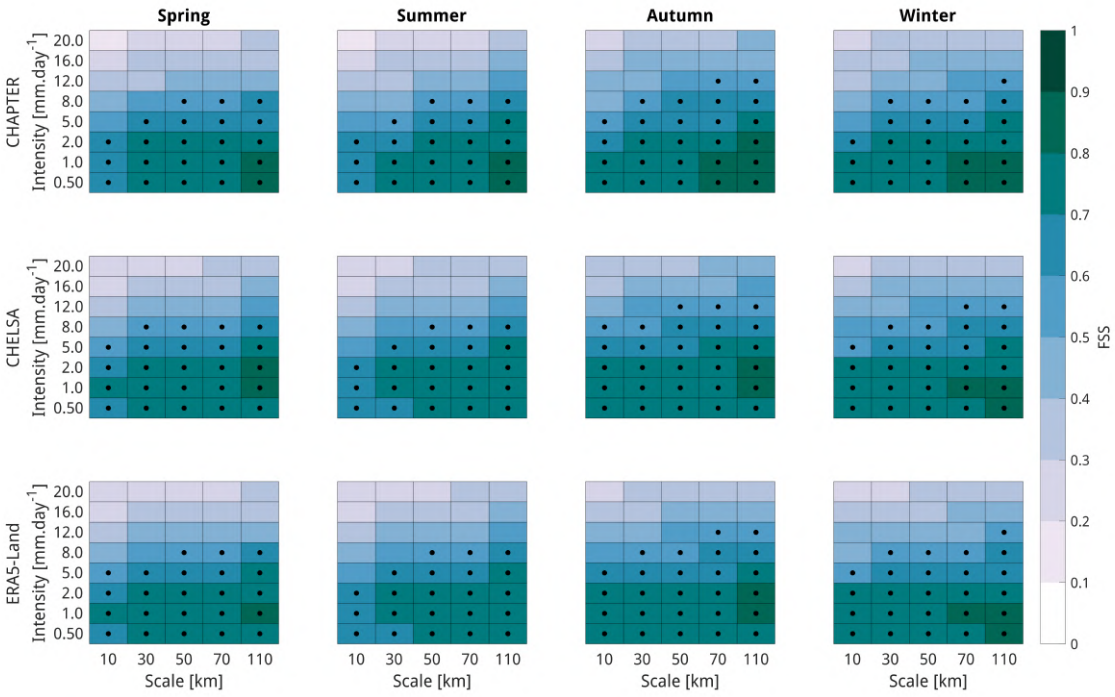

Fig. 2.3 Fraction Skill Score of the daily precipitation accumulation of CHAPTER (top) and CHELSA (center) at 10 km, and ERA5-Land (bottom) against E-OBS for the period 2003-2016. Black dots denote useful FSS values.

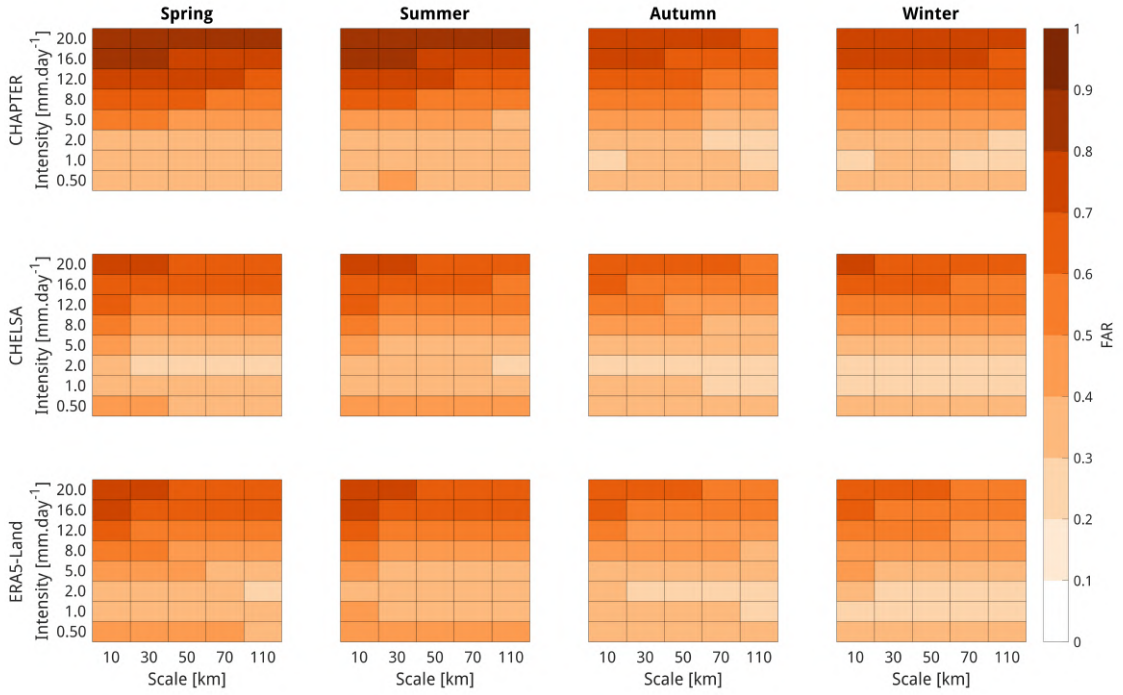

Fig. 2.4 False Alarm Ratio of the daily precipitation accumulation of CHAPTER (top) and CHELSA (center) at 10 km, and ERA5-Land (bottom) against E-OBS for the period 2003-2016.

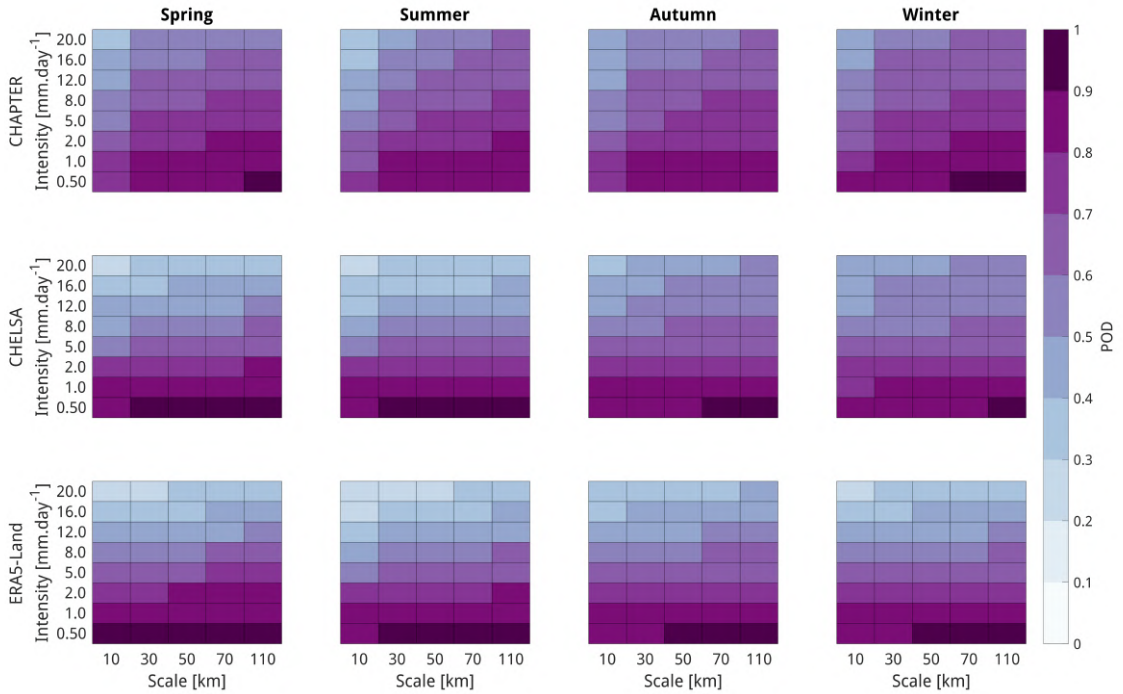

Fig. 2.5 Probability of Detection of the daily precipitation accumulation of CHAPTER (top) and CHELSA (center) at 10 km, and ERA5-Land (bottom) against E-OBS for the period 2003-2016.

CHAPTER performs very similarly to the two other datasets. Some differences can however be observed. In spring, for CHAPTER, the intensity of 5 mm per day at a scale of 10 km cannot be considered reliable while it is for the other datasets. As already mentioned in the previous part, the FAR scores also indicate that CHAPTER overestimates the strongest intensities ($\geq$ 16 mm per day) in spring and summer for every scale (**Fig. 2.4**). The high FAR scores at these scales are associated with higher POD scores for CHAPTER than for the other two datasets (**Fig. 2.5**). It shows that in general CHAPTER represents more strong convective events, increasing both probabilities of capturing events observed in E-OBS and events not present in the observation dataset.

Focusing on the comparison between CHAPTER and CHELSA with EURADCLIM at the native resolution of CHAPTER (3 km, **Fig. 2.6, 2.7**, and **2.8**) confirms the previous conclusions: CHAPTER can be reliable up to a scale of 10 km for precipitation intensities of 5 mm per day or 30 km for intensities of 8 mm per day (**fig. 2.6**). The main difference with CHELSA is in summer at a scale of 3 km where CHAPTER is not reliable for any of the intensities. However, it is worth mentioning that the mean difference between the scores of the two datasets is very low, around 0.02 points.

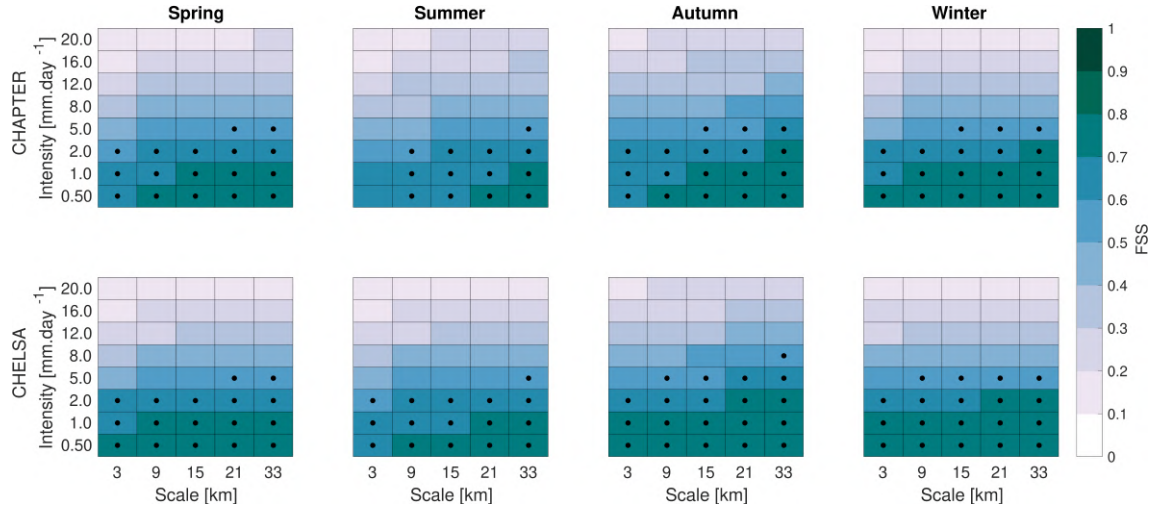

Fig. 2.6 Fraction Skill Score of the daily precipitation accumulation of CHAPTER (top) and CHELSA (bottom) against EURADCLIM for the period 2013-2016. All datasets are re-gridded on a regular grid of 3 km by 3 km. Black dots denote useful FSS values.

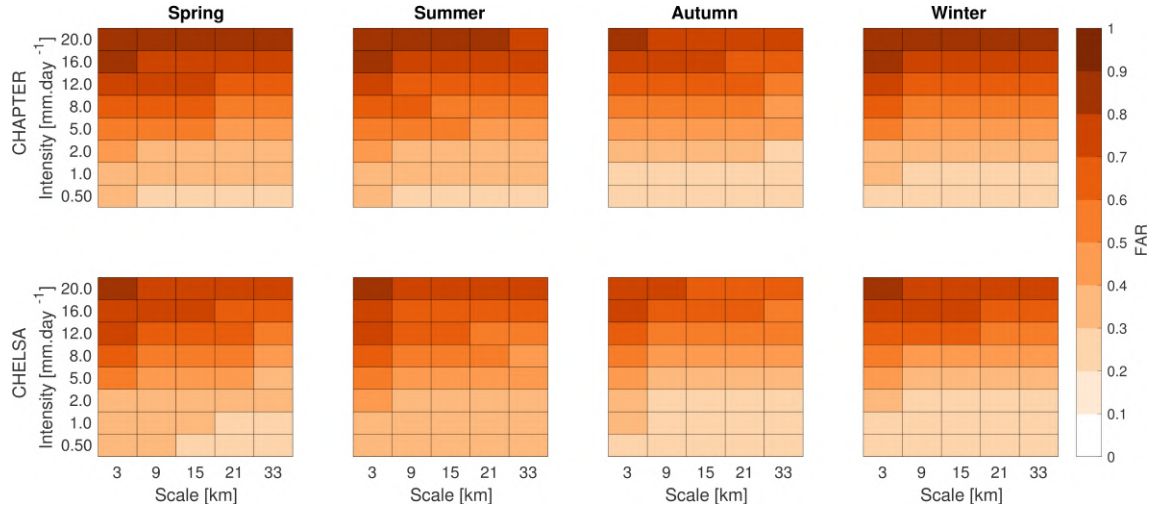

Fig. 2.7 False Alarm Ratio of the daily precipitation accumulation of CHAPTER (top) and CHELSA (bottom) against EURADCLIM for the period 2013-2016. All datasets are re-gridded on a regular grid of 3 km by 3 km.

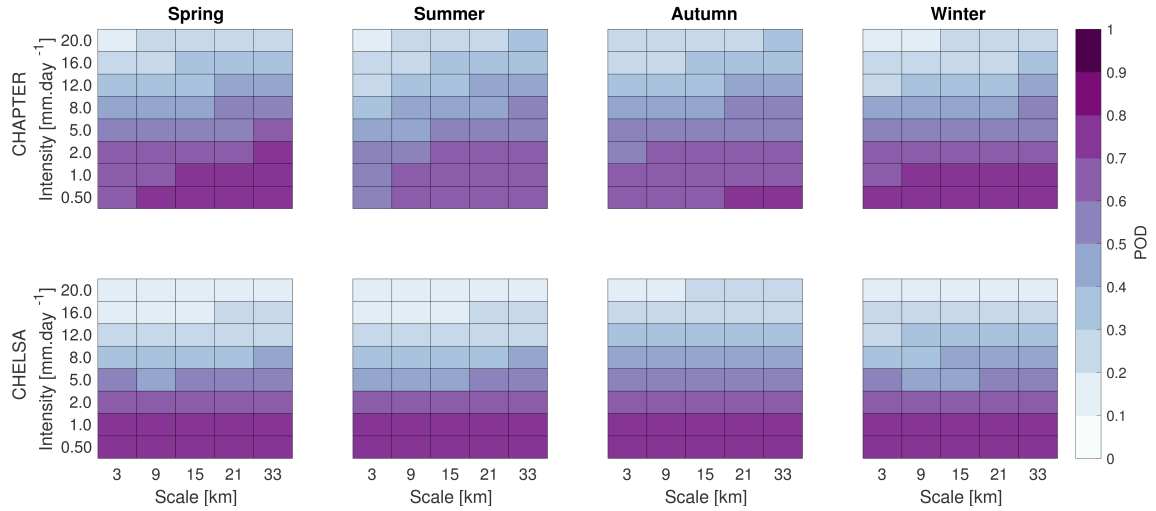

Fig. 2.8 Probability of Detection of the daily precipitation accumulation of CHAPTER (top) and CHELSA (bottom) against EURADCLIM for the period 2013-2016. All datasets are re-gridded on a regular grid of 3 km by 3 km.

2.3.2 Temperature

Figure 2.9 shows the evolution in the monthly mean 2m-temperature over all the validation domain of CHAPTER (upscaled at 10km), ERA5-Land, and E-OBS, for the whole period available in CHAPTER, i.e. 1981-2022. While ERA5-Land presents a systematic positive bias compared to E-OBS, CHAPTER seems to present a closer agreement with the observation dataset, with a slight negative bias starting after the year 1995 and a small positive bias before. Both datasets perfectly represent the evolution of the trends.

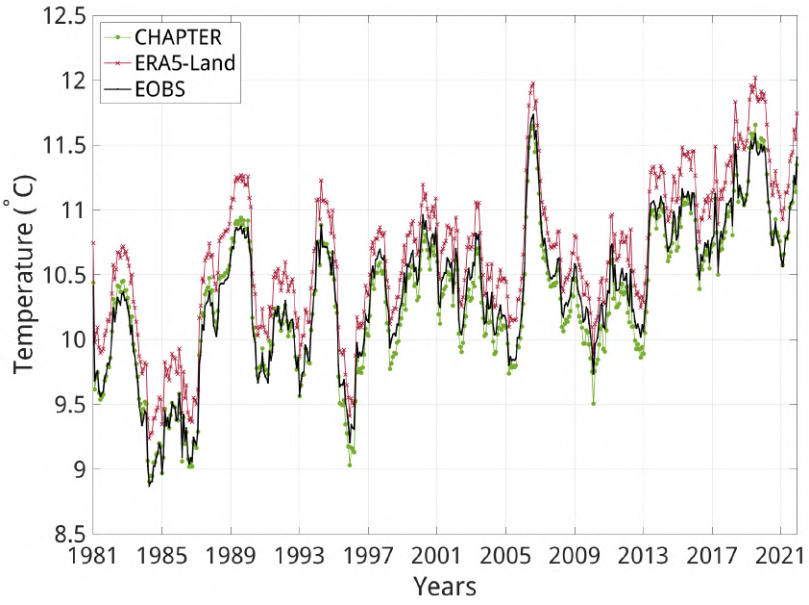

Fig. 2.9 Twelve-month running means of 2m temperature between 1981 and 2022 for E-OBS (black), ERA5-Land (red), and CHAPTER (green).

Table 2.1 presents the seasonal mean bias of temperature over all the domains, for the entire period. The positive bias in ERA5-Land mainly comes from the summer and autumn seasons while CHAPTER presents the strongest negative bias in winter. CHAPTER has both a positive bias in summer and a negative bias in winter, while ERA5-Land has only a strong positive bias in summer. This could explain why doing the running mean (**Fig. 2.9**) CHAPTER seems to have a closer agreement with the observations: the negative bias in winter compensates the positive one in summer.

Table 2.1 Mean bias of daily mean temperature of CHAPTER upscaled at 10 km and ERA5-Land temperatures for each season over all the domain (1981-2022). The units are in degrees Celsius.

	CHAPTER	ERA5-Land
Spring	0.02 ± 0.01	0.21 ± 0.01
Summer	0.55 ± 0.01	0.70 ± 0.01
Autumn	-0.02 ± 0.01	0.45 ± 0.01
Winter	-0.67 ± 0.01	-0.04 ± 0.01

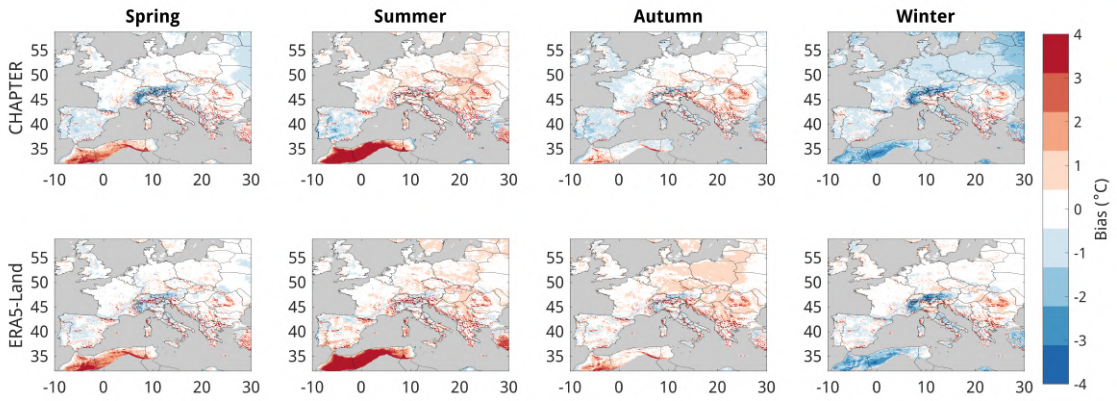

Fig. 2.10 Bias of the daily mean temperature of CHAPTER (top) at 10 km and ERA5-Land (bottom) compared to E-OBS for the period 1981-2022.

Looking at the mean bias for each location (**Fig. 2.10**), there is a clear overestimation of the temperature over the African coast. However, those large errors have perhaps more to do with the scarcity of data on this region than with the intrinsic deficiencies of the model. On another hand, the temperatures over the Alps are more frequently underestimated. It is important to note that over these two regions, the same errors are observed both for CHAPTER and for ERA5-Land, both in sign and magnitude.

Because of error compensation, the mean bias alone provides only partial information on model performance. The root mean square error (RMSE), shown in **Figure 2.11**, more accurately represents the magnitude of the average error, while giving greater weight to larger discrepancies. CHAPTER generally exhibits higher RMSE values than ERA5-Land, with a maximum seasonal mean RMSE of 2.18 °C in winter (**Tab. 2.2**). This confirms that CHAPTER tends to display slightly larger instantaneous differences relative to E-OBS; however, these errors largely compensate for each other both spatially and temporally, leading to a comparatively small annual mean bias. In contrast, ERA5-Land does not exhibit such seasonal compensation: it shows a pronounced positive bias in summer and only a weak negative bias in winter. As a result, the seasonal errors do not offset each other, yielding a larger discrepancy with E-OBS in the annual mean temperature. From a spatial perspective, the largest errors for both datasets are again found over North Africa and the Alpine region.

Table 2.2 Mean RMSE of the daily mean temperature of CHAPTER upscaled at 10 km and ERA5-Land temperatures for each season over the entire domain (1981-2022). The units are in degrees Celsius.

	CHAPTER	ERA5-Land
Spring	1.80 ± 0.02	1.64 ± 0.02
Summer	2.02 ± 0.02	2.04 ± 0.02
Autumn	1.66 ± 0.01	1.60 ± 0.01
Winter	2.18 ± 0.02	1.72 ± 0.01

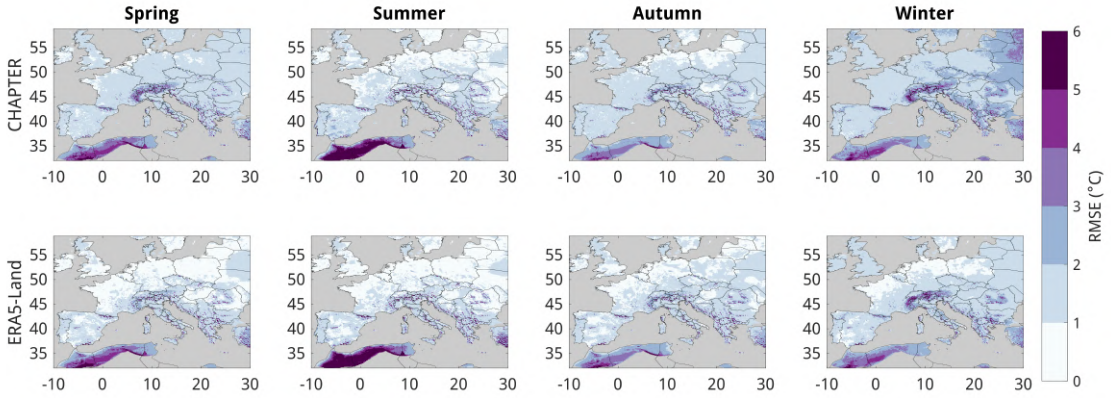

Fig. 2.11 RMSE of the daily mean temperature of CHAPTER (top) at 10 km and ERA5-Land (bottom) compared to E-OBS for the period 1981-2022.

2.3.3 Added Value of CHAPTER over ERA5

The preceding sub-sections focus on comparing CHAPTER with state-of-the-art downscaling of ERA5, one statistical and one dynamic. This section directly contrasts CHAPTER with ERA5 to evaluate the added value of CHAPTER. **Figure 2.12** illustrates the AV for temperature, where CHAPTER demonstrates a clear improvement. For nearly every grid cell across the domain and in all seasons, the AV is positive. In the case of precipitation (**fig. 2.13**), positive AV are observed over the plains of Central Europe during autumn, winter, and spring, whereas negative values occur in summer and over mountainous regions throughout all seasons. This indicates that during summer and in areas with complex orography, ERA5 aligns more closely with E-OBS.

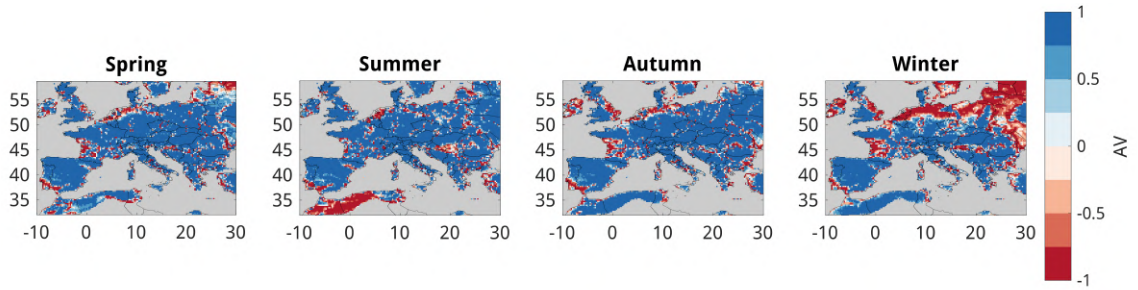

Fig. 2.12 Added Value (AV) for seasonal daily mean temperature (1981-2022) to assess the added value of CHAPTER over ERA5 when compared to E-OBS.

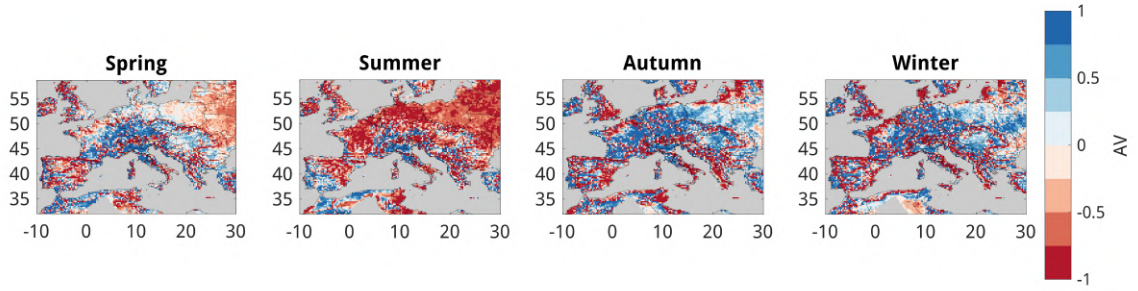

Fig. 2.13 Added Value (AV) for seasonal daily accumulated precipitation (1981-2022) to assess the added value of CHAPTER over ERA5 when compared to E-OBS.

The discrepancies between CHAPTER and E-OBS during summer or in specific regions may partly stem from E-OBS' inherent uncertainties. As highlighted in [172, 133, 179], the sparse distribution of measurement stations in certain regions leads to an effective resolution that is coarser than the nominal grid spacing, resulting in excessive smoothing of small-scale precipitation patterns. This smoothing effect is particularly pronounced in complex orographic regions such as the Alps and the Carpathians, where E-OBS tends to underestimate spatial contrasts in mean annual precipitation and systematically underestimates extreme rainfall rates due to the interpolation of coarse observations that miss or substantially dampen prominent heavy precipitation anomalies [172].

Since extreme precipitations are more frequently observed in summer, a season dominated by convective precipitation events [126, 127], such smoothing effects are expected to disproportionately affect this season. The ability of CHAPTER to better represent such events is supported by the PDF of annual daily mean precipitation (**fig. 2.14**): the tail of CHAPTER's distribution extends beyond those of E-OBS and ERA5. This contrast becomes even more evident when the PDF of EURADCLIM is considered (**fig. 2.15**), as EURADCLIM is available at a much higher resolution than E-OBS. In that case, CHAPTER's tail aligns more closely with EURADCLIM than ERA5 does, underscoring the added value of CHAPTER for capturing extreme precipitation at finer spatial scales.

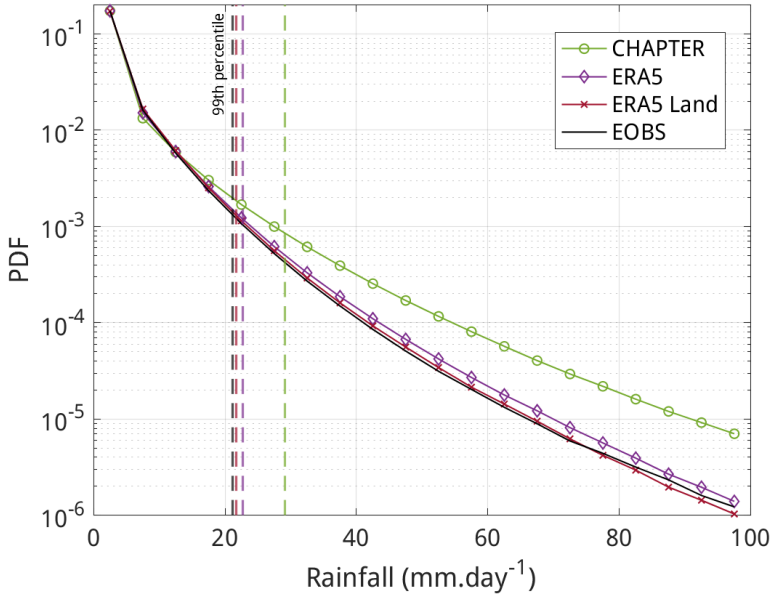

Fig. 2.14 Probability density function of the annual daily mean precipitation for the period 1981-2022 for the four datasets: E-OBS, ERA5, ERA5-Land, and CHAPTER.

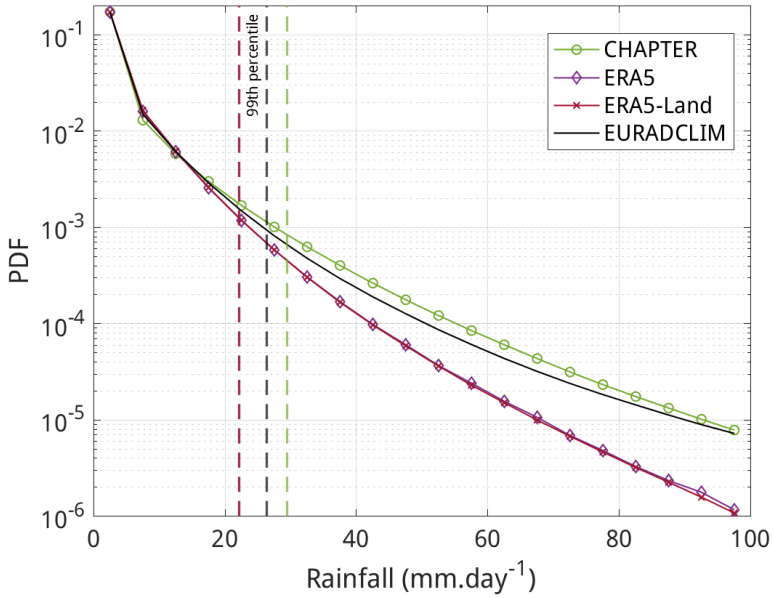

Fig. 2.15 Probability density function of the annual daily mean precipitation for the period 2013-2020 for the four datasets: EURADCLIM, ERA5, ERA5-Land, and CHAPTER.

However, the overestimation of extreme events by CHAPTER may not solely stem from its enhanced ability to represent convective events. An analysis of seasonal rainfall distributions reveals that in summer, CHAPTER overestimates extreme events compared to E-OBS, while ERA5 slightly underestimates them, as can be seen in **fig. 2.16**. In winter, both CHAPTER and ERA5 overestimate intense rainfall compared to E-OBS. A probable hypothesis is that ERA5 tends to overestimate large-scale precipitation intensity over Europe, as already found by

[172, 180, 181]. The influence of ERA5's bias in large-scale precipitation may therefore partly explain the overestimation observed in CHAPTER, particularly in winter. However, this remains only a secondary factor, as the PDF distributions suggest that CHAPTER's finer resolution is the most dominant driver, enabling a more detailed representation of both convective and large-scale precipitation processes that coarser models fail to capture. Overall, this leads to the annual overestimation shown in **fig. 2.14** and **fig. 2.15**. Further studies would be needed to fully disentangle these contributions, as the current analysis does not, for example, explain why in summer CHAPTER overestimates rainfall events when compared to EURADCLIM (**fig. 2.17**).

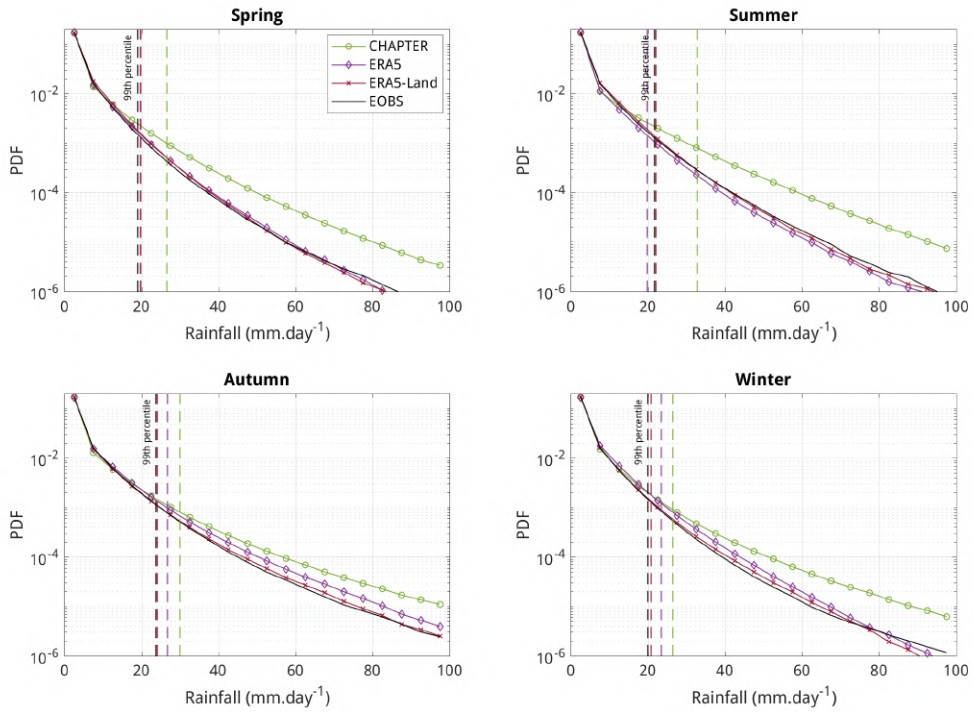

Fig. 2.16 Probability density function of the seasonal daily mean precipitation for the period 1981-2022 for the four datasets: E-OBS, ERA5, ERA5-Land, and CHAPTER.

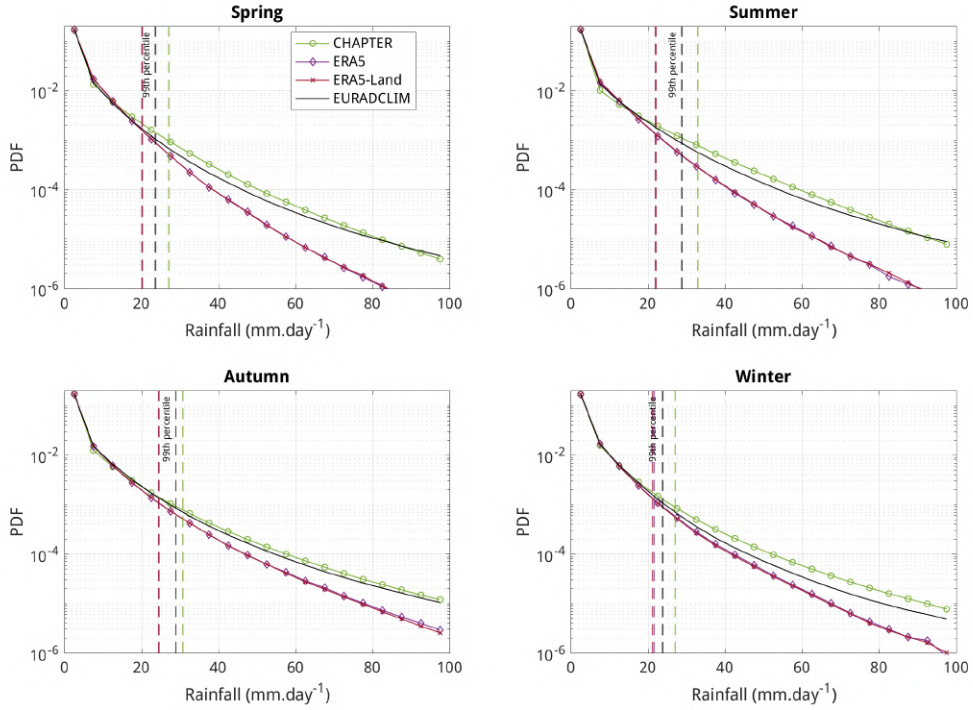

Fig. 2.17 Probability density function of the seasonal daily mean precipitation for the period 2013-2020 for the four datasets: EURADCLIM, ERA5, ERA5-Land, and CHAPTER.

A key advantage of CHAPTER lies in the availability of explicitly resolved vertical velocity. The diagnostic field of maximum upward velocity ($W_{UP,MAX}$) was employed to compute the yearly mean number of days per month exceeding a threshold of 2 $m.s^{-1}$. This metric enabled the reconstruction of a thunderstorm climatology comparable to those reported in [182, 183, 5], as can be seen comparing **figures 2.18** & **2.19**. This climatology demonstrates the capability of CHAPTER to realistically represent extreme convective events.

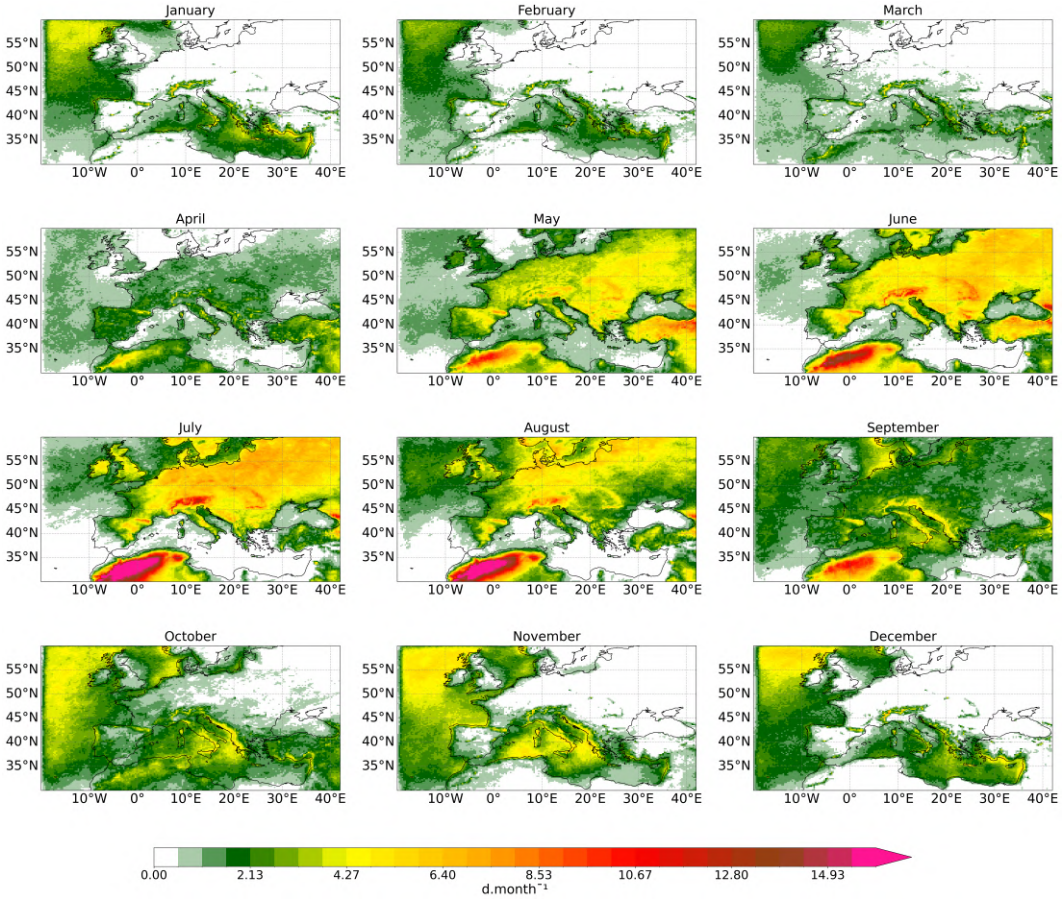

Fig. 2.18 Monthly averaged number of days with thunderstorms, i.e. days where for at least one hour $W_{UP,MAX} > 2\ m.s{-}1$ for the period 2008-2017.

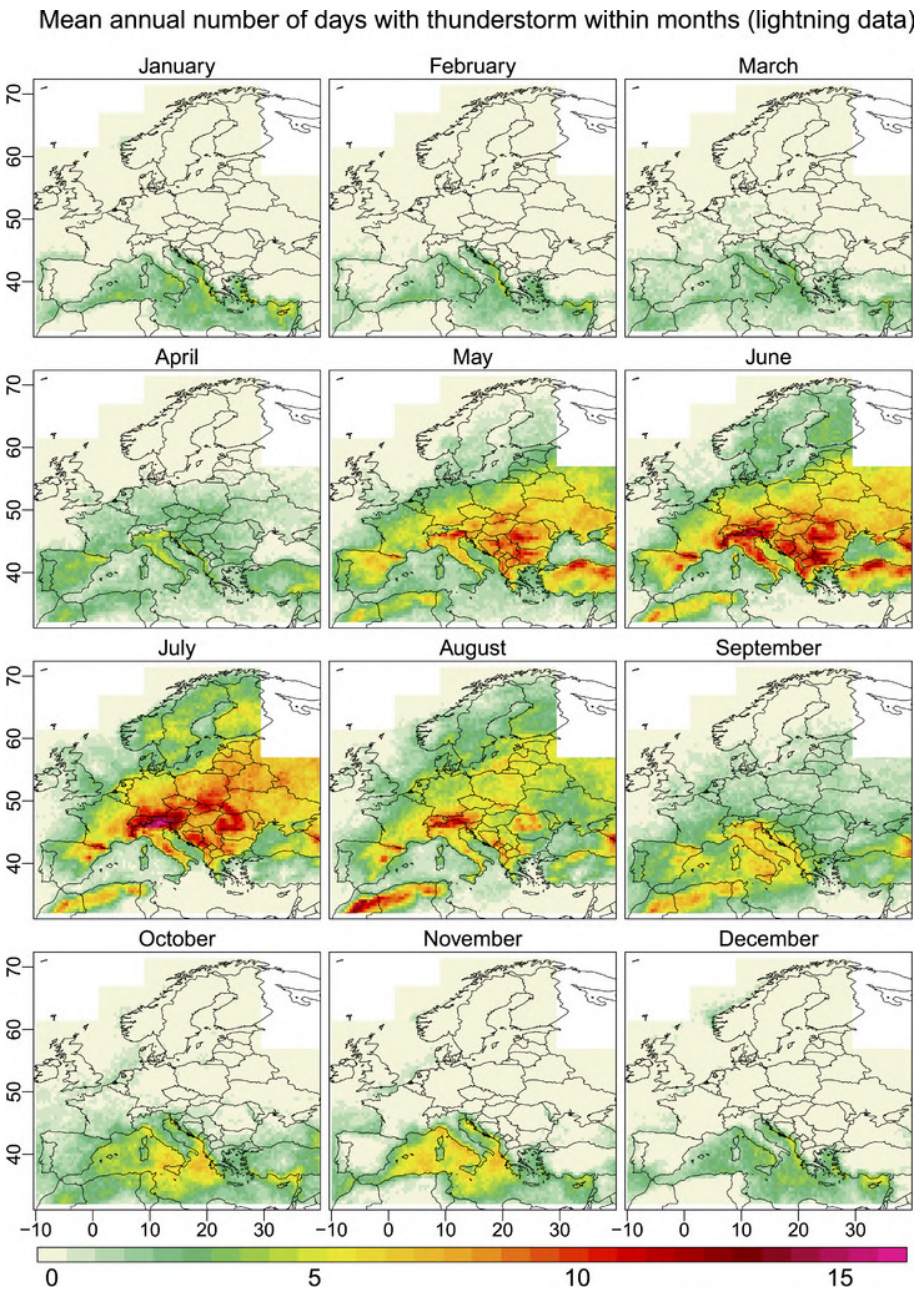

Fig. 2.19 Mean annual number of days with thunderstorms in each month, based on EUCLID and ZEUS lightning data for the period 2008-2017. Source: [5]

2.4 Discussion

The CHAPTER dataset, through its high-resolution dynamical downscaling of the ERA5 global reanalysis, offers a significant advancement in the realm of climate and weather modeling for Europe and the Mediterranean basin. One of the primary benefits of CHAPTER is its cloud-resolving grid spacing at 3 km by 3 km, which allows for detailed and precise simulations of atmospheric phenomena along with hourly temporal resolution.

Compared to existing state-of-the-art datasets, CHAPTER matches their performance and presents an important added value by providing a rich list of three-dimensional variables, such as temperature, water vapor mass fraction, wind components including vertical velocity, and microphysical species mass fractions. This enhanced spatial resolution over such a long period, 42 years, is very valuable for comprehensive physical process studies and enables a deeper understanding of severe hydro-meteorological phenomena in a changing climate.

For instance, statistical analyses of lightning potential indices, maximum vertical velocities in updrafts, and hail statistics can be performed using CHAPTER data, and be compared to observational data from recent climatologies [5, 184]. This will allow for a better understanding of the physics behind lightning and hailstorm phenomena and their predictability such as in [185]. Such insights are valuable for sectors like insurance, where risk assessment and damage prediction are critical.

Moreover, CHAPTER's high-resolution reanalysis fields, when coupled with models like the Continuum hydrological model [186], could enable detailed studies of streamflow extremes and long-term water balances [187]. This is particularly important for regions with small hydrological catchments that are vulnerable to severe rainfall events [60]. By simulating various components of the water cycle, CHAPTER can produce indicators of meteorological, hydrological, and agricultural drought attributes, thus supporting decision-making in areas heavily affected by climate variability and extremes.

High-resolution reanalysis datasets like CHAPTER are also crucial for studying wildfires because they provide detailed and precise meteorological information that is essential for understanding and predicting fire behavior [188]. CHAPTER captures the fine-scale atmospheric conditions that influence wildfire dynamics, such as wind speed, humidity, and temperature variations but also as already mentioned lightning strikes [189]. Additionally, CHAPTER's comprehensive data can drive fire behavior models, as already done by [190], and inform forest management practices, ultimately contributing to more effective wildfire prevention and mitigation strategies like prescribed fires [191].

Despite its advantages, the CHAPTER dataset faces different challenges. First, the data for each day are produced by different independent runs which can create small discrepancies at 0000 UTC. This should not be a problem for the statistical application of CHAPTER described above but needs to be evaluated when using CHAPTER to study the evolution of a specific event.

Second, the comparison with the ERA5-Land convection-parametrized downscaling does not show significant improvements across various metrics. This may be partly due to the pronounced double penalty issue in high-resolution weather simulations. Such penalties arise from spatial discrepancies in the locations of heavy rainfall or temperature peaks, resulting in mismatches with observational data [174]. This problem is intrinsic to simulations of deep moist convection, which are highly chaotic and difficult to predict with high accuracy. While a fuzzy validation technique for precipitation addresses this issue to some extent, the most effective

methods for enhancing precision involve the additional assimilation of radar observations [192] or post-processing reanalysis data using optimal interpolation techniques [26].

Data assimilation is challenging to implement at the resolution provided by CHAPTER and on such a large territory [193]. However, the integration of CHAPTER into multi-model ensemble-based approaches could mitigate this issue. Such approaches enhance the robustness of simulations and improve the representation of unresolved physics in convection-permitting models. Recent European efforts have shown that multi-model convection-permitting regional climate simulations provide a more realistic representation of heavy precipitation and improve confidence in simulating convection extremes [140, 194, 195].

Furthermore, CHAPTER's high-resolution reanalysis fields are poised to benefit machine learning applications in weather and climate analysis. These applications can include data assimilation corrections [196] and improved parameterization of atmospheric processes in general circulation models, leveraging machine learning methods to enhance predictive capabilities and model accuracy [197] as done by [198].

The last point concerns CHAPTER uncertainties. ERA5 features an ensemble data assimilation (EDA) component [199] including one control and nine perturbed members. This ensemble provides background error estimates, enabling the estimation of analysis and short-range forecast uncertainties. In contrast, CHAPTER lacks an ensemble component that precludes a direct estimation of uncertainties analogous to those provided by the EDA systems of ERA5. Nevertheless, several potential methods could be explored to assess the uncertainty in CHAPTER.

Since CHAPTER is a deterministic downscaling of ERA5, the 10-member ERA5 ensemble could, in principle, be used to generate 10 independent realizations of CHAPTER, from which uncertainty could be estimated using the ensemble spread (e.g., maximum minus minimum values). A complementary approach would consist of constructing a multiphysics ensemble by repeating the CHAPTER simulations with alternative physical parameterization schemes or by adopting a stochastic perturbation approach while keeping the deterministic ERA5 boundary conditions unchanged, thereby assessing the sensitivity of the results to model physics. However, both strategies are beyond the scope of this thesis work by their extreme computational demands.

The production of the existing 42-year CHAPTER dataset alone required approximately 42 million CPU hours on the SuperMUC-NG supercomputer at the Leibniz Supercomputing Centre (LRZ). Extending this effort to a 10-member ERA5 ensemble would therefore increase the computational cost by roughly an order of magnitude, while a multiphysics or stochastic ensemble would entail a comparable or even larger increase depending on the number of configurations considered. Such requirements make these ensemble-based approaches infeasible within the thesis work over the full spatial and temporal extent of the CHAPTER domain. Nevertheless, for carefully selected regions of interest, it may be conceivable in the future to use one or both of the approaches described above, in order to obtain localized and process-oriented estimates of uncertainty.

A more feasible alternative is the application of a pragmatic, low-budget postprocessing approach, as described by [200]. This methodology derives probabilistic forecasts from deterministic model outputs by examining the spatiotemporal neighborhood of a grid point to generate a set of forecasts. These forecasts are then used to calculate probabilistic metrics, such as ensemble mean and spread for the central point. Applying this method to CHAPTER would allow the derivation of a spatiotemporal uncertainty metric at each grid point without the need for ensemble simulations or historical error statistics, making it a cost-effective solution.

Finally, it has to be pointed out that fuzzy verification techniques provide insights into the spatial scales at which CHAPTER is reliable. As shown in the validation of precipitation section, CHAPTER reliability aligns with that of ERA5-Land and CHELSA, both of which are widely recognized as valuable downscaling products of ERA5. This alignment supports the credibility of CHAPTER's outputs at comparable spatial scales.

Overall, CHAPTER is a valuable resource for climate scientists, natural hazard researchers, and stakeholders involved in risk assessment and mitigation of extreme weather events. It offers critical insights and a robust foundation for future research and applications aimed at understanding and managing weather-related hazards in the context of global warming.

Chapter 3

Changes in Extreme Precipitation

3.1 Context and Significance

As introduced in **Chapter 1**, global warming reshapes the convective environment through a combination of thermodynamic and dynamic pathways that need to be carefully disentangled. Thermodynamic changes stem primarily from the temperature-driven increase in atmospheric moisture, as predicted by Clausius–Clapeyron scaling. Consequently, the associated increase in specific humidity enlarges the reservoir of precipitable water accessible to weather systems, allowing convective storms to yield higher rainfall intensities when they develop. This process describes the thermodynamic backdrop against which deep convection will operate in a warmer climate.

Yet the extent to which these latent thermodynamic potentials translate into changes in actual extreme precipitation depends crucially on dynamical responses - in particular, how convective organization evolves with warming. Several studies have underscored that dynamic adjustments can either amplify or counteract thermodynamic increases in humidity [201–203, 102]. For instance, while precipitation extremes tend to scale positively with moisture availability, the dynamical component of vertical motions can impose substantial deviations from Clausius–Clapeyron (CC) scaling, sometimes leading to super-CC or sub-CC behavior depending on the regional circulation response. This interplay between moisture-controlled thermodynamics and circulation-controlled dynamics is therefore central to understanding changes in convective intensity and rainfall extremes.

This chapter has been built directly on this thermodynamic–dynamic distinction by adopting a physical scaling framework similar to that advanced in recent studies [204–206] (see **section 3.2**). This approach decomposes changes in convective strength and precipitation into contributions from (i) thermodynamic forcing, or in other words, moisture changes constrained by Clausius–Clapeyron; and (ii) dynamic forcing, which involves the response of vertical velocities,

mesoscale organization, and large-scale ascent. By doing so, the goal is to clarify whether projected changes in convective extremes arise predominantly from enhanced moisture availability, from altered atmospheric dynamics, or from nonlinear interactions between the two.

These studies [203, 205, 206] collectively demonstrate that regional patterns of change in extreme precipitation cannot be inferred from thermodynamic arguments alone. Instead, they emphasize the need to account for dynamically driven variations in vertical motion, which can either reinforce or counteract the moisture-driven intensification expected under Clausius–Clapeyron scaling. For instance, enhanced ascent in regions such as the Central Pacific and Southeast Asia acts to magnify precipitation extremes beyond thermodynamic expectations, whereas weakened vertical velocities across the subtropics, including the Mediterranean, Australia, and Southern Africa, can offset or even reverse the thermodynamic tendency for intensification. Such results underscore that spatial heterogeneity in the forced response emerges from the interplay of moisture availability and evolving atmospheric circulation.

However, a significant limitation of prior work is that these thermodynamic–dynamic decompositions have been performed using global climate models. Because these models parameterize convection, the diagnosed dynamic component primarily reflects changes in large-scale vertical motion, such as shifts in the Hadley circulation, while omitting modifications to local convective organization. Consequently, the mechanisms driving the dynamic response remain only partially constrained, and key processes, such as changes in updraft intensity, entrainment, and storm morphology, are effectively hidden within parameterized subgrid physics.

To overcome these limitations, the convection-resolving CHAPTER dataset presented in **Chapter 2** was employed. CHAPTER explicitly resolves convective updrafts and associated mesoscale organization. This approach allows the dynamical pathways through which changes in storm structure, cloud-scale motions, and convective clustering contribute to the overall response of extreme precipitation to be directly examined. Combining this process-level insight with the physical scaling framework presented afterward enables a more complete and mechanistic interpretation of how thermodynamic and dynamic forcings jointly shape precipitation extremes in a changing climate.

3.2 Materials and Methods

All variables analyzed in this study are derived from the CHAPTER dataset introduced previously. The study domain is limited to (20°W–42°E; 30°N–60°N), as trend analyses of extreme precipitation over the Saharan Desert, where climatological rainfall is extremely low, can produce artificially large but statistically non-significant relative changes.

As already anticipated, following [204–206], the hourly maxima precipitation found in CHAPTER has been approximated with a physical scaling diagnostic. This scaling allows the decomposition of maximum precipitation changes into thermodynamic and dynamic contributions:

$$P_e = -\varepsilon \left\{ \omega_e \frac{dq_s}{dp}\bigg|_{\theta^*} \right\} \tag{3.1}$$

Where P_e, the annual maximum hourly precipitation at each model grid point, is related to the corresponding vertical pressure velocity ω_e and the vertical derivative of the saturation specific humidity q_s at constant saturation equivalent potential temperature θ^*. Finally, $\{.\}$ indicates a mass-weighted vertical integral over the troposphere.

This scaling relation can be derived by assuming a moist-adiabatic, saturated ascent of air parcels. The term in brackets in equation **3.1** provides an estimate of the column-integrated condensation rate associated with the ascending motion. Following [207], to account for the fact that not all condensed moisture contributes to surface precipitation, a precipitation efficiency term, ε, is included in the scaling. This parameter represents not only the evaporation of falling precipitation in subsaturated layers, but also the effect of the lifting condensation level being generally located above the surface. As a consequence, vertical gradients of the saturation specific humidity in the lower troposphere may not be associated with condensation.

This scaling framework allows the total temporal changes in P_e to be decomposed into distinct dynamic and thermodynamic contributions. To this end, a thermodynamic scaling is defined using equation **3.1** while neglecting time variations in the vertical velocity associated with extreme precipitation; specifically, at each location, ω_e is replaced by its temporal mean over all extreme events during the period 1981–2022. Conversely, a dynamic scaling is computed by neglecting time variations in the saturation specific humidity, such that, at each location, the pressure and temperature fields used to calculate q_s are replaced by their temporal averages over all extreme events in the same period.

Instead of computing the scaling only for the single hour associated with the annual maximum precipitation, a sensitivity analysis was performed by calculating the scaling for the 20 highest-precipitation hours of each year over the 1981–2022 period. For each of those 20 hours, profiles of hourly temperature, pressure, and vertical velocity on model levels were extracted at the corresponding grid point locations. In the next section, results based on the average of the five hours with the most intense precipitation are presented. This choice represents a compromise: it captures the characteristics of the most extreme events while avoiding the noise that may arise when relying on a single hour. Results based on averaging the top 20, 10, and the single most intense precipitation hours are provided in **Appendix A** (**sup. fig. A.6, A.7, & A.8**).

While the WRF model used in CHAPTER was integrated at a native grid spacing of 0.03° (Δx), it is well-established that the effective resolution of such models, that is to say the scale at which they accurately resolve physical features, is typically $6\Delta x$ to $8\Delta x$. This is due to numerical diffusion and the Nyquist limit [208, 209, 133]. Such an effective resolution is confirmed for CHAPTER with the validation analyses presented **Chapter 2**. Notably, the fuzzy validation technique performed for daily precipitation data shows that CHPATER is more reliable at spatial

scales superior to $5\Delta x$. Therefore, for a better representation of the principal patterns, the final scaling results presented in the next section have been upscaled to a grid with a 0.24° spatial resolution (approximately $8\Delta x$) using a box-averaged remapping. This procedure filters out inherent grid-scale noise and ensures that the analyzed precipitation trends reflect physically robust, skillful scales rather than numerical artifacts.

Alongside the scaling, two key variables were employed to evaluate environmental convective potential: Convective Available Potential Energy (CAPE) and Moist Static Energy (MSE). These two variables were introduced in the first chapter of this thesis (**1**); for completeness, they are recalled here and defined mathematically below.

While CAPE directly measures the vertically integrated buoyant energy available to an ascending air parcel and is therefore closely tied to storm intensity, MSE describes the energetic content of the air column and is approximately conserved under moist adiabatic motions. As such, vertical gradients in MSE provide a physically intuitive framework for understanding the origin of CAPE, with CAPE emerging from differences between the MSE of near-surface air and that of the overlying troposphere. The two diagnostics are thus complementary: CAPE quantifies convective instability explicitly, whereas MSE offers a more fundamental and thermodynamically grounded perspective on how this instability is established and how it evolves under climate change.

$$MSE = C_p T \; + \; L_v q \; + \; gz \tag{3.2}$$

With C_p the specific heat at constant pressure, T the absolute air temperature, L_v the latent heat of vaporization, q the specific humidity, g the gravitational constant, and z the geopotential height above sea level.

$$CAPE = g \int_{LFC}^{EL} \frac{T_{v_{parcel}} - T_{v_{env}}}{T_{v_{env}}} \, dz \tag{3.3}$$

With LFC the level of free convection, EL the equilibrium level (level of neutral buoyancy); $T_{v_{parcel}}$ is the virtual temperature of the considered parcel, and $T_{v_{env}}$ is the virtual temperature of the surrounding environment.

More specifically, the CAPE presented in the results section (**3.3**) is defined as the maximum CAPE occurring within the six hours preceding each hourly precipitation maximum. In addition, for each of these six time steps, we retained the maximum CAPE value within a surrounding neighborhood defined by a radius of three grid cells. This spatial maximization accounts for potential displacement between the location of peak convective instability and the precipitation maximum, reflecting the influence of mesoscale organization and advective processes.

3.3 Results

3.3.1 Extreme precipitations

The temperature increase in the CHAPTER dataset was briefly introduced in **Section 2.3.2**, where the domain-averaged time series indicates a mean warming of 1.3 K over the period 1981–2022. However, this spatially averaged value conceals substantial regional and seasonal variability, as shown in **figure 3.1**. In both winter and summer, large areas in the central–eastern part of the domain exhibit warming trends approximately twice the domain mean, with local temperature increases reaching up to 3.5 K. This corresponds to a substantial change relative to the regional mean surface temperature of about 295 K, whose climatology is shown in the **supplementary figure A.1**.

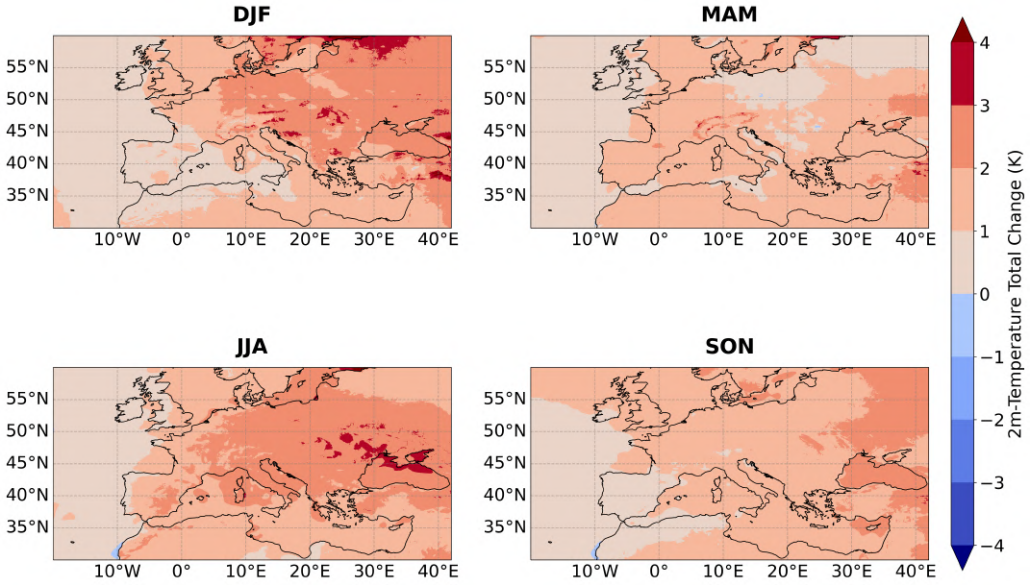

Fig. 3.1 Seasonal total change of 2m temperature between 1981 and 2022.

The domain-mean annual hourly precipitation amounts to approximately 0.08 $mm.h^{-1}$. Over the study period, despite the warming, this mean value does not exhibit any substantial change. Indeed, the change in hourly mean precipitation averaged over the entire domain is 0.00 $mm.h^{-1}$, reflecting a compensation between positive and negative regional trends. However, this domain-wide average masks pronounced spatial and seasonal contrasts (see **fig. 3.2**). During summer, precipitation decreases of up to -0.05 $mm.h^{-1}$ are observed north of the Black Sea, whereas in fall, increases reaching $+0.06$ $mm.h^{-1}$ occur over the Ionian Sea. These variations should be interpreted relative to the local seasonal climatology, which is on the order of 0.11 $mm.h^{-1}$ for Ukraine in summer and of 0.14 $mm.h^{-1}$ for the Ionian Sea in fall (see **sup. fig. A.2**).

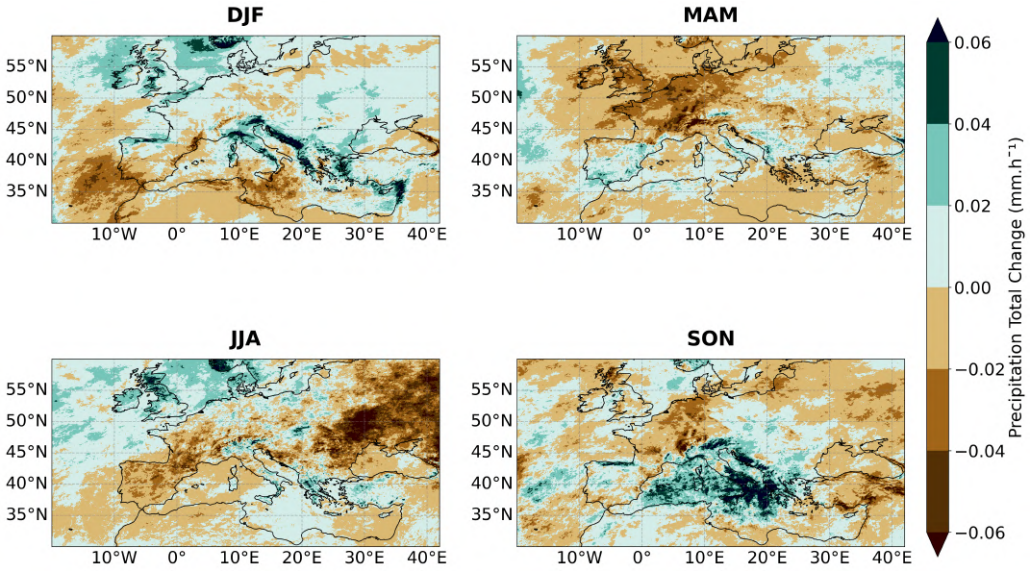

Fig. 3.2 Seasonal total change of hourly accumulated precipitation between 1981 and 2022.

Summer and fall are highlighted here because, when selecting the five hours per year corresponding to the most intense precipitation at each grid point, as described in **Section 3.2**, these two seasons contain the highest numbers of extreme precipitation events (see **sup. fig. A.3**). This behaviour is expected, as the most intense hourly precipitation is typically associated with convective phenomena that predominantly occur during the warmest months of the year [210]. The 1981-2020 average of the intensity of the 5 most extreme hourly precipitation events per year is shown in **fig. 3.3**. Its domain average is 12.5 $mm.h^{-1}$, but larger values are present, especially in the Ionian Sea and in several Northern Mediterranean coastal areas.

Using **eq. 3.1**, it can be assessed how effectively the proposed scaling relationship reproduces the spatial pattern of these extreme events. In the assumption that the precipitation efficiency, ε, does not change over time, extreme hourly precipitation P_e is computed using **eq. 3.1** and ε is obtained as follows. First, the scaling was computed using $\varepsilon = 1$. Then, at each location the ratio between the time average of hourly precipitation for the selected extreme events (as shown in **fig. 3.3.a**) and the time average of the corresponding scaling values (as shown in **sup. fig. A.4.a**) was computed. This ratio was used as a spatially variable efficiency factor (**sup. fig. A.4.b**). Its domain mean was then used to define $\varepsilon = 0.68$ in **eq. 3.1**, leading to the time mean values of scaled precipitation shown in **fig. 3.3.b**. It is stressed that this procedure affects the magnitude of the extreme precipitations reconstructed using **eq. 3.1** but not their spatial nor temporal relative variability, as the same ε value is used at any location and time.

The maps of the extreme precipitation intensity averaged over the study period and the corresponding scaling-reconstructed extreme rainfalls, shown in **fig. 3.3**, have a spatial correlation of 0.88. This large correlation coefficient confirms that the scaling relationship accurately captures the spatial pattern of annual maximum precipitation for the period considered (**fig. 3.3.a** and **fig. 3.3.b**).

However, it tends to overestimate precipitation amounts in regions with complex orography, such as the Alps, the Cantabrian Mountains, and the Dinaric Alps. The performance is slightly lower than reported in [206], likely because the assumption that local net condensation rate directly corresponds to precipitation extremes holds more robustly at the coarser resolutions of global simulations (0.5°–4° in the CMIP5 models), as lateral liquid water transport among larger grid boxes is less important.

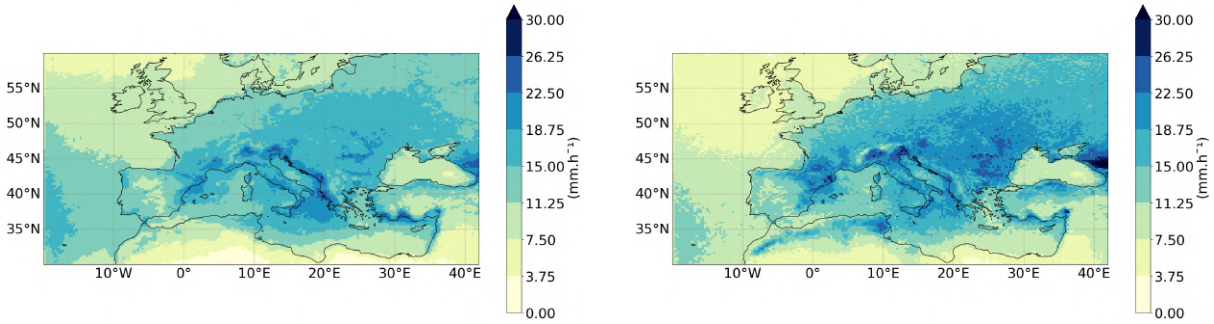

(a) CHAPTER precipitation

(b) Scaling-reconstructed precipitation

Fig. 3.3 Mean top-5 annual hourly precipitation (mm.h^{-1}) from CHAPTER rainfall (left), and from scaling-reconstruction using eq. 3.1 (right), all averaged over the period 1981–2022. Data have been upscaled at 0.24° latitude and longitude using a box average.

The changes in precipitation extremes in recent decades have been investigated by calculating linear regressions of the relative change of annual mean intensity of the extreme precipitation events at each grid point (with respect to the mean over the whole period), as shown in **fig. 3.4.a**. The domain mean extreme precipitation change has been +0.9 $mm.h^{-1}$, which is a relative increase of 7% compared to the annual mean of 12.5 $mm.h^{-1}$ (**fig. 3.3.a**). Such a relative increase, with respect to the total temperature change of $+1.3$ K corresponds to a sub-CC scaling. However, different spatial patterns are observed: the positive trends are observed in most of the Mediterranean and North Sea, with increases up to 8 $mm.h^{-1}$ (corresponding to +50%, a super-CC scaling), while the western part of France, the Iberian Peninsula, and the border between eastern Europe and Russia experienced negative trends.

Over the period 1981–2022, changes in extreme precipitation can be expected to be strongly influenced by natural variability; nevertheless, statistically significant trends do emerge in specific regions. A Student's t-test was applied to the precipitation trends under the null hypothesis of zero slope, revealing that approximately 10% of grid points exhibit significant trends at the 95% confidence level (see **sup. fig. A.5**). These localized areas of significance highlight regions where the forced signal in extreme precipitation is detectable above background variability.

The scaling-reconstructed precipitation change (**fig. 3.4.b**) does capture the main features of the model changes, with a spatial correlation of 0.73. Although the signal is noisier than in the model output and tends to overestimate trend magnitudes, it still provides a useful framework for examining changes in extreme precipitation. The main part of the precipitation changes is driven by the dynamic contribution (**fig. 3.4d**), which well reproduces the observed changes in

the full scaling (**fig. 3.4.b**). The spatial correlation between the model outputs (**fig. 3.4.a**) and the dynamical scaling is 0.70, while with the thermodynamic scaling, the spatial correlation is 0.58. Therefore, changes in convective dynamics emerge as the dominant factor, more accurately reproducing the spatial distribution and intensity in changes of the extreme events found in the CHAPTER precipitation dataset.

To further assess the robustness of these results, a series of sensitivity tests were performed in which the scaling was computed using different definitions of extreme precipitation, considering not only the five hours with the most intense precipitation but also the 20, 10, and single most intense hourly events, as described in the section **Materials and Methods** (**3.2**). Across all configurations, the resulting spatial patterns remain essentially unchanged, confirming that the diagnosed trends are not sensitive to the number of extreme events used to define the scaling. In all cases, the dynamical component consistently dominates and drives the changes in extreme precipitation simulated by the model, as summarized in the supplementary **table A.1**. As expected, however, the spatial correlation between the model output and the scaling decreases when fewer events are considered, reflecting the increased noisiness of the scaling when it is based on a very limited number of extreme events, particularly in the single-event case.

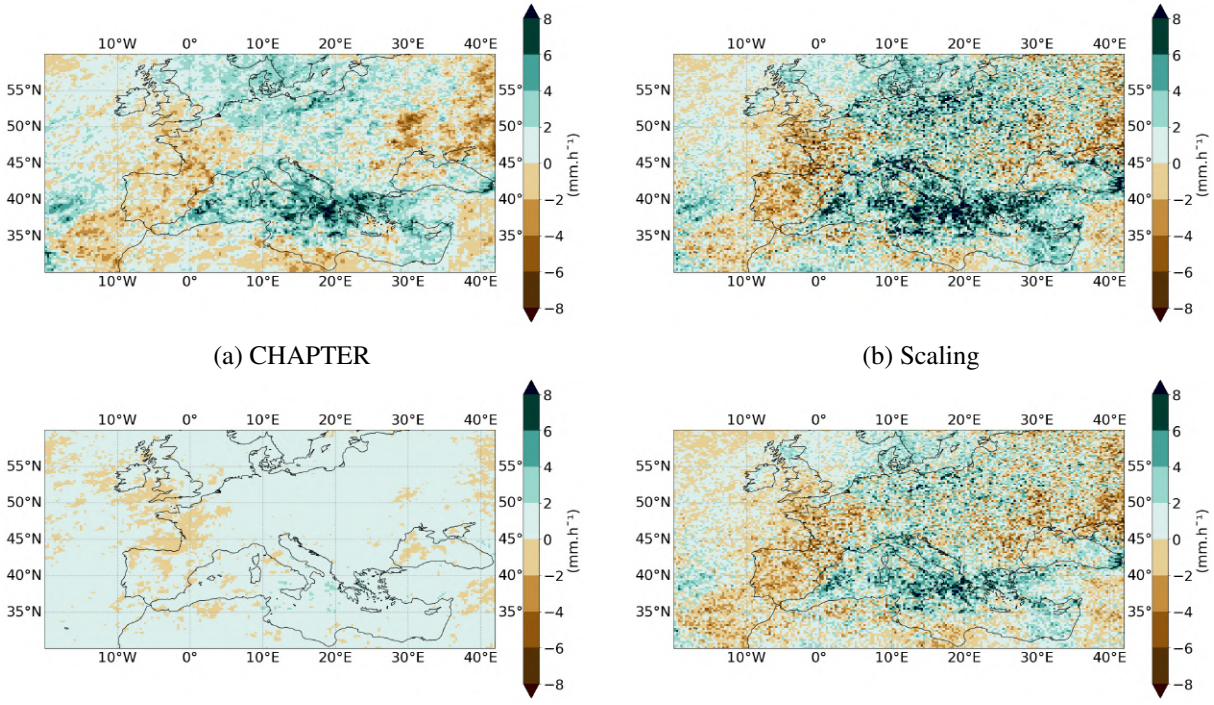

(a) CHAPTER

(b) Scaling

(c) Thermodynamic scaling (omega constant)

(d) Dynamic scaling (temperature constant)

Fig. 3.4 Total change in mean top-5 annual hourly precipitation (top, left), precipitation extremes scaling (top, right), the thermodynamic scaling (center, left), and the dynamic scaling (center, right), derived from a linear regression for the period 1981-2022. The unit is $mm.h^{-1}$. Data have been upscaled at 0.24° using a box average.

3.3.2 The role of convective instability

Considering that most selected extreme events occur during the summer and fall seasons (**fig. A.3**), convective instability is expected to contribute to their occurrence. The fraction of selected events associated with high CAPE values is therefore quantified. Convection is considered to be an important player in the precipitation event in case the corresponding CAPE was larger than a given threshold (here taken as 500 J/kg, but sensitivity with respect to changes in this threshold has been investigated).

Over vast areas in continental Europe and the Mediterranean, most events are characterized as convective events, while over the Atlantic Ocean, the North Sea, and much of Northern Africa, convection is not important (**fig. 3.5.a**). When looking at the trend in the fraction of convective events among the selected extreme events, it can be noticed that there is a decrease in the number of convective events over the Iberian Peninsula, Western France, and the Eastern part of the domain, i.e., where there is a decrease in the intensity of extreme precipitation (**fig. 3.4.a**), and in the dynamical scaling (**fig. 3.4.d**). On the other hand, there is an increase in the number of convective events over most of the Mediterranean Basin, and especially in the Levantine Basin. No particular signal is observed over the Ionian Sea, where extreme precipitation events are already almost exclusively convective from the beginning of the study period, such that the fraction of convective events is close to 100% and cannot increase substantially.

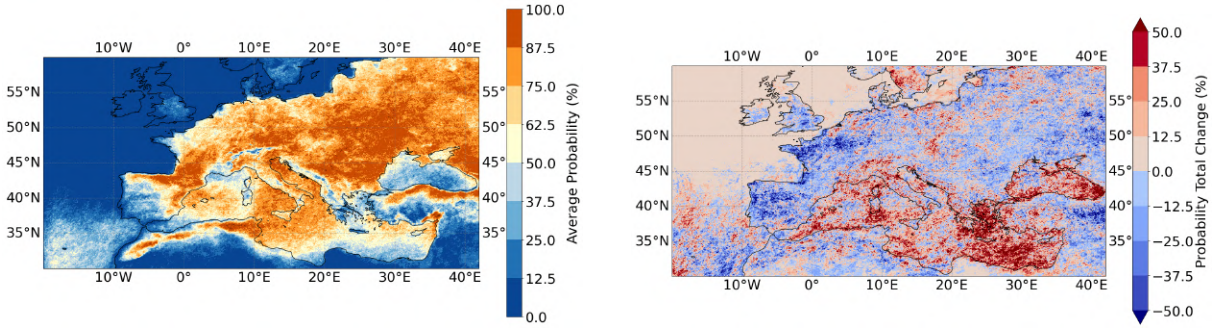

(a) Climatology (b) Trends

Fig. 3.5 Climatology (left) and total change (right) of the probability that the mean CAPE between the top-5 annual hourly precipitation (**fig. 3.4.a**) exceeds a threshold of $500 J.kg^{-1}$.

The motivation behind these changes in CAPE can be investigated using the moist static energy (MSE). Focusing on the fall season, during which the events considered here predominantly occur (**sup. fig. A.3**), the climatological difference between surface and mid-tropospheric MSE over the 1982–2022 period exhibits a pronounced spatial contrast (**fig. 3.7**). Positive values prevail over the Mediterranean Sea, indicating that near-surface air has higher energetic content than the free troposphere, a configuration favorable for deep convection. This is consistent with the large CAPE values observed over the same region (**fig. 3.5.a**). In contrast, negative MSE differences dominate over the Iberian Peninsula, reflecting a more stable atmospheric column and a reduced potential for deep convective development.

Changes in the surface-to-mid-tropospheric MSE difference over the same period further mirror the spatial pattern of extreme precipitation intensity, with a pronounced increase over the central Mediterranean basin and a weak negative change over France and the Iberian Peninsula (**fig. 3.7**). Notably, the increase occurs in regions where the MSE difference is already positive, whereas regions characterized by negative MSE differences show minimal change. Together, these results indicate a strengthening of convective instability in areas that are already prone to deep convection, while regions that are climatologically stable experience limited modification of convective instability despite surface warming.

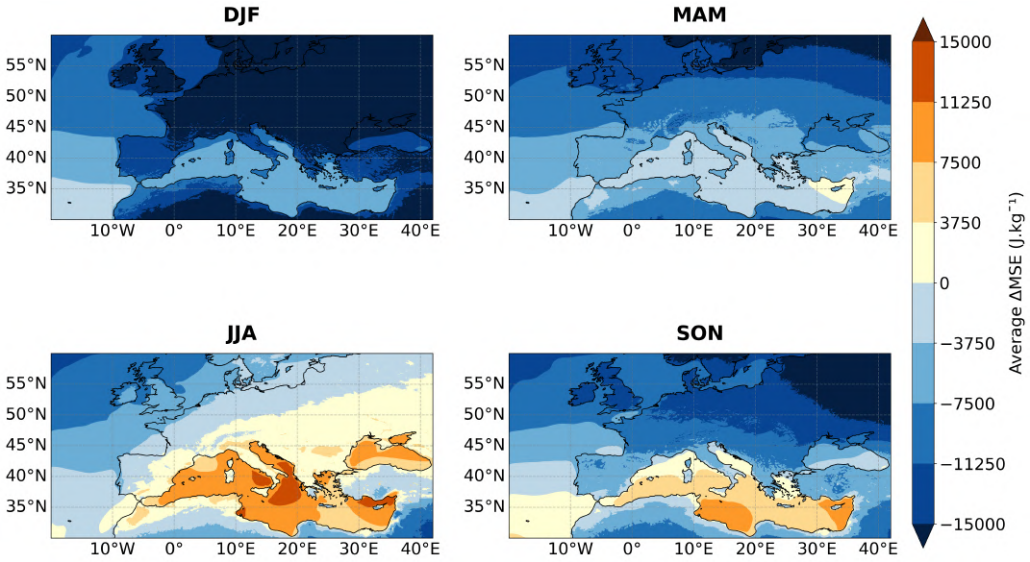

Fig. 3.6 Seasonal climatology of the difference between surface and mid-tropospheric MSE between 1981 and 2022.

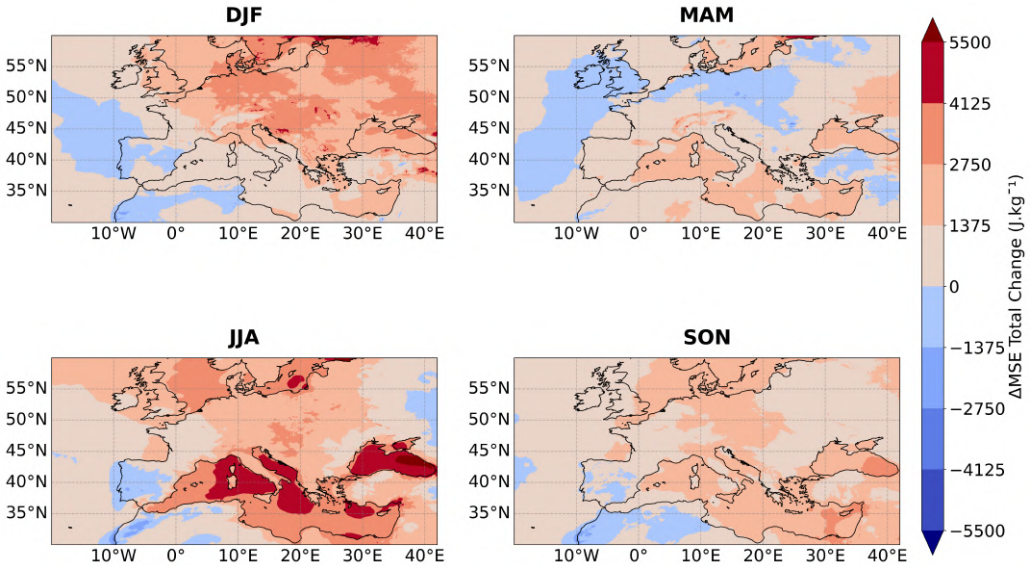

Fig. 3.7 Seasonal total change of the difference between surface and mid-tropospheric MSE between 1981 and 2022.

To better understand the mechanisms driving this evolution, surface MSE changes (**sup. fig. A.9**) have been decomposed into the temperature component ($c_p \times t_{2m}$ see **sup. fig. A.10**) and the specific humidity component ($L_v \times q_{2m}$; see **sup. fig. A.11**). This decomposition reveals that the contrasting MSE response is primarily controlled by changes in specific humidity (**fig. 3.8**). In fall, near-surface specific humidity increases strongly over the central Mediterranean (Italy, Greece, and the Ionian Sea), while remaining weak or decreasing over the Iberian Peninsula, even though the two regions have a sensibly similar climatology as shown in the **supplementary figure A.12**. These opposite changes result in a clear dipole in surface MSE (**fig. A.9**).

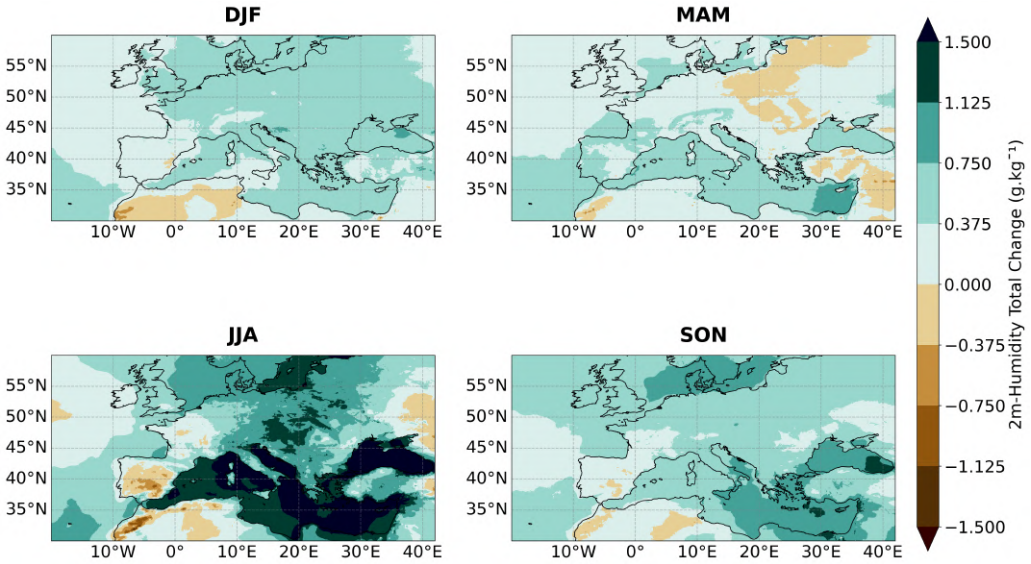

Fig. 3.8 Seasonal total change of 2m specific humidity between 1981 and 2022.

Over the Iberian Peninsula, soil moisture is climatologically low during fall and exhibits a marked decreasing trend under warming conditions (**fig. 3.9 & sup. fig. A.13**). This combination of limited baseline moisture availability and ongoing drying strongly constrains evaporation, leading to reduced near-surface specific humidity. In contrast, southern Italy and Greece are characterized by higher climatological soil moisture in autumn, which is further increasing over time (**fig. 3.9 & sup. fig. A.13**). This wetter baseline state, together with the sustained moisture supply provided by the Mediterranean Sea, allows evaporation to remain largely unconstrained. As a result, near-surface humidity and convective potential are enhanced in the central and eastern Mediterranean.

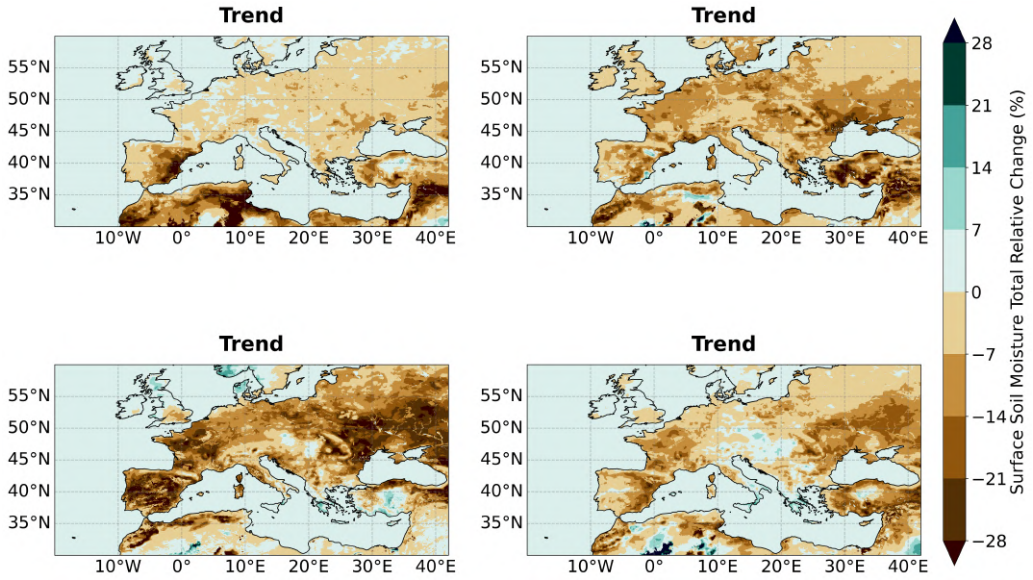

Fig. 3.9 Seasonal total relative change of first level soil moisture between 1981 and 2022.

Therefore, the results point to a strong modulation of convective responses by the underlying climatological moisture regime, highlighting a feedback between surface water availability, evaporation, and convective intensity. Over the Iberian Peninsula and Western France, the climatological environment is not conducive to deep convection, owing to limited soil moisture and surface evaporation. Under warming conditions, this moisture limitation intensifies, preventing surface moist static energy from increasing sufficiently to destabilize the atmospheric column. As a result, convective activity remains suppressed, leading to a decrease in hourly extreme precipitation (**fig. 3.4.a**).

In contrast, over the Ionian Sea region, encompassing southern Italy and Greece, the climatological environment is already favorable for deep convection, supported by high sea-surface temperatures and ample soil moisture. In this moisture-rich regime, warming enhances evaporation from both land and sea, increasing near-surface moisture and convective instability. This leads to a coherent intensification of both mean fall precipitation (**fig. 3.2**) and hourly extreme rainfall (**fig. 3.4.a**). Together, these results indicate that the response of extreme precipitation to warming is strongly conditioned by the pre-existing climatological moisture state, with convection-prone regions becoming more unstable, while moisture-limited regions experience a weakening of convective extremes.

3.4 Discussion

The results indicate that, over the 1981–2022 period, annual hourly precipitation extremes over the study domain increased on average by about 0.9 $mm.h^{-1}$ in association with a mean warming of +1.3 K. This signal, however, exhibits strong spatial heterogeneity and generally low statistical significance, pointing to a substantial influence of natural variability. The physical scaling

framework reproduces the main features of the observed spatial patterns, and the decomposition highlights the dominant role of the dynamical contribution relative to the thermodynamic one in shaping regional changes in extreme precipitation.

This finding contrasts with many previous studies in which the thermodynamic component, associated with increased moisture availability under warming, is often regarded as the most robust and certain aspect of the response. For example, [206] found at the global scale only a weak contribution from synoptic-scale vertical velocity, with thermodynamics capturing most of the forced signal in heavy precipitation extremes in the mid latitudes.

Such conclusions, however, are largely drawn from global-scale analyses that rely on coarse-resolution climate models with parametrized convection and focus on daily extreme precipitation, a temporal scale at which convective processes play a relatively smaller role. As a result, these studies tend to emphasize large-scale, moisture-driven responses. Moreover, these studies have predominantly examined future climate projections, for which the externally forced thermodynamic signal is expected to be stronger than in historical changes. As a result, thermodynamically driven responses tend to dominate in such analyses, whereas in the historical, high-resolution framework considered here, dynamic processes play a more prominent role.

At regional and hourly scales, dynamical processes are widely recognized as critical modulators of precipitation extremes. [211], for instance, demonstrated that moisture increases alone are insufficient to explain regional patterns of heavy precipitation, while [212] emphasized that dynamical changes, although more uncertain, are critical for understanding regional climate impacts and informing adaptation.

The importance of dynamics is further supported by [204], who highlighted that improving the representation of vertical velocities is essential for more realistic simulations of precipitation extremes. Also [206] acknowledged that dynamical contributions can substantially modulate regional responses; however, for the Mediterranean region, they found that dynamics tend to weaken the thermodynamically driven increase, whereas the present results indicate an intensification of extremes associated with strengthened dynamics. This discrepancy supports the hypothesis introduced earlier: at regional scales and in areas where convection plays a central role, increases in extreme precipitation are more plausibly explained by a strengthening of convective dynamics in a warmer climate rather than by moisture increases alone.

However, these results are affected by substantial uncertainty, as illustrated by the limited spatial extent of statistically significant trends, which suggests that internal climate variability strongly modulates changes in extreme precipitation over the 1981–2022 period. This dominance of variability does not imply that the analysis is flawed or uninformative; rather, it is consistent with the well-established difficulty of isolating a clear climate-change signal in precipitation extremes at regional scales over a few decades.

As emphasized by [213], natural variability can obscure underlying long-term tendencies in both observations and model-based datasets, leading to noisy and spatially heterogeneous signals

even when physical intensification mechanisms are expected to operate. In this context, high-resolution downscaling remains one of the most powerful tools available to investigate spatial patterns of extremes, as it allows a more realistic representation of mesoscale processes and convective rainfall that are essential for capturing regional contrasts, as shown by [214]. While such approaches cannot eliminate irreducible uncertainty, they provide physically consistent information that would be inaccessible at coarser resolutions.

Ultimately, a key avenue for improving robustness would be the construction of ensembles, for instance by combining CHAPTER with other downscalings of ERA5 over targeted subregions [151, 152, 155, 153], to better separate forced signals from internal variability. Large initial-condition ensembles, as discussed by [215], offer a conceptual framework for this strategy. Their work suggests that the methodology developed for CHAPTER could be extended in future work to ensemble-based analyses, yielding more robust regional assessments despite the inherently low signal-to-noise ratio. However, as already discussed in **Chapter 2** (**Section 2.4**), the implementation of such ensemble-based analyses at convection-permitting resolution remains highly challenging from a computational perspective, particularly when applied to large spatial domains and multi-decadal periods.

Building on the contrasting autumnal responses identified across the Mediterranean, with drying and weakening extremes over the Iberian Peninsula and Western France versus increasing moisture availability and intensifying precipitation over southern Italy and Greece, the results align with a well-established body of literature highlighting both direct and indirect soil moisture–precipitation feedbacks. Early studies [216, 217] emphasized a direct feedback, whereby reduced soil moisture leads to diminished evapotranspiration and, consequently, reduced atmospheric moisture availability and precipitation. They also documented how this mechanism can propagate soil moisture deficits seasonally, from reduced spring snowmelt to enhanced summer drought conditions.

Beyond this direct pathway, several studies have proposed an indirect feedback mediated by surface energy balance, radiation, and convective instability. [218] and [219] showed that dry soils reduce net radiation and total turbulent heat fluxes, thereby lowering boundary-layer moist static energy (MSE) and limiting the energy available for deep convection. This framework was further developed by [220], who identified land–atmosphere coupling regimes in which wet soils enhance convective activity through increased latent heat flux and CAPE, a regime particularly relevant for transitional climates such as the Mediterranean. [221] synthesized these mechanisms, emphasizing that soil moisture–precipitation coupling is strongest in such transitional regions, where drying can effectively suppress latent heat fluxes and convective potential, as suggested by the findings over Iberia.

In this context, the use of boundary-layer MSE as a proxy for land–atmosphere coupling is well justified: [218] explicitly linked wet soils to higher boundary-layer MSE and increased rainfall likelihood, while more recent work by [222] showed a robust relationship between MSE and extreme precipitation, suggesting relatively stable precipitation efficiency. Together,

these studies support the interpretation that contrasting soil moisture trajectories across the Mediterranean modulate evaporation, boundary-layer energetics, and ultimately the occurrence of extreme rainfall through both direct moisture limitation and indirect energetic pathways.

Despite its relevance, the use of MSE as a primary diagnostic has inherent limitations. A more comprehensive characterization of the convective environment would ideally include additional indicators such as Convective Inhibition (CIN), total column water vapour, or thunderstorm-oriented indices such as the K-index or Total Totals (TT). Temporal constraints prevented the inclusion of these diagnostics in the present thesis. Moreover, a definitive attribution of the feedback mechanism discussed in this chapter would require targeted numerical sensitivity experiments, in which surface evaporative fluxes are artificially decoupled from soil moisture availability. Such experiments would allow a direct assessment of the influence of soil moisture on convective updraft dynamics and extreme precipitation at the regional scale. However, the computational demands and associated carbon footprint of simulations covering the full CHAPTER domain at the required resolution render this approach unfeasible. In the absence of a means to fully disentangle these interactions within the available dataset, the physical coherence of the results nevertheless provides strong circumstantial evidence for a soil moisture–precipitation feedback operating through both moisture supply limitations and boundary-layer energetic modulation of convection.

Chapter 4

The Development of Tropical-Like Features in Mediterranean Cyclones

4.1 Context and Significance

While the previous chapter focused on convection at the local scale, it is essential to recognize that convective activity is often organized, intensified, and sustained by larger-scale synoptic structures. In the Mediterranean, more than 80% of precipitation extremes are directly associated with cyclones [102], underscoring the close coupling between local convective sensitivity and broader dynamical forcing. Variations in storm tracks, upper-level disturbances, and large-scale circulation patterns therefore play a central role in shaping extreme events. To fully understand their drivers, the analysis must extend beyond isolated convective processes to encompass the environmental conditions that promote the development of organized convective systems. This chapter adopts such a perspective by focusing on the environments associated with the most intense form of organized convective systems in the Mediterranean: tropical-like cyclones.

As introduced in **Chapter 1**, the majority of Mediterranean cyclones follow the extratropical paradigm; however, a subset can undergo profound structural changes when deep, persistent convection becomes established near their core. These Mediterranean Tropical-Like Cyclones (MTLC), or *medicanes*, can acquire enhanced axisymmetry, strong diabatic forcing, and the development of a deep warm core. Their hybrid character, straddling baroclinic and tropical dynamics, challenges traditional cyclone classifications and raises fundamental questions about the mechanisms governing their evolution.

MTLC are relatively rare phenomena, with an annual frequency that depends on the definition adopted but generally amounts to only a few cases per year [223–226]. As a result, the physical mechanisms underlying their development have most often been investigated through detailed analyses of individual or small sets of case studies [223, 227–229]. A more systematic perspective

was provided by the climatological study of [230], based on downscaled reanalysis data, which characterized the large-scale environmental conditions associated with their formation. That study highlighted the presence, during the early stages, of weak vertical wind shear, upper-level cold intrusions, enhanced moisture availability, and strong vorticity, expressed as anomalies relative to the seasonal climatology.

However, many of these environmental features are not specific to Mediterranean tropical-like cyclones, but are also commonly associated with Mediterranean cyclones more generally, including classical cold-core systems. This raises a fundamental open question: which factors control whether a Mediterranean cyclone follows a "classical" extratropical evolution or transitions toward a tropical-like structure?

Addressing this question requires first clarifying which tropical-like characteristics are considered when identifying Mediterranean tropical-like cyclones. Recent efforts within the scientific community have therefore sought to formalize the defining features of medicanes and to provide a clearer framework for their identification [231]. In this spirit, the following definition has been proposed:

"A medicane is a mesoscale cyclone that develops over the Mediterranean Sea and displays tropical-like cyclone characteristics: a warm core extending into the upper troposphere, an eye-like feature in its center with spiral cloud bands around, an almost windless center surrounded by nearly symmetric sea-surface wind circulation with maximum wind speed within a few tens of kilometers from the center."

While this definition reflects a growing consensus within the scientific community, it remains focused on a specific subset of Mediterranean cyclones exhibiting the most pronounced tropical-like characteristics. As such, it does not encompass all Mediterranean cyclones that develop significant warm-core structures, which may share similar physical processes without fully satisfying all morphological or dynamical criteria of the definition.

Therefore, this study adopts a more phenomenological approach by introducing the term Deep Warm-Core Cyclone (DWCC) to denote Mediterranean cyclones that develop a pronounced and vertically deep warm-core structure during their mature phase, irrespective of whether they meet all the criteria of the existing Medicane definition. This choice allows the analysis to focus on the physical processes leading to warm-core development, acknowledging that such development may arise from multiple mechanisms across a broader spectrum of Mediterranean cyclones.

Indeed, the development of DWCC can be associated with the WISHE mechanism [79]. This means that DWCC evolution is due to the positive feedback between the sea surface heat fluxes and the surface wind [232, 227]. In those cases, the large release of latent heat favors the development of a warm core and deep convection is significant to maintain the system, as in TC. Another mechanism that leads to the development of a warm core is associated with the enhancement of the low-level circulation by the upper-level PV anomaly, which in turn increases

the sea-surface fluxes [233]. In those cases, the warm core is mainly a consequence of warm air seclusion in the cyclone's inner core by surrounding colder air [234, 227], and convection becomes rather weak during the mature stage of the cyclone.

In this work, the conditions under which the cyclones develop a warm core are analyzed. The novelty lies in providing a systematic and climatic analysis of DWCC within the broader population of Mediterranean cyclones. Rather than focusing on a limited number of emblematic events, a large dataset spanning a wide range of cyclones' types and intensities was exploited. By comparing DWCC with intense cold-core cyclones, the evolution of their structure and environmental conditions throughout the cyclone life cycle was analyzed to identify the factors that distinguish warm-core development from more typical Mediterranean cyclone evolution.

4.2 Materials & Methods

4.2.1 Cyclone tracks and atmospheric conditions

Mediterranean cyclone tracks are taken from a new dataset provided by [235]. It consists of composite cyclone trajectories and intensities detected by ten different cyclone detection and tracking methods applied to hourly data of the ERA5 reanalysis [236] in the 42 years of 1979-2020. In the following work, the cyclones tracked by at least five of the ten tracking algorithms (confidence level of five) were retained. Such a confidence level is a trade-off between "robustness" and "completeness" of the final dataset and has already been used in other studies [237]. The original cyclones of [235] have been tracked on the Extended Mediterranean Sea Region: -20°E;45°E;20°N;50°N. To focus only on Mediterranean Cyclones, Atlantic Cyclones have been discarded by reducing the domain to: 6°W;45°E;30°N;50°N. The cyclones that stay less than six hours over the Mediterranean Sea have also been discarded to not take into account the thermal lows present over the Sahara desert.

The maximum intensity of the cyclone is defined as the lifetime minimum Sea Level Pressure, SLP, at the cyclone center, and the first time this minimum is reached is defined as time 0. Data are then organized into an intensification phase (before time 0) and a weakening phase (after time 0), although in a few cases, short re-intensification periods might occur.

Based on the position of the tracked cyclones, hourly 3D fields of temperature, moisture, wind, rainfall, geopotential height, heat fluxes, and potential vorticity have been extracted from the ERA5 reanalysis dataset in an area of $10° \times 10°$ surrounding the center of the depression. Anomalies have been computed as departures from the climatological seasonal cycle, computed as a 7-day running mean of the daily mean values over the 42 years.

4.2.2 Hart cyclones phase space diagram

The cyclone phase space (CPS) diagram [85] has been applied to distinguish between typical asymmetric ETC with a cold inner core and axisymmetric tropical-like cyclones (TLC) with a deep inner warm core. To construct this CPS, three parameters are needed:

- B, the thermal asymmetry of the cyclone in the lower troposphere.
- V_l, the lower tropospheric thermal wind
- V_u, the upper tropospheric thermal wind

Those parameters are computed using the geopotential height field Z at three different vertical levels (900 hPA, 600 hPA, and 200 hPA) within a circle of radius 1.25° around the cyclone center. They are mathematically defined as follows:

$$B = \overline{Z_{600}(\mathbf{x},t) - Z_{900}(\mathbf{x},t)}\Big|_R - \overline{Z_{600}(\mathbf{x},t) - Z_{900}(\mathbf{x},t)}\Big|_L \tag{4.1}$$

where the over-bar indicates the mean over the area of a semicircle of radius 1.25°, located to the right (subscript R) or to the left (subscript L) of the storm trajectory.

$$-|V_l| = \frac{\partial(\Delta Z)}{\partial \ln(p)}\Bigg|_{900}^{600} \tag{4.2}$$

$$-|V_u| = \frac{\partial(\Delta Z)}{\partial \ln(p)}\Bigg|_{600}^{200} \tag{4.3}$$

with $\Delta Z = max(Z) - min(Z)$ (at the same pressure level, in a region of radius 1.25° around the cyclone center).

The choice of a 1.25° (or 137.5 km) radius was justified as several studies have shown that the original 500 km radius of [85] is too large for Mediterranean cyclones. For instance, [238–240, 226] reduced the radius to 150 km, while [230, 241, 224] reviewed different approaches and performed sensitivity tests, reporting that choosing values between 70 km and 150 km did not make significant changes in the categorization. [229] also demonstrated that results obtained with 150 km are consistent with those obtained at 300 km. Importantly, it is worth noting that, also in [231], despite cautionary remarks, the CPS diagram presented in their work was computed using a 150 km radius.

In this context, the choice of 137.5 km falls within the range commonly adopted in the literature and is consistent with the reduced spatial scale of medicanes. It should be acknowledged that using a small radius could be a limitation for the diagnosis of cyclone symmetry; however, this issue is partly mitigated by the fact that most tracking algorithms used in [235] already

apply explicit symmetry criteria when identifying a cyclone. The extent to which the radius size would affect the determination of the upper-level core temperature nonetheless remains an open question.

In Hart's view, a tropical cyclone is a non-frontal system characterized by thermal symmetry, while an ETC is a frontal system that is thermally asymmetric. Mature TC have values of B of approximately zero, while developing ETC have large positive values of B. The symmetry condition for distinguishing a TC from an ETC is conventionally set at $|B| < 10$ m.

The parameters V_l and V_u instead are related to the radial gradient of temperature in the cyclone. In a cold-core structure, the geopotential height perturbation increases with height. Cold-core structures like ETC have negative values for both $-V_l$ and $-V_u$. Conversely, in a warm-core structure, the geopotential height perturbation is larger closer to the surface than at higher levels. Warm-core structures like TC have positive values for both $-V_l$ and $-V_u$. Hybrid and transitioning cyclones may have a sign of $-V_l$ that is different from $-V_u$.

In the present study, following the work of [230, 242, 239, 243], Deep Warm Core Cyclones (DWCC) are defined as cyclones that during part of their lifetime develop a deep warm core: both $-V_l$ and $-V_u$ must be positive for at least six hours while they are over the sea. It has to be emphasized that thanks to ERA5 hourly resolution, $-V_l$ and $-V_u$ were computed for each hour of the cyclones' lifetime; so to be classified as a DWCC, a cyclone must have a deep warm core for six hourly time-steps. The ETC are the ones with a cold core, i.e., they have negative values for both $-V_l$ and $-V_u$, for their whole lifetime, or they have a short-duration positive value for $-V_l$ only (less than six hours). The remaining cyclones, i.e., those with a different sign for $-V_l$ and $-V_u$, are considered as hybrid and are not included in the study.

In the present dataset, adding the B parameter threshold criterion to discriminate DWCC from ETC decreases the number of warm core cyclones by 5%. This is likely because most tracking algorithms used in [235] are already considering symmetry criteria to identify a structure as a cyclone. Therefore, in this work, only core temperature ($-V_l$ and $-V_u$ parameters) was used to discriminate between ETC and DWCC.

4.2.3 Potential Intensity

Potential Intensity (PI) represents the theoretical maximum intensity a tropical cyclone (TC) can attain under specific environmental conditions. It is determined by different thermodynamic factors such as sea surface temperature, atmospheric temperature in the air column, and moisture availability. Following many influential studies [244–248], and others, the computation of PI based on [249] was adopted:

$$PI^2 = \frac{C_k}{C_d}\frac{T_s}{T_o}(CAPE^* - CAPE_{env}) \tag{4.4}$$

where C_k and C_d are the surface exchange coefficients for enthalpy and momentum; T_s and T_o are the sea surface and outflow temperatures; $CAPE^*$ is the convective available potential energy of an air parcel lifted from saturation conditions at the sea surface temperature (referred to as *hurricane CAPE* in the following), and $CAPE_{env}$ is the convective available potential energy of a near surface air parcel (referred to as *environmental CAPE* in the following).

The potential intensity and the CAPE variables were computed using the Python packages described in [250]. The function takes as input ERA5 sea surface temperature (SST), and temperature and relative humidity profiles at the following pressure levels: 2m, 900hPa, 850hPa, 700hPa, 500hPa, 400hPa, 300hPa, 200hPa, 100hPa, and 50hPa. Following [250, 251, 246], the ratio $\frac{C_k}{C_d}$ was set to 0.9.

In computing the SST and PI composites over the previously mentioned $10° \times 10°$ areas, grid cells that were over land have been excluded (see the percentage of cells concerned **fig. B.1 & B.2**). Then, a sensitivity test was performed by assigning $PI = 0\ m.s^{-1}$ in grid points over land areas. While this adjustment significantly reduces the box-averaged PI values, the results of the analysis remain qualitatively unchanged, indicating that the general conclusions of the work are not sensitive to the way in which land points are treated.

4.3 Results

4.3.1 Classification of cyclones

Considering all the criteria previously mentioned, over the 42-year study period, the total number of cyclones present in the dataset is 2026, located in the Mediterranean Sea and the Black Sea. Of those 2026 cyclones, an average of 23 cyclones per year are classified as ETC cyclones (959 cyclones in total), and 3.4 cyclones per year are classified as DWCC cyclones (142 cyclones in total). The rest are intermediate or hybrid cyclones, which were not considered in the following study. Most of the cyclones identified as medicanes in the scientific literature are present in the DWCC group. These include Callisto (09/27/1983), Celeno (1/14/1995), Rolf (2011-11-06), Trixi (2016-11-01), and Ianos (2020-09-17). Others identified as Medicanes by [252] and [229] are not considered in the present study, as, according to the present definition, they never developed a deep warm core (Leucosia, 1982-24-01; Zeo, 2005-12-13; Ilona, 2014-01-19; only had a low-level warm core). Furthermore, the DWCC group also includes other cyclone types, such as warm seclusions, as previously mentioned.

To ensure a meaningful comparison between categories, the ETC were further divided according to intensity: the 15% ETC with the lowest Sea Level Pressure (SLP) values were classified as "Strong ETC" (SETC). This subgroup contains 144 cyclones, a number deliberately chosen to be close to the size of the DWCC sample (142 cyclones), thereby making the two groups more comparable. The remaining 815 cyclones are thereafter labeled as "WETC" and

referred to as weak extratropical cyclones. To test the robustness of this classification, the analysis was repeated, defining SETC as the 20% of ETC with the lowest SLP, and then based on maximum wind speed instead of minimum SLP. The alternative definitions produced results consistent with what is shown in **section 4.3.3**.

To construct composites consistently across all cyclones, time $t = 0$ is defined as the moment of maximum intensity, identified as the minimum SLP. This common reference point allows for a homogeneous comparison between categories. The evolution of the number of DWCC and SETC in the period from 36 h before to 36 h after the cyclones' maximum intensity is shown in **fig 4.1**, with the count decreasing both for negative and positive time intervals due to the limited duration of the tracks. On average, the tracks last 64 hours for normal and SETC, while they last much longer (89 hours) for DWCC, the difference between the classes being statistically significant at the 99.9% confidence level. It is also worth noting that the average duration of the warm core in DWCC is 13.5 hours.

Figure 4.1 also presents the proportion of DWCC that have a full warm core (positive values for both $-V_l$ and $-V_u$) at any given time lag from 0. About 40% of DWCC have a full warm core at the time of peak intensity, developed in most cases less than 6 hours before, and a total of 75% have at least a lower or an upper warm core at time t=0, while the remaining DWCC develop a warm core in the subsequent hours. Importantly, the timing of maximum intensity does not coincide with the warm-core transition itself: in many cases, the warm core develops well after peak intensity, while in others it is already established several hours beforehand. However, what matters for this analysis is that at 36 hours before the maximum intensity, none of the cyclones in the DWCC category present a deep warm core. It means that they are still in their typical cold core or hybrid conditions at those time-steps. For this reason, the difference in the tropospheric conditions between ETC and DWCC at 36 hr before the peak intensity is investigated in **section 4.3.3** to identify possible precursors to the development of the deep warm core.

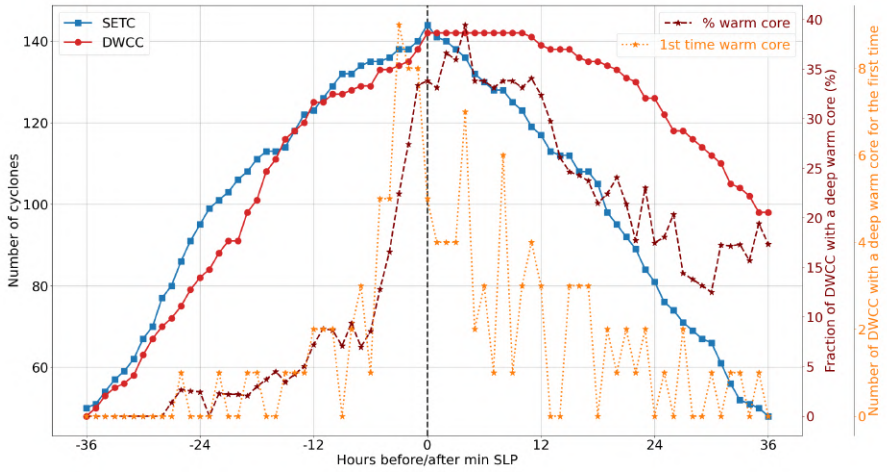

Fig. 4.1 Time evolution with respect to minimum SLP of the number of SETC (blue solid line) and DWCC (red solid line), proportion of DWCC that have a warm-core at each time step (maroon dashed line), and number of DWCC that have a deep warm core for the first time (dotted orange line).

4.3.2 General characteristics

Cyclones in the Mediterranean are known to occur preferentially in specific regions, including the Gulf of Genoa, the Adriatic Sea, the Black Sea, close to Cyprus, and in northwest Africa, at the leeward side of the Atlas Mountains [253–255, 90, 256–259]. As revealed in **fig. 4.2**, which shows the spatial density of tracks separated into ETC and DWCC, the overall distribution of the cyclones analyzed in this study matches the geographical localization of Mediterranean cyclones, but cyclones of different categories are preferentially located in different positions. Most SETC are mainly located in the Gulf of Genoa, while cyclones that develop a warm core are mainly present in the western Mediterranean Sea and the Ionian Sea, with some present in the Black Sea, in line with previous studies [65, 223]. At 36 hours before maximum intensity, the time at which environmental conditions are examined in the following section, it is important to note that only about one-third of SETC have their centers located over the sea, compared to roughly one-half of DWCC. This difference is consistent with the already mentioned role played by the air-sea exchanges in the development of DWCC.

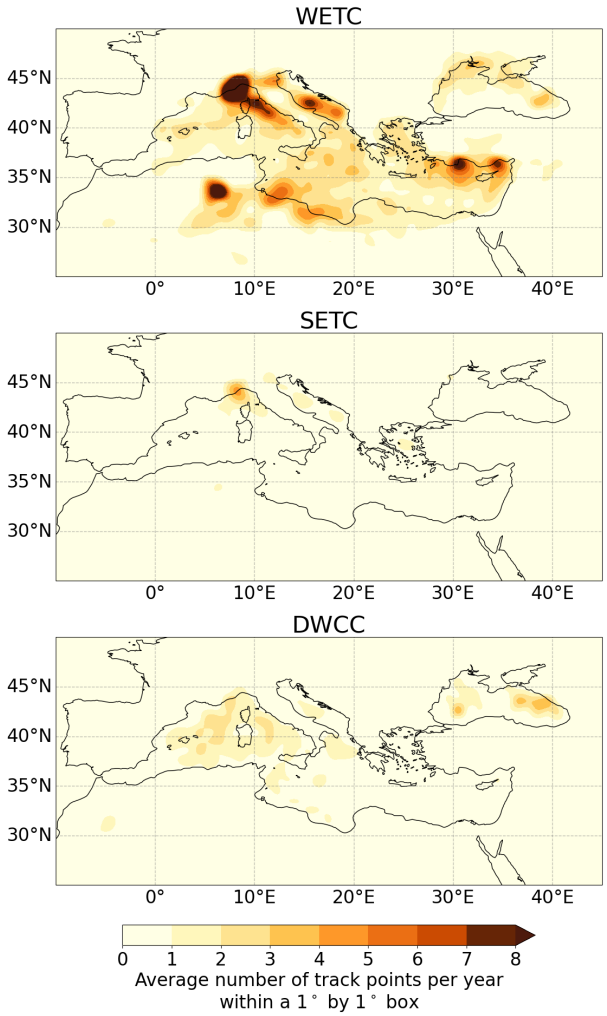

Fig. 4.2 Spatial density of cyclone tracks expressed as the average count of track points per year within a $1° \times 1°$ box.

The seasonality of Mediterranean cyclones indicates a preferential occurrence in spring and fall [90]. This is reflected both in the occurrence of ETC and DWCC (see **fig. 4.3**). Several studies have similarly shown that Mediterranean cyclone activity often peaks during the transition seasons, with enhanced cyclogenesis in spring linked to increasing surface temperatures, strong land–sea thermal contrasts, and elevated atmospheric moisture availability [260, 261, 17, 262].

SETC occurrence presents a well-defined maximum in winter and early spring, while some works have found that the most intense Mediterranean cyclones are more frequent in winter [263, 88]. This apparent discrepancy highlights that the seasonality of intense systems is highly sensitive to the dataset, boundary conditions, and criteria used to define cyclone intensity. Indeed, different thresholds or forcing data can substantially alter the simulated seasonal distribution, as already shown in [263].

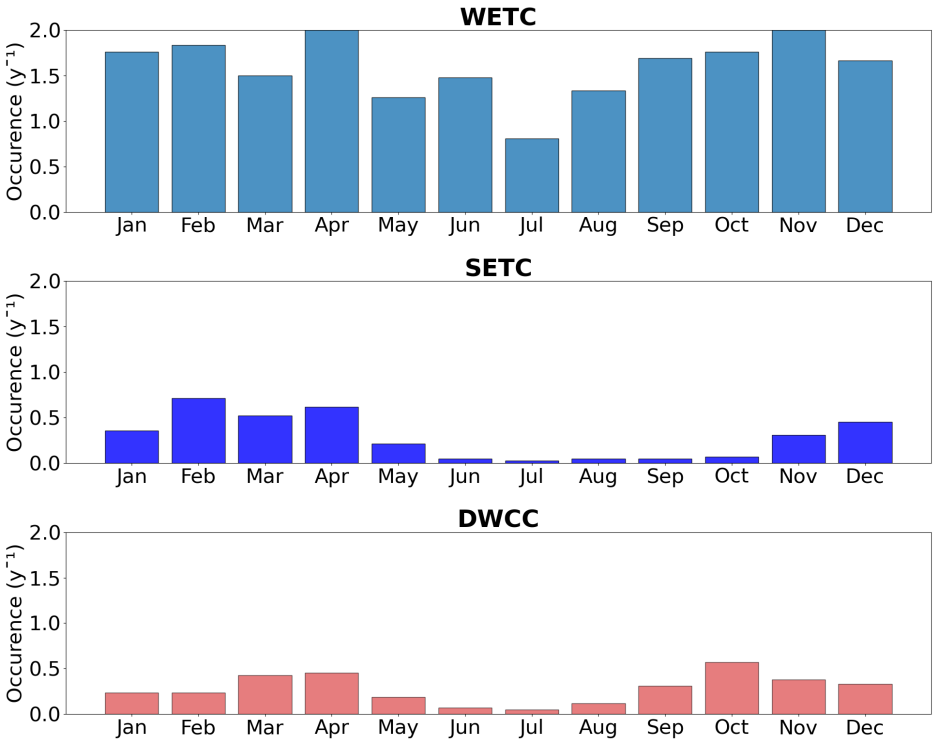

Fig. 4.3 Seasonal cycle of WETC (light blue, top row), SETC (dark blue, middle row), and intense DWCC (red, bottom row) occurrence, counted at their time of maximum intensity.

DWCC are most frequent in October, when the large SST favor air-sea heat exchanges and therefore promote the establishment of the warm core [242]. However, several DWCC are also found in spring.

The different seasonality of ETC' and DWCC' occurrence is reflected in the composite sea surface temperature over which they develop, shown in **fig. 4.4**. At 36 hours before peak intensity, SST is about 3^{o}C warmer for DWCC than for SETC. In addition, a two-sample t-test comparing the mean values of the 10% highest SST values in the $10° \times 10°$ box shown in the top panel of **fig. 4.4** shows that the SST associated with DWCC significantly differ from the SETC ones at a 95% confidence level.

Thereafter, all mentions to statistical outcomes will refer to this two-sample t-test comparing the mean values over the 10% highest values of the $10° \times 10°$ box at a 95% confidence level. The selection of the 10% highest values is motivated by the fact that the 10°x10° box is very large, and it includes areas that are not representative of the cyclone conditions. On the other hand, selecting a smaller area at a fixed location with respect to the cyclone center is not appropriate as different variables express anomalous values at different places (e.g., wind speed is typically larger in the southwest quadrant, while precipitation maxima are on average larger to the north of the center, and PV intrusion is in the northwest quadrant). For these reasons, a fixed-size area covering 10% of the 10°x10° box is defined by selecting the largest values, regardless of their position in the box. A sensitivity analysis was also performed over the area fraction used (5%,

25%, and 100%, in addition to the 10% reported here), yielding similar conclusions to those presented in the following.

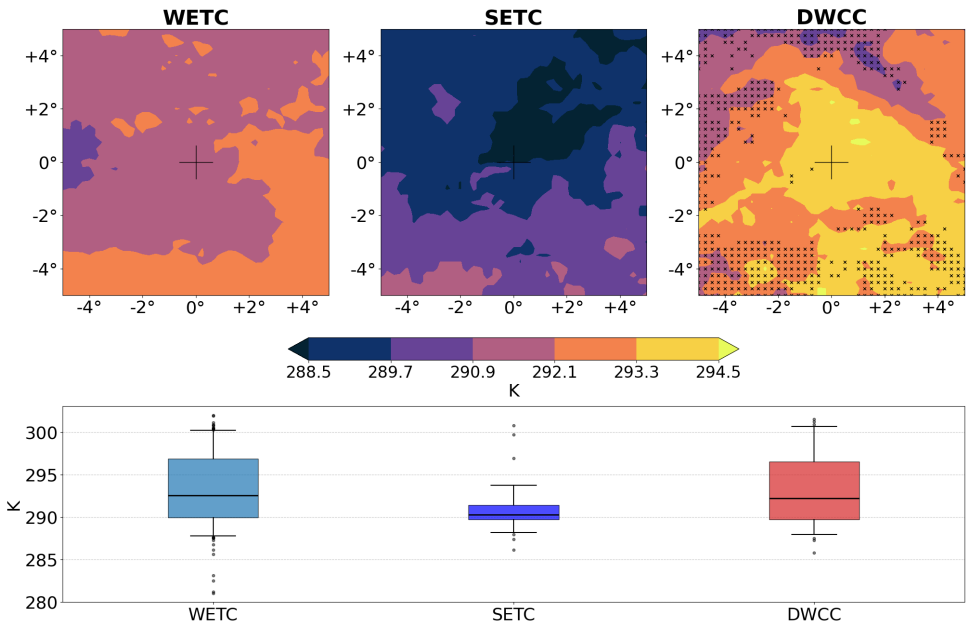

Fig. 4.4 Sea Surface Temperature (SST) for the different cyclone classes. Top: 2D composites centered on the cyclones, 36h before the time of minimum SLP. The markers in the right panel indicate regions where DWCC composited SST is not significantly different from SETC (95% confidence level). Bottom: boxplots of the mean SST for each cyclone, where the mean is computed on the 10% highest values over the 10°x10° box for each cyclone. Boxplots show the median value (horizontal line), the inter-quartile range (colored area), the 5th and 95th percentiles (whiskers), and outliers.

ETC and DWCC are also characterized by different peak intensities: the largest SLP anomaly is on average -10 hPa for WETC and -17 hPa for DWCC, whereas SETC are on average even stronger than DWCC (in terms of their depression, which averages at -21 hPa). Consistently, peak winds are comparable between SETC and DWCC, and are much smaller in WETC (**fig. 4.5**). This is confirmed by the two-sided t-test mentioned above, giving no statistically significant difference between the mean values for DWCC and SETC surface wind.

In DWCC, the maximum azimuthally averaged winds are found closer to the center than in ETC (see **sup. fig. B.4**). However, large heterogeneities exist as the standard deviation of the radius of maximum winds is over 100 km in all classes. Finally, wind composites (**fig. 4.5**) have a maximum in the southwest quadrant, on the right of their direction of propagation (**sup. fig. B.6**) given by the wind rose shown in the **supplementary figure B.3**.

A major difference emerging between DWCC and SETC is in their associated precipitation: even though the cyclone intensity between the two categories is similar, hourly rainfall is much higher in DWCC, where the azimuthal average peaks to values that are 40% larger than for SETC (**fig. 4.6** and **sup. fig. B.5**). Indeed, the mean precipitation over the grid points with the upper decile rainfall rate is significantly larger for DWCC than for SETC, even if very intense rainfall

can be present in some cold-core cyclones, as shown by the outliers present in the boxplots of **figure 4.6**.

Building on the tropical-cyclone literature, which has shown that rainfall intensity can be at least as important as wind speed in determining cyclone-related socioeconomic losses [264–266], these composites indicate that DWCC have the potential to produce more severe impacts than their extratropical counterparts.

The precipitation at the peak intensity of ETC is localized in the North-East quadrant (**fig. 4.6**). This spatial distribution is similar to the one reported in the literature for typical extratropical cyclones associated with the presence of the warm-frontal region [267–269], and matches the one described in [270] for Mediterranean cyclones interacting with the warm conveyor belt that advects moist air into the system.

The maximum precipitation for the warm-core cyclones is found in the North-West quadrant (**fig. 4.6**), as already presented in [225]. Usually, the peak of rainfall in TC occurs at the forefront of the storm center, where the uneven circulation induced by friction in the moving storm generates low-level convergence, significantly intensifying deep convective activity [271, 272]. This is partially confirmed by the composites oriented along the direction of propagation (**sup. fig. B.7**).

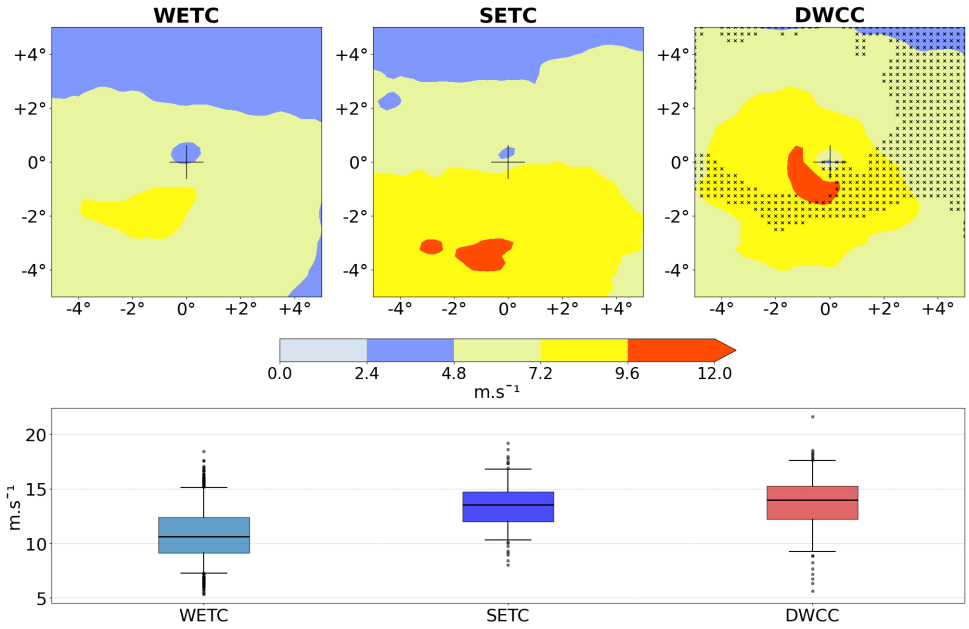

Fig. 4.5 10m surface wind for the different cyclone classes. Top: 2D composites centered on the cyclones, at the time of minimum SLP. The markers in the right panel indicate regions where DWCC composited surface wind is not significantly different from SETC (95% confidence level). Bottom: boxplots of the mean surface wind for each cyclone, where the mean is computed on the 10% highest values over the 10°x10° box for each cyclone. Boxplots show the median value (horizontal line), the inter-quartile range (colored area), the 5th and 95th percentiles (whiskers), and outliers.

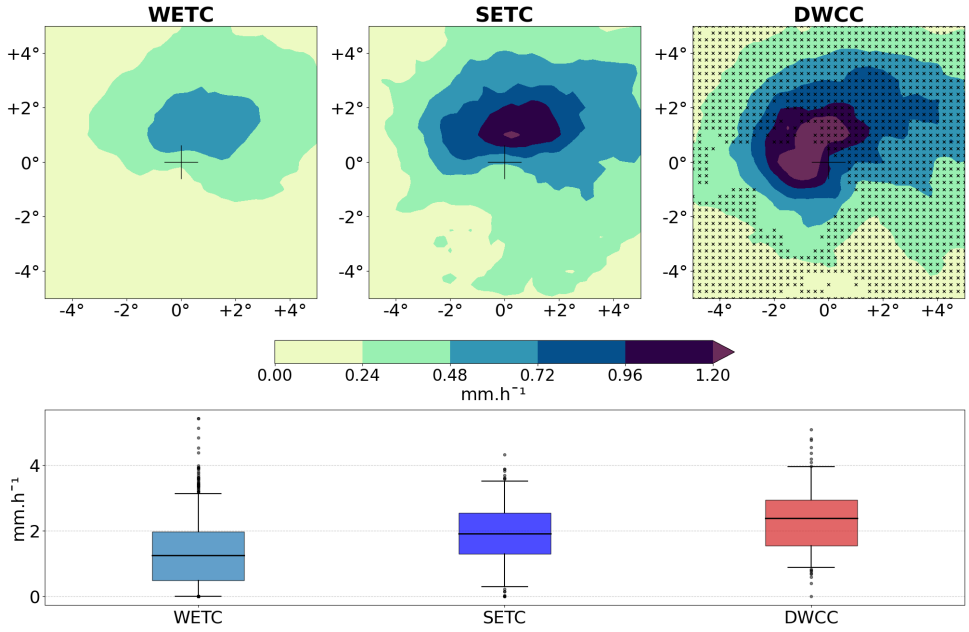

Fig. 4.6 Hourly precipitation for the different cyclone classes. Top: 2D composites centered on the cyclones, at the time of minimum SLP. The markers in the right panel indicate regions where DWCC composited hourly precipitation is not significantly different from SETC (95% confidence level). Bottom: boxplots of the mean hourly precipitation for each cyclone, where the mean is computed on the 10% highest values over the 10°x10° box for each cyclone. Boxplots show the median value (horizontal line), the inter-quartile range (colored area), the 5th and 95th percentiles (whiskers), and outliers.

4.3.3 Intensification phase

The composite evolution of surface wind speed in the different cyclone categories is shown in **figure 4.7**. In this case, wind speed has been averaged over a 4° by 4° longitude-latitude box centered at the minimum sea level pressure location. The choice of the 4° × 4° box was based on inspection of the two-dimensional composites, which show that this region typically encompasses the area of maximum wind and surface flux intensities around the cyclone center. A smaller box (e.g., 2° × 2°) would exclude part of this high-intensity region for many systems, while a larger one would include unrelated environmental signals. To assess the sensitivity of the results to this choice, calculations were repeated using box sizes ranging from 10° × 10° down to 2° × 2°. The resulting evolution of wind and heat fluxes was very similar across all cases, confirming the robustness of the findings. Finally, all computations excluded land areas, as wind speeds over land can be biased, either exaggerated by orography or reduced by friction.

As for the 2D surface wind composites (**fig. 4.5**), **figure 4.7** also indicates similar peak intensities for DWCC and SETC. However, their intensity evolution is quite different, indicating a statistically significantly larger intensification rate for DWCC in the earlier stages, triggered by larger air-sea (latent and sensible) heat fluxes (**fig. 4.8**; latent fluxes only can be observed **sup. fig. B.9**). SETC, even though they have stronger surface winds than WETC, exhibit surface fluxes quite similar to WETC, suggesting that the wind-induced surface heat exchange (WISHE)

feedback is not active in those cases, whereas it can drive the evolution of DWCC. To investigate possible reasons for the observed differences, the conditions under which cyclones develop are analyzed, focusing on the environmental characteristics at the location where they are 36 hr before their peak intensity, when none of them has yet developed a deep warm core.

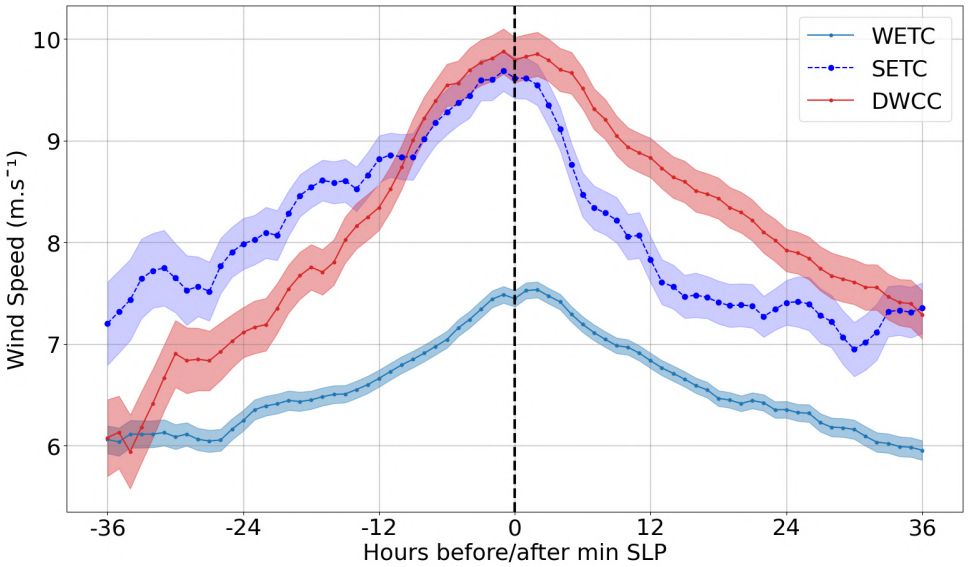

Fig. 4.7 Composite time evolution of mean 10-m wind speed in a 4° by 4° box centered on the cyclone. Only the points over the sea are considered to compute the composite. The vertical black dashed line indicates the time of minimum sea level pressure. Shading around the solid line indicates the standard error of the mean.

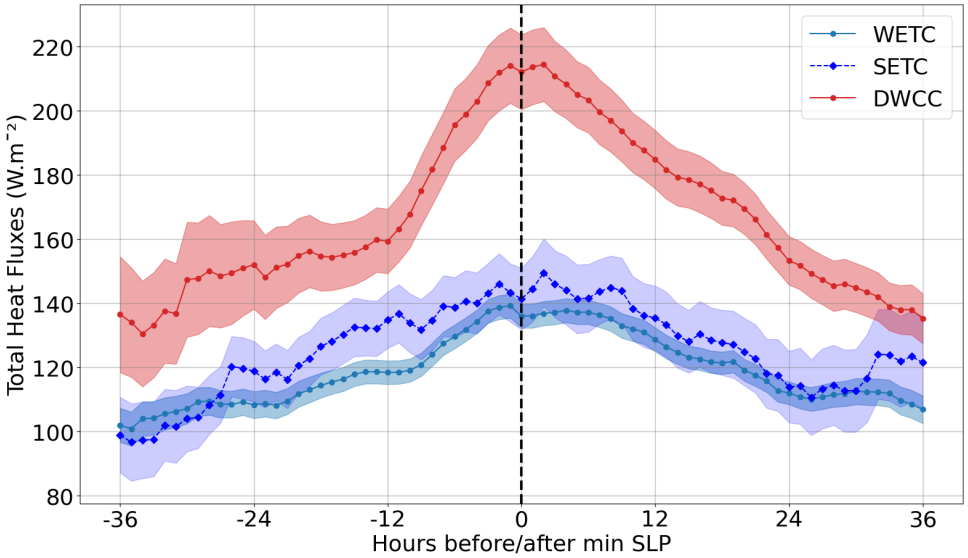

Fig. 4.8 Composite time evolution of mean air-sea total (latent and sensible) heat flux in a 4° by 4° box centered on the cyclone. Only the points over the sea are considered to compute the composite. The vertical black dashed line indicates the time of minimum sea level pressure. Shading around the solid line indicates the standard error of the mean.

As already mentioned in the introduction, the origin of Mediterranean cyclones is the presence of a trough in the upper troposphere. The meandering of the jetstream advects positive potential vorticity (PV) anomaly into the region and is associated with cyclone development [273, 274]. It also favors upper-level divergence, upward motion, and the intensification of the surface depression. The positive upper-level PV anomaly is present in the analyzed cyclones, as shown in the 300hPa composite maps 36h before the cyclone peak intensity (**fig. 4.9**). The average PV anomaly is relatively weak for WETC, and larger for SETC and DWCC, with no statistically significant difference observed between the mean PV anomaly of DWCC and SETC. In addition, the very large differences among cyclones of the same class indicate that the PV anomaly strength is neither a sufficient nor necessary condition for DWCC development.

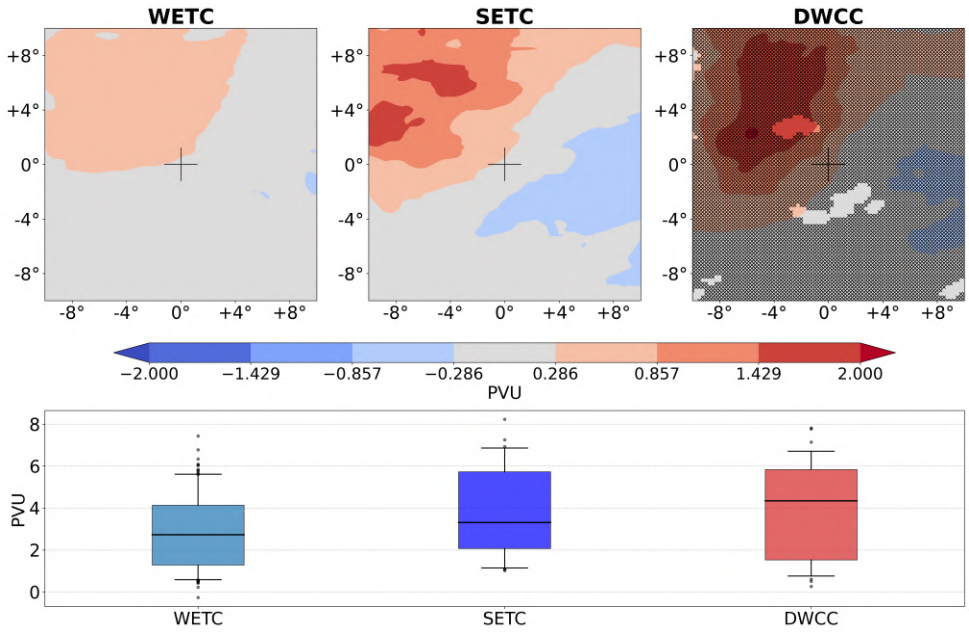

Fig. 4.9 300hPa Potential Vorticity (PV) anomaly for the different cyclone classes. Top: 2D composites centered on the cyclones, 36h before the time of minimum SLP. The markers in the right panel indicate regions where DWCC composited PV anomaly is not significantly different from SETC (95% confidence level). Bottom: boxplots of the mean PV anomaly for each cyclone, where the mean is computed on the 10% highest values over the 10°x10° box for each cyclone. Boxplots show the median value (horizontal line), the interquartile range (colored area), the 5th and 95th percentiles (whiskers), and outliers.

Composite maps of potential intensity 36 hr prior to peak intensity are shown in **fig. 4.10**. DWCC have PI values exceeding the threshold typically associated with tropical cyclone development ($> 35\ m.s^{-1}$; [6]), while PI is statistically significantly lower for WETC and SETC. The DWCC high PI region is present in proximity of the cyclone center, suggesting that the perturbation itself contributes to increasing the potential intensity in an environment overall less prone to TC development, as discussed in [275].

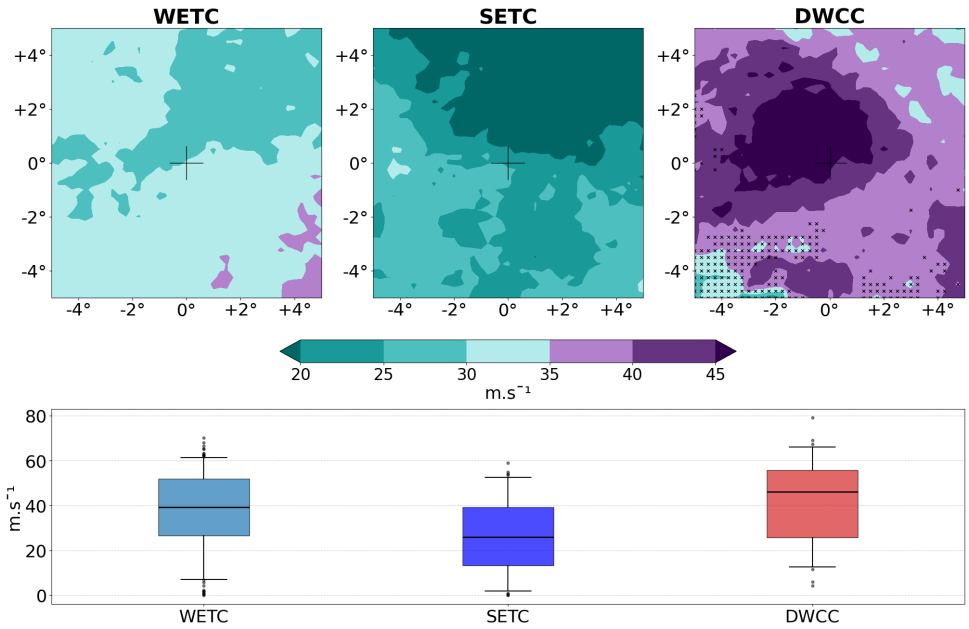

Fig. 4.10 Potential Intensity (PI) for the different cyclone classes. Top: 2D composites centered on the cyclones, 36h before the time of minimum SLP. The markers in the right panel indicate regions where DWCC composited PI is not significantly different from SETC (95% confidence level). The purple colors represent values of PI above 35 $m\ s^{-1}$, value below which tropical cyclones typically don't form [6]. Bottom: boxplots of the mean PI for each cyclone, where the mean is computed on the 10% highest values over the 10°x10° box for each cyclone. Boxplots show the median value (horizontal line), the interquartile range (colored area), the 5th and 95th percentiles (whiskers), and outliers.

To delve into the origin of the differences in potential intensity across the different classes, the PI was computed from the climatological conditions. Climatological conditions are obtained as long-term averages of the relevant fields (temperature, moisture, and SLP) at the same location and time of the year of each analyzed cyclone. A stronger climatological PI is obtained for DWCC than for SETC (**fig. B.10**). This difference has an average magnitude of 12 $m.s^{-1}$ and is statistically significant. It is associated with their different seasonality, as DWCC occurrence peaks in fall (**fig. 4.1**), when the larger SST (**fig. 4.4**) are associated both to a larger magnitude of the temperature ratio term $\frac{SST}{T_o}$ and of the hurricane CAPE term in eq. (4).

However, the climatological PI associated with DWCC presents less intense values than the actual PI obtained at their formation, indicating that there are some specific conditions when DWCC develop which increase the local PI value, resulting in a composite PI anomaly (actual minus climatological value) of up to 13 $m\ s^{-1}$ (**sup. fig. B.11.a**), and with a mean of 6 $m\ s^{-1}$. The main contribution to such an anomaly in PI for DWCC is due to the anomalous CAPE difference term in **eq. 4**, while the SST/T_o temperature ratio does not significantly differ from its climatological value (see **sup. fig. B.11.b** and **B.11.c**).

The CAPE difference term depends on sea surface temperature, on near-surface specific humidity (here taken at 2m asl), and on the temperature profile in the whole air column. To determine which variable has the most important influence on the anomaly produced in PI

for DWCC, the CAPE difference term inserted in the PI derivation is computed using all climatological values except one.

For instance, climatological values of near-surface specific humidity and tropospheric air temperature are held fixed, while the actual values of SST are inserted. This allows an anomalous hurricane CAPE to be computed and subsequently used in the PI calculation. The difference between the resulting PI and the climatological PI therefore isolates the impact of the SST anomaly on hurricane CAPE alone. This contribution is then composited across the different DWCC, as shown in **figure 4.11a**.

The procedure is then repeated for anomalous near surface specific humidity (here taken at 2m asl, which affects the buoyancy of the near surface air parcel), for anomalous near surface air temperature (which again affects the buoyancy of the near surface air parcel), and for the rest of the tropospheric temperature profile (which enters in the computation of the parcel CAPE). All the different terms are shown in **figure 4.11**.

They indicate that the negative anomaly in the mid-troposphere air temperature (see **sup. fig. B.12**) has the largest effect, followed by the positive SST anomalies. The anomalies in near-surface air properties have a minimal effect. The negative anomaly in tropospheric temperature increases the density of the environmental air, contributing to the hurricane CAPE increase. The positive SST anomaly increases the buoyancy of the saturated parcel used to compute hurricane CAPE. Together, the two anomalies significantly increase the hurricane CAPE and thus the PI with respect to climatological conditions. The linear superposition of the PI anomalies shown in **figure 4.11** provides a total anomaly very close to the full one, indicating that nonlinear effects are small.

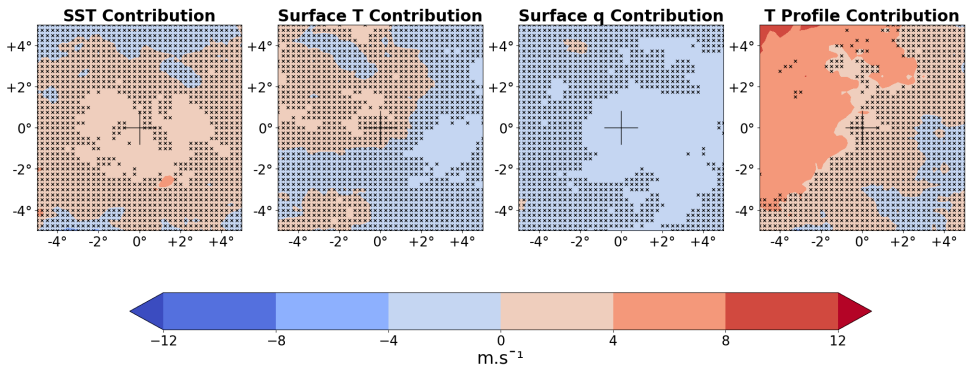

Fig. 4.11 2D composites of PI anomalies ($m.s^{-1}$) for DWCC 36h before their minimum SLP. Each panel shows the difference between (a) the PI computed using climatological values except for the CAPE difference term, and (b) the climatological PI (**sup. fig. B.10**). The CAPE difference term in (a) is computed with climatological fields except one, for which the actual field present at the time of the storm is used. This field is, from left to right panels: SST, 2m temperature, 2m specific humidity, and air column temperature profile. The markers indicate the anomalies that are not significantly different from 0 at the 95% confidence level.

In addition to PI, the differences between the three categories of cyclones in the vertical wind shear have also been analyzed. Indeed, strong wind shear is known to have detrimental

effects on the development of tropical cyclones through its ventilation effects [276, 277, 74, 278], and its role on the formation of DWCC has been previously discussed [223, 230]. The DWCC studied here do present a statistically significant weaker wind shear than SETC (**fig. 4.12**), largely because of differences in the upper-level winds. At time t=-36hr, 300 hPa winds are stronger than in the climatology for all categories of cyclones, in line with their association with the meandering of the jet stream. However, they are less strong for DWCC and WETC than for SETC.

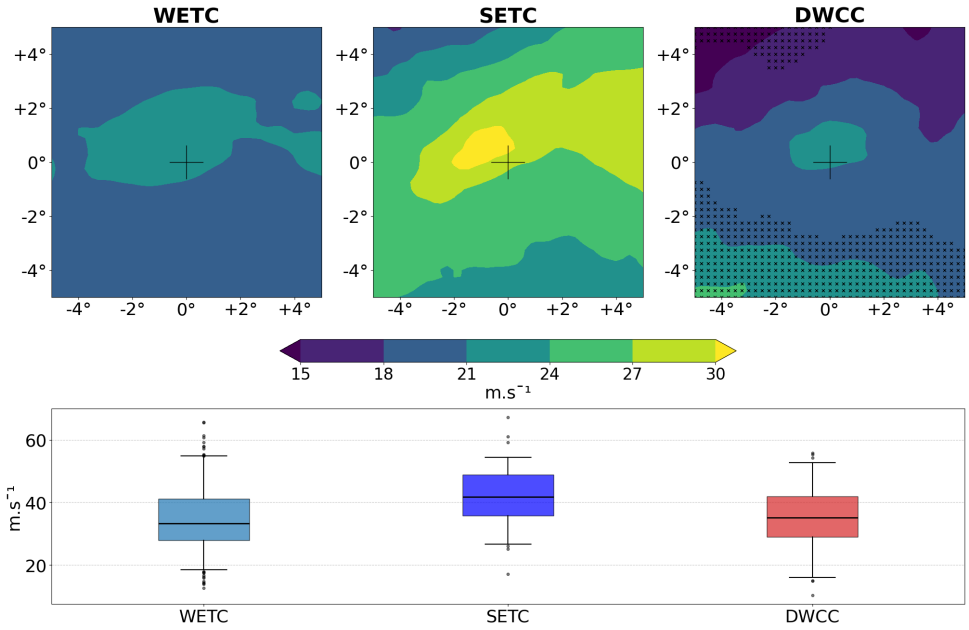

Fig. 4.12 Wind shear for the different cyclone classes. Here, the wind shear is defined as the difference between the wind at 300hPa and the wind at 850hPa. Top: 2D composites centered on the cyclones, 36h before the time of minimum SLP. The markers in the right panel indicate regions where DWCC composited wind shear is not significantly different from SETC (95% confidence level). Bottom: boxplots of the mean wind shear for each cyclone, where the mean is computed on the 10% highest values over the 10°x10° box for each cyclone. Boxplots show the median value (horizontal line), the interquartile range (colored area), the 5th and 95th percentiles (whiskers), and outliers.

In summary, the results show that, during their early stages, DWCC are typically characterized by higher potential intensity than ETC and evolve in environments with comparatively weak vertical wind shear. Both factors are conducive to the development of tropical-like features within cyclonic systems that are initially triggered by upper-level potential vorticity intrusions.

Although statistically significant differences in mean SST, PI, and wind shear are found between DWCC and SETC, the corresponding distributions exhibit substantial spread and overlap. Consequently, none of these environmental parameters alone provides a reliable discriminator between the two cyclone types. Rather, they should be interpreted as indicating environmental conditions that increase the likelihood of deep warm-core development.

4.3.4 Potential cause of the DWCC decay

Landfall is usually cited as an important cause of deprivation of moisture supply in tropical cyclones, causing their dissipation [279, 280]. However, in the present dataset, more than 75% of DWCC remain over the sea for 36hr after the peak intensity (**sup. fig. B.13**), while they significantly weaken **fig. 4.13** and in many cases loose their warm core. Thus, other processes could be responsible for the onset of the dissipation phase.

In **figure 4.13** the time evolution of DWCC potential intensity is shown between -36 hr and + 36 hr from time of peak intensity. A progressive decrease of the PI with time can be noticed starting already in early stages and certainly before peak intensity.

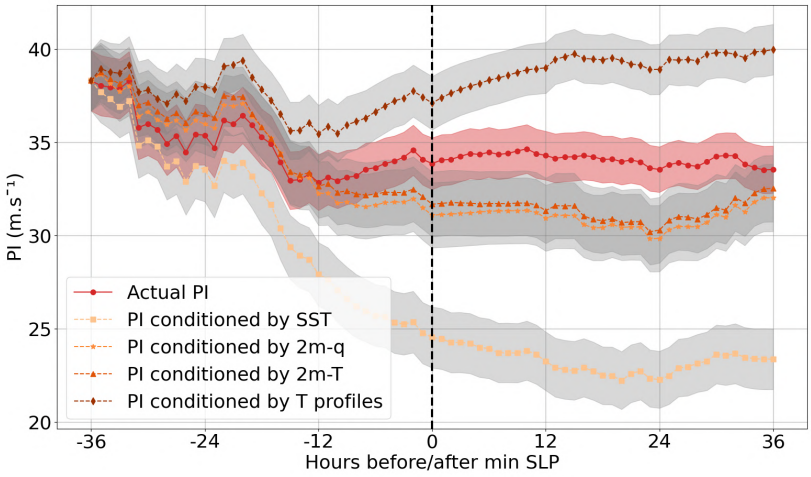

Fig. 4.13 Composite time evolution of the mean PI for DWCC with respect to their minimum SLP (black dashed line). The red solid line represents the actual mean PI. Other lines refer to PI computed letting only one variable evolve in time and all the others fixed at their initial value: SST (square markers), 2m-temperature (triangle markers), 2m-specific humidity (star markers), tropospheric temperature profile (diamond markers). The mean has been computed in a 4° by 4° box centered on each cyclone. Shading around the solid line indicates the standard error of the mean.

The reader can notice that at the same time there is a considerable reduction in SST (**sup. fig. B.8**). The reduction in SST along the trajectory of DWCC could be driven by the action of the strong cyclonic winds, which are well known to generate cold wakes on the tracks of TC [281]. In that matter, it can also be noticed that the translation speed of DWCC, and of SETC as well, significantly drops starting 12 hr before peak intensity (**sup. fig. B.14**). While the investigation of the reasons behind this change is beyond the scope of this work, it can be noted that a slower translation speed both causes a colder anomaly at the sea surface [282] and leads to the cyclone spending more time over cool water. Those mechanisms generate a reduction in the air-sea fluxes because of the reduced thermodynamical disequilibrium between the upper ocean and the lower atmosphere associated with colder SST and are known to reduce the intensification rate of tropical cyclones [282].

The reduction in SST leads to a decrease in hurricane CAPE (i.e. the convective available potential energy of an air parcel lifted from saturation conditions at the sea surface temperature) that can ultimately result in lower PI. To investigate this influence, additional time evolutions of PI have been computed by holding all variables constant at their initial values (either at -36hr, or at the first available track time for cyclones with a later track onset), except for one: SST, near-surface specific humidity, near-surface temperature, or the full atmospheric temperature profile (**fig. 4.13**). Among these, the PI computed with varying SST and fixed other variables shows the largest decrease, suggesting that the SST drop can be considered one of the primary contributors to the PI reduction.

In this regard, it can be noticed that the DWCC composite SST reduction of 3K is a very strong anomaly, compared to the cold wakes of TC [281]. This strong cooling, and the potential large cold-wake feedback on cyclone intensity, can be attributed to the shallow mixed layer of the Mediterranean Sea—typically only 15–30 m deep in October [283], the month of largest DWCC occurrence. Such a shallow mixed layer enhances the effects of the cyclone-induced upwelling and vertical mixing, resulting in a large cooling at the surface.

Thus, those composites are consistent with the SST-controlled intensity feedback known to limit the strength of tropical cyclones. The decay of DWCC might be related to it, but it can also be associated with other dynamical factors, such as the evolving baroclinic environment and changes in the vertical wind shear. While the present analysis highlights the role of air–sea coupling and cold-wake feedbacks as key contributors to the post-peak intensity decline, a detailed assessment of the relative importance and interactions among these processes is left for future work.

Interestingly, when the PI is computed by allowing only the atmospheric temperature profile to evolve while holding the SST and near-surface variables constant, a slight increase in PI is observed over time. A plausible physical explanation for such an intensification is the warming of the upper troposphere associated with the cyclone's own warm-core signature [76, 231]. Such an upper-level warming may reduce the environmental CAPE ($CAPE_{env}$) toward zero while the hurricane CAPE ($CAPE^*$) remains positive with the fixed warm SST, thereby increasing the difference $CAPE^* - CAPE_{env}$ that governs PI. This mechanism is consistent with the known sensitivity of PI to the thermodynamic structure of the environment [249] and highlights that, even in the absence of any SST change, the evolving atmospheric column alone can sustain or slightly increase the theoretical intensity limit of the cyclone.

4.3.5 Long-term evolution of different DWCC characteristics

The final part of this work examines whether trends associated with global warming can be detected in the DWCC datasets, which span 42 years from 1979 to 2020. To this end, time series were generated for a set of key DWCC metrics, and linear trends were estimated. For each trend,

a Student's t-test was applied under the null hypothesis that the slope equals zero. Trends are reported as statistically significant only when the p-value is below 0.05 (95% confidence level).

No significant decrease in the number of DWCC is found over the study period (**fig. 4.14**). Regarding their geographical distribution, no trend emerges in their mean latitude of occurrence (**fig. 4.15.a**), whereas a statistically significant westward shift in the cyclone tracks is detected, perhaps driven by a reduction of DWCC cyclones in the Levantine basin (**fig. 4.15.b**).

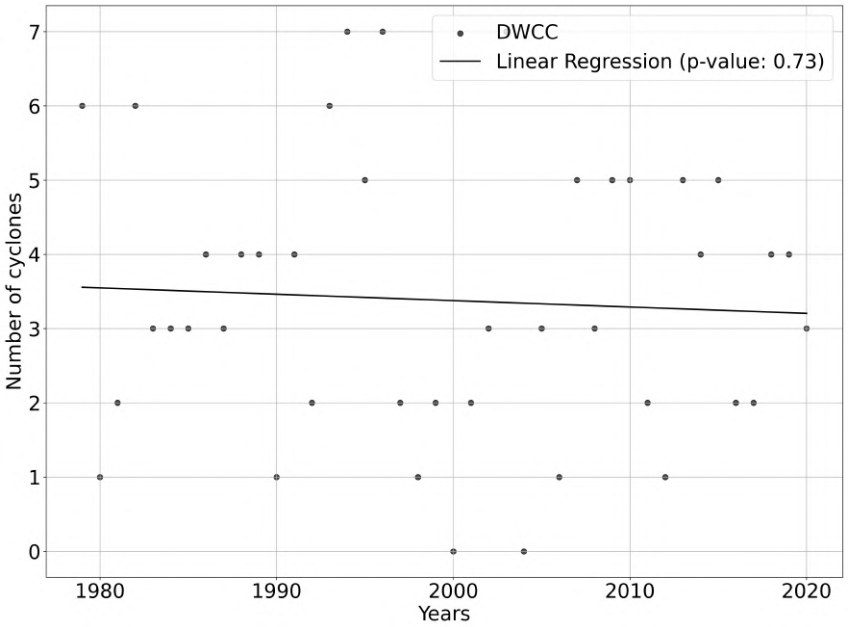

Fig. 4.14 Time series of the number of DWCC.

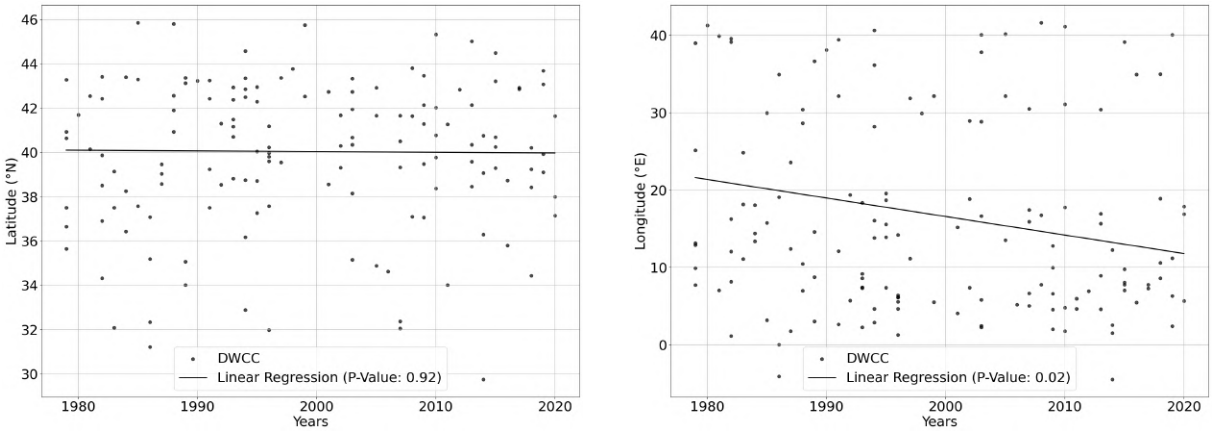

(a) Latitude

(b) Longitude

Fig. 4.15 Time series of the latitude (left) and the longitude (right) coordinates of the DWCC' center at the time of minimum SLP.

Physical conditions associated with DWCC exhibit significant changes over the study period. Sea-surface temperatures show a very strong and statistically significant increase (**fig. 4.16.a**), consistent with the robust and well-documented warming of the Mediterranean basin over recent

decades [284–286]. This regional amplification of ocean warming is a recognized feature of the Mediterranean climate system and is projected to continue throughout the 21st century under all emission scenarios. At the same time, upper level potential vorticity (PV) anomalies associated with DWCC display a significant decrease (**fig. 4.16.b**).

The observed decrease in PV anomaly intensity associated with DWCC likely reflects the robust large-scale dynamical trend of the jet stream migrating poleward [287, 288]. As the jet shifts northward, stratospheric PV intrusions, which act as the primary dynamical trigger for these cyclones, become less frequent and weaker in the subtropical genesis regions preferred by DWCC. However, interpreting this signal is complicated by the ongoing scientific debate regarding changes in jet stream "waviness" [289]. While a wavier jet could theoretically enhance meridional exchanges and potentially increase the frequency of PV streamers in certain sectors [290], the lack of consensus on these trends makes it difficult to definitively attribute the weakening PV signal to purely latitudinal shifts.

Beyond these dynamical considerations, an alternative and non-exclusive explanation involves the concurrent significant warming of the Mediterranean Sea (**fig. 4.16.a**). One hypothesis could be that the increase in SST lowers the threshold for the dynamical forcing required to trigger deep convection. As surface temperatures rise, the increased flux of sensible and latent heat enhances the moist static energy of the lower troposphere. Consequently, a less intense mid-level cold intrusion (associated with a weaker PV anomaly) may be sufficient to create the vertical instability and convective-prone environment that favor DWCC development. In this framework, the warming ocean essentially "compensates" for the weakening upper-level dynamical support.

This thermodynamic compensation might also explain why no such decrease in PV anomalies is associated with SETC (**fig. B.15**). As SETC development is more strictly tied to baroclinic instability rather than air-sea interaction, they do not benefit from the same "SST subsidy" as warm-core systems. Nevertheless, without a strong consensus on the evolution of jet stream waviness, interpreting these divergent trends remains challenging, and it is difficult to definitively explain the PV discrepancy without further sensitivity experiments. Future research should focus on quantifying the relative contribution of surface-based instability versus upper-level forcing to determine if DWCC are becoming increasingly "bottom-heavy" in their intensification processes.

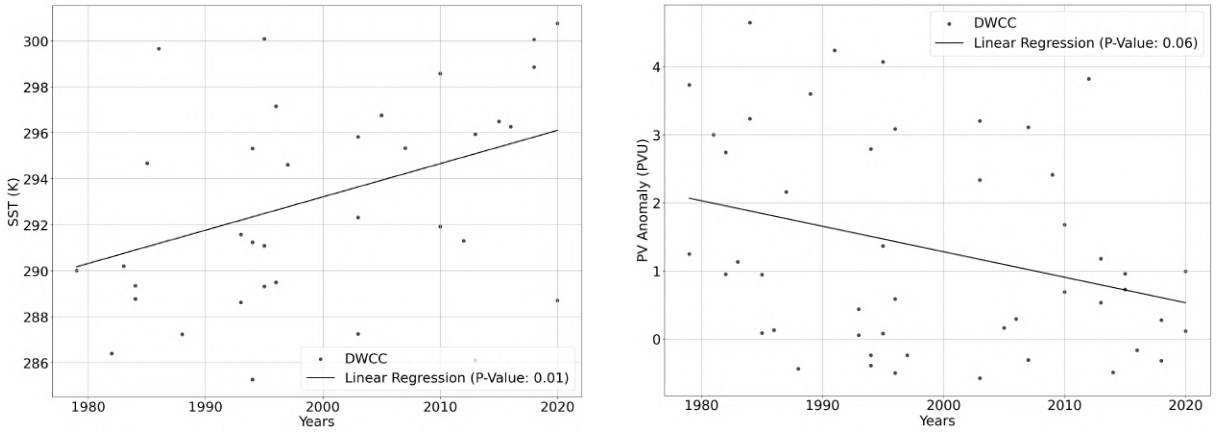

(a) SST (b) PV Anomaly

Fig. 4.16 Time series of the SST (left) and the 300hPa PV anomaly (right) average computed in a 4° by 4° box centered on each DWCC, 36h before their minimum SLP.

Concerning potential intensity, PI exhibits an upward trend consistent with the increase in SST, but the signal does not reach statistical significance (**fig. 4.17.a**). When PI is computed instead using the climatological values for the variables in **eq. 4.4** at the day and location of the cyclone, the upward trend is significant at a 90% confidence level (**fig. 4.17.b**) and follows more closely the strong SST signal. This suggests that the increasing potential intensity (**fig. 4.17.a**) is best explained by the large intrinsic variability of PI, which depends on several thermodynamic and dynamic factors beyond SST, as previously mentioned in section **4.2.3**.

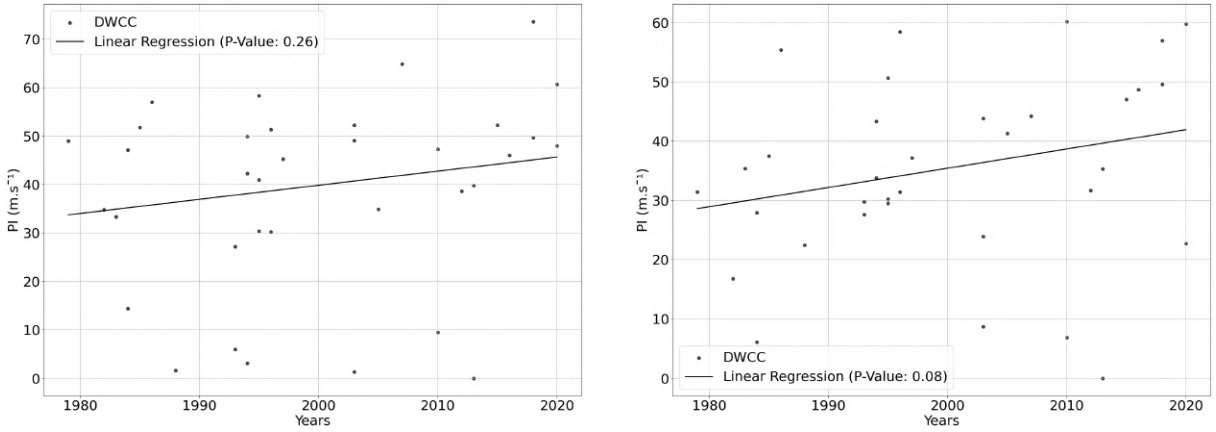

(a) Total PI (b) Climatic PI

Fig. 4.17 Time series of the total (left) and climatic (right) PI average computed in a 4° by 4° box centered on each DWCC, 36h before their minimum SLP.

Finally, no significant long-term trends are found in the wind or precipitation associated with DWCC (**fig. 4.18**). Additional tests using the upper 10% of wind and rainfall values within a 10° × 10° box surrounding each event yield the same result, suggesting that extreme impacts, like the mean values, do not exhibit detectable trends over the 42-year period. This outcome is consistent

with the substantial variability inherent in wind and precipitation fields and may also indicate that these quantities depend on a wider set of environmental controls than PI alone.

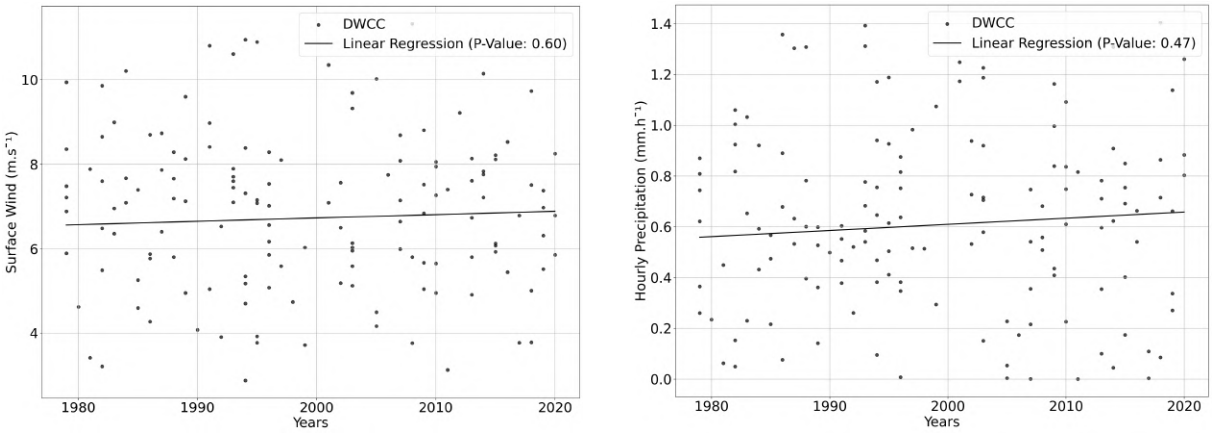

(a) Surface wind

(b) 24h-accumulated precipitation

Fig. 4.18 Time series of the 10m wind (left) and 24h accumulated precipitation (right) average computed in a 4° by 4° box centered on each DWCC, at the time of minimum SLP.

4.4 Discussion

This study provides a comprehensive analysis of Mediterranean Deep Warm Core Cyclones (DWCC) compared to classical Extratropical Cyclones (ETC). Moving beyond the individual case studies and idealized model simulations that characterize much of the existing literature [223, 65, 252, 226], an extensive dataset of real-world cyclones developed by [235] is used.

While previous works focused on anomalous environmental conditions associated with the peak intensity phase of cyclones [230, 223, 291], which can often appear similar for both warm-core and intense cold-core systems, this study instead compares environmental conditions during the intensification phase of DWCC and strong extratropical cyclones (SETC). This distinction makes it possible to isolate the physical mechanisms that favor a tropical-like transition, defined here as the evolution from a cold-core structure to a deep warm-core structure [98].

It is, however, important to note that the classification of cyclones presented in this work is based on Cyclone Phase Space (CPS) diagrams [85]. Although the CPS framework is a widely accepted diagnostic tool, its application to Mediterranean systems remains a subject of debate within the scientific community. The original formulation by [85] requires adaptation for the smaller and shorter-lived Mediterranean systems. In this study, this was done following the works of [239, 230, 224, 241, 226]. It has to be stressed that CPS diagnostics does not differentiate between diabatically driven warm cores and warm seclusions, as highlighted by [234, 87, 231, 229]. Indeed, both medicanes and warm seclusions are present in the DWCC class. The number of warm seclusions may be slightly enhanced by the absence of the symmetry criterion introduced by [85] (as measured by the B parameter) in the present analysis. However,

the tracking algorithm employed by [235] already incorporates symmetry-related constraints: 95% of the selected cyclones indeed satisfy the low B criterion.

In light of these methodological considerations, and considering that the number of DWCC identified in this study, 3.4 cyclones per year, is considerably larger than the number of medicanes typically reported in the literature, which is about 1.5 per year [292, 65, 224, 225], readers may be tempted to conclude that most DWCC are warm seclusions. However, it is worth noting that in several cases reported in the literature, the number of occurrences of tropical-like cyclones has been obtained by explicitly tuning selection criteria used for the definition of medicanes to obtain an average of 1.5 events per year, a number that originated from an informal register that was maintained by the Meteorological group at the University of Balearic Islands (see www.uib.es/depart/dfs/meteorologia/METEOROLOGIA/MEDICANES). By varying a threshold parameter within a reasonable range in the selection procedure, [65] found that the number of events varied by a factor of three. Similar sensitivity was presented in [224]. For these reasons, even acknowledging that the DWCC dataset includes warm seclusions, it is impossible to presently state what fraction of DWCC belongs to the different categories. In any case, it is reasonable to expect that many of the signals emerging from this work that differentiate DWCC from classical strong ETC evolution might be even clearer for tropical-like cyclones. A demonstration of this, however, requires a clear identification of medicanes within the DWCC class and is left for future work.

The present analysis reveals that both DWCC and strong ETC originate from a strong positive upper-level potential vorticity (PV) anomaly, setting them apart from the majority of weak ETC. Those strong PV anomalies are mainly of adiabatic origin, typically associated with PV advection from the stratosphere [273, 274]. While DWCC and SETC exhibit similar surface wind speeds, DWCC are associated with larger and more intense precipitation patterns, as well as stronger enthalpy fluxes at the air-sea interface, resulting, on average, in more dangerous phenomena [225].

The primary distinction between the two cyclone types considered here is reflected in their potential intensity (PI): during the intensification phase, PI is on average higher for DWCC than for SETC. A central contribution of this study is the systematic analysis of PI across a large sample of Mediterranean cyclones, enabling an assessment of its diagnostic relevance in a statistical sense. Although the PI distributions of extratropical-type cyclones and deep warm-core cyclones partially overlap, indicating that PI alone does not provide a strict separation between the two classes, clear differences nevertheless emerge at the population level. This analysis, therefore, goes beyond demonstrating that high-PI environments can occur in the Mediterranean Sea [232, 275], and instead shows that PI provides probabilistic information on cyclone evolution, with higher PI values associated with an increased likelihood of deep warm-core development.

In this PI distinction, seasonality plays an important role: DWCC predominantly form in autumn and spring, whereas SETC develop mainly in winter. Therefore, SETC are typically associated with colder sea surface temperatures (SST) than DWCC, conditions that lead to

lower climatological values of PI. In contrast, DWCC form at locations and times in which climatological PI is larger. Moreover, DWCC develop in situations when the actual PI is larger than the climatological value, confirming that specific localized conditions (such as the mid-level cold intrusions) contribute to setting a favorable context for their intensification [230]. Instead, cold anomaly intrusions in SETC do not significantly modify PI from the climatological value, possibly because of the stronger air column stability associated with the lower SST. Wind shear further distinguishes the two cyclone types: DWCC form in settings with weaker upper-level jets, as suggested in previous studies [230, 223].

The development of a cold anomaly in the mid-troposphere (which is present in all cyclone categories, **sup. fig. B.12**) can be directly driven by the upper-troposphere PV intrusion through several dynamic and thermodynamic processes. A positive PV anomaly induces vertical motion below [293], causing mid-tropospheric air to ascend and cool adiabatically as it expands under decreasing pressure. The upper-level divergence associated with the anomaly reinforces this upward motion and cooling. Combined, these processes can generate a significant mid-tropospheric cold anomaly, destabilizing the air column in warm environments and enhancing convection. Further investigation of the terms in the omega equation, similar to the analysis of Hurricane Ophelia's extratropical transition by [294], is needed to confirm the action of these individual processes.

The focus of the present study is the warm-core transition in a broad sense, which encompasses the tropical transition, but is not limited to it. As stated multiple times, the present dataset also includes warm seclusion events, which are not undergoing a TT toward a tropical–like state. As such, the present results contribute to the TT literature in a more general way, by characterizing the environmental and synoptic conditions associated with warm-core development across a wide population of Mediterranean cyclones, rather than isolating TT cases alone. The present findings are consistent with previous work [227, 96], while extending it through an objective framework that tracks the time evolution of cyclones in the Hart cyclone phase space, together with a statistically robust, reanalysis-based perspective on warm-core transitions in the Mediterranean.

[275] propose to differentiate extratropical cyclones with tropical characteristics that develop in the presence of a transient, localized, and self-induced large value of potential intensity (named *cyclops*) from those that develop in a region where the large PI is a large-scale environmental factor (which are actual tropical cyclones, even if they happen outside the tropics). The composite approach adopted in the present study does not allow for a clear distinction between these two categories. A detailed study of PI and the relative contributions from cold troposphere and warm SST anomalies should therefore be performed on individual cyclones to properly assess the frequency of cyclops within the DWCC population.

This possible extension of the present work also requires the integration of the modified potential intensity introduced in [275] to remove the effects of the cyclone-induced tropospheric warming from the computation of PI, which may artificially limit PI once the warm core has

developed. The results suggest that the temporal changes in tropospheric air temperature might play a relatively small role in the evolution of PI (**fig. 4.13**). This result aligns with the statement by [275] that the contribution of the correction in the modified PI is generally modest. However, further analysis will be needed to confirm this indication.

The decay of tropical-like cyclones can be attributed to landfall, increased stability in the air column, wind shear, and passage of the cyclone over a cold SST. The present analysis suggests that DWCC decay is typically linked to a drop in SST, which drives the decrease of PI over time, resembling the SST feedback mechanism known to affect the evolution of classical tropical cyclones, where surface cooling induced by the storm reduces PI [295, 296, 282]. However, ERA5 SST (obtained using both spatial and temporal smoothing of observed SST) may not be the best available estimate of the actual sea surface temperature fields at the time of DWCC occurrence. The use of purely observational SST datasets could lead to interesting findings in the response of the upper waters to DWCC, in the quantification of cold wakes associated with their passage, and in the investigation of their effect on the subsequent evolution of cyclones.

This study benefits from the large observational dataset assimilated in the ERA5 reanalysis, which represents a substantial improvement over earlier studies based on its coarser predecessor, ERA-40 [223]. Nevertheless, it is important to acknowledge the limitations of using non-assimilated variables in the analysis, as these may affect the interpretation of key cyclone characteristics. ERA5 tends to under-represent specific humidity in the lower and mid-troposphere, particularly in convective environments and over sea, which can bias estimates of thermodynamic disequilibrium and moisture fluxes [297–299]. Biases in atmospheric temperature and humidity can distort the vertical instability structure and affect potential intensity metrics. Moreover, ERA5 systematically underestimates peak wind speeds in intense cyclones due to its relatively coarse resolution and smoothed surface drag parameterization, resulting in weaker near-surface winds than those observed in both tropical and tropical-like systems [300, 291].

These shortcomings and the relatively coarse resolution of the used atmospheric model limit ERA5's ability to fully capture the mesoscale dynamics essential for cyclone development and intensification. This limitation is particularly evident when attempting to depict the most intense features, as those found in the northwest quadrant of DWCC composites for both PI and precipitation, where ERA5's spatial and physical resolution proves insufficient to resolve fine-scale structures. Therefore, future research should integrate high-resolution simulations (following [224, 301, 274]), fine-scale hindcasts of reanalysis data such as the CHAPTER dataset presented in the first two chapters of this thesis (**1** & **2**), and targeted observations (like recommended by [302]) to better resolve the fine-scale thermodynamic and dynamical processes governing Mediterranean tropical-like cyclones.

Within the constraints imposed by ERA5's resolution and its limited representation of mesoscale processes, the reanalysis nonetheless provides a consistent framework for examining long-term variability. Over the 1979–2020 period, no statistically significant increase in the

number of Mediterranean cyclones with a deep warm core is detected. This result contrasts with the robust signal emerging from climate projections, which consistently suggest a future decrease in the frequency of Mediterranean tropical-like cyclones under global warming, accompanied by an increase in their intensity and associated risks [292, 65, 303, 128, 66]. However, an important distinction with most previous studies lies in the focus on the recent historical period rather than on future projections, making the comparison non-trivial. In addition to differences between historical analyses and future projections, the aggregation of physically distinct systems within the DWCC category (tropical-like cyclones, cyclops, and warm seclusions) may further mask trends if these subclasses exhibit divergent long-term evolutions.

Despite the absence of a frequency trend, a significant spatial redistribution is identified, with preferred formation regions shifting within the Mediterranean basin. This result is broadly consistent with earlier modelling work indicating enhanced formation in the Gulf of Lion–Genoa region and south of Sicily [303], although the exact patterns differ, likely reflecting dataset resolution, methodology, and the limited length of the observational record.

No robust trend is found in cyclones' PI over the study period, a result that has not been systematically assessed in previous studies on Mediterranean cyclones. The large inter-annual and decadal variability of PI, which depends on multiple thermodynamic factors beyond sea surface temperature alone, likely masks any long-term signal. This behavior is consistent with findings from the tropical cyclone literature, which highlight the dominant role of natural climate variability in shaping PI in the tropical regions over recent decades. For instance, [304] showed that localized sea surface temperature anomalies associated with natural variability can induce stronger PI responses than the more spatially uniform warming driven by greenhouse gases. Similarly, [305] demonstrated that multi-decadal variability has historically outweighed anthropogenic forcing in PI changes, with recent increases largely attributed to natural cycles, while a clearer greenhouse-gas-driven signal is expected to emerge only later in the 21st century.

Consistent with the absence of significant trends in PI, no clear changes are detected in cyclone-related impacts, such as maximum wind speeds and precipitation. The large spread in these variables, combined with their sensitivity to dynamical and environmental factors beyond thermodynamic intensity alone, hinders the detection of long-term trends. Although previous projection-based studies report an intensification of Mediterranean tropical-like cyclones [292, 65, 303, 128, 66], these increases are generally moderate [65] and strongly model-dependent [128]. Overall, these results underline the well-established difficulty of disentangling climate-change signals from natural variability over a few decades, and particularly for regional-scale phenomena. Such difficulties were already mentioned **Chapter 3**, and highlight the need for longer records and higher-resolution datasets to robustly assess long-term trends.

Chapter 5

Conclusion

5.1 Synthesis of Research Findings

This thesis addressed the mechanisms governing extreme precipitation and organized convective systems in the Euro-Mediterranean region through three interconnected research questions, progressing from dataset validation to the physical interpretation of localized extremes and, finally, to the large-scale dynamics of intense cyclonic systems. Together, the results provide a coherent picture of how thermodynamic and dynamical processes interact across scales to shape high-impact hydro-meteorological phenomena in a changing climate.

Chapter 2 constitutes the methodological cornerstone of this thesis by focusing on the rigorous evaluation of the CHAPTER dataset against independent observational references. Through a comprehensive validation framework, the convection-permitting downscaling of ERA5 was assessed in terms of its ability to reproduce key surface climate variables, including both precipitation and near-surface temperature. The analysis demonstrated that CHAPTER reliably captures the statistical properties, temporal variability, and spatial organization of heavy precipitation, as well as the mean state and variability of temperature, across a range of climatic regions and regimes.

The performance of CHAPTER was systematically benchmarked against existing, well-established high-resolution regional datasets [165, 166]. These comparisons showed that CHAPTER performs at least as well as state-of-the-art alternatives, despite differences in model configurations. This result confirms that the dynamical downscaling approach adopted here does not compromise realism but enables the study of processes at unprecedented spatial resolution for a multi-decade atmospheric dataset. By establishing observational credibility, **Chapter 2** validates CHAPTER as a trustworthy representation of convective precipitation and associated atmospheric processes.

Building on this validated framework, **Chapter 3** focused on disentangling the physical drivers of trends in localized precipitation extremes in the Mediterranean and European regions. The analysis revealed different spatial patterns. An increase in extreme hourly rainfall was observed in most of the Mediterranean and the North Sea, but at the same time, the West of France, the Iberian Peninsula, and the border between Eastern Europe and Russia experienced negative trends. Crucially, the applied diagnostic decomposition showed that this increase cannot be explained by thermodynamic effects alone. The thermodynamic contribution, linked to the enhanced moisture-holding capacity of a warmer atmosphere, exhibits a generally positive but modest trend. On the other hand, it is the dynamical component, associated with changes in vertical motion and convective intensity, that dominates both the magnitude and the spatial structure of extreme precipitation changes.

Chapter 3 further highlighted the importance of surface–atmosphere interactions as regional contrasts suggest a feedback involving soil moisture, evaporation, and convective strength. In regions such as Greece and southern Italy, abundant marine moisture supply from the surrounding areas coincides with the increase of convective instability and supports positive trends in both mean autumn precipitation and extreme hourly rainfall. In contrast, the Iberian Peninsula and western France experience pronounced soil drying, which limits evaporation and appears to suppress an already limited convective activity and extreme hourly precipitation.

Finally, **Chapter 4** extended the analysis to organized convective systems embedded in large-scale circulation patterns, focusing on Mediterranean cyclones. By directly comparing deep warm core cyclones (DWCC) with strong extratropical cyclones (SETC) during their intensification phases, this chapter clarified the conditions favoringthe development of a deep warm core. Both cyclone types originate from strong upper-level positive potential vorticity anomalies of adiabatic origin, typically associated with jet stream meandering, distinguishing them from weaker extratropical cyclones. Despite comparable surface wind speeds, DWCC are characterized by stronger air–sea enthalpy fluxes and more extensive and intense precipitation.

The key discriminator between DWCC and SETC lies in their potential intensity (PI). DWCC develop in environments with systematically higher PI, a distinction strongly modulated by seasonality. Their preferential formation in autumn and spring corresponds to warmer sea surface temperatures and higher climatological PI, whereas SETC predominantly form in winter under colder SST and lower PI. Moreover, DWCC tend to intensify when actual PI exceeds its climatological value, indicating the importance of localized conditions, such as mid-level cold intrusions, in creating a favorable thermodynamic environment. In contrast, similar cold intrusions in SETC do not significantly enhance PI, likely due to the greater static stability imposed by colder SST. Differences in vertical wind shear further separate the two cyclone types, with DWCC forming in environments characterized by weaker upper-level jets.

5.2 Scientific Contributions and Limitations

The synthesis of findings presented in the previous section provides a coherent overview of the physical mechanisms governing localized convective precipitation and deep warm-core cyclones in the Euro-Mediterranean region. However, a full contextualization of this research requires moving beyond the results to evaluate their broader impact on the field and the inherent constraints of the study. To provide this perspective, the following section details the specific scientific contributions of each chapter. This section highlights the advancements in process-based understanding, while critically addressing the methodological and data-driven limitations that define the scope of these findings.

Chapter 2 provides a rigorous validation that establishes CHAPTER as a reliable convection-permitting climate dataset suitable for broad scientific use. By demonstrating performance comparable to established high-resolution reference products, this chapter enables confident application of CHAPTER for process-based analyses, extreme event studies, and investigations of climate variability. Its particular strength lies in the combination of high spatial resolution over an extended domain covering the whole Mediterranean basin and all of central Europe, an extended temporal coverage of 42 years, and the availability of three-dimensional atmospheric variables. Together, these characteristics currently make CHAPTER unique in spatial and temporal extent among existing European high-resolution products [147–153, 155]. This validation, therefore, serves as a critical enabling step for the subsequent chapter of this thesis and future studies seeking a consistent, long-term, high-resolution framework.

A key limitation of this work concerns the temporal scale of the validation. The focus on daily statistics, while appropriate for assessing climatological behavior and large-scale variability, does not fully capture the short-lived, high-intensity precipitation events characteristic of deep convection. A validation at hourly timescales would provide a more direct evaluation of extreme rainfall dynamics, but such an extension is currently constrained by the limited availability of long, high-quality sub-daily observational records at a pan-european spatial extent, and by the substantial computational cost associated with high-frequency analyses.

Chapter 3 advances the scientific understanding of precipitation extremes by disentangling the respective roles of the atmospheric thermodynamics and the dynamics component in extreme precipitation trends. The results highlight that changes in convective organization and vertical motion are key drivers of extreme precipitation, challenging interpretations based mainly on thermodynamic scaling [206]. In addition, the analysis demonstrates that surface water availability exerts a strong control on convective intensity, indicating that surface–atmosphere coupling is a crucial component in shaping present-day extremes. Together, these findings stress that future changes in precipitation extremes cannot be inferred from thermodynamic assumptions alone, but will depend on the joint evolution of dynamical circulation patterns and sea-land-surface processes.

However, this chapter remains limited in scope by its focus on present-day conditions. The absence of explicit future climate scenarios prevents a direct assessment of how the identified mechanisms may evolve under a stronger global warming signal. Moreover, a more comprehensive characterization of air–sea and air–land interactions, with the computation of additional dynamical and thermodynamical indices, or possibly with coupled sea-atmosphere long-term modelling experiments, would be necessary to further isolate and quantify the processes underlying the observed signals.

Beyond the validation presented in **Chapter 2** and the specific analyses performed in **Chapter 3**, a more fundamental limitation is inherent to the CHAPTER dataset itself, and thus to any study based on it. CHAPTER represents a single realization of a regional climate model with a fixed configuration and set of physical parameterizations. The absence of an ensemble of convection-permitting simulations for a domain of this size and over a multi-decadal period implies that internal climate variability and model uncertainty cannot be explicitly sampled. Producing such an ensemble would be computationally extremely demanding, financially costly, and associated with a substantial carbon footprint, rendering this approach currently unfeasible. However, for more spatially limited regions, complementary high-resolution datasets, derived from physical or statistical downscaling, including emerging AI-based approaches with rapidly increasing capabilities, can be used to partially address this limitation. In this context, CHAPTER should be viewed as a foundational dataset that can be combined with other products to strengthen robustness, or used on its own to provide strong circumstantial evidence of climate change–driven signals, particularly at the scale of convective processes.

Chapter 4 contributes to the understanding of Mediterranean cyclones by focusing on the early stages of systems that eventually develop warm-core characteristics. In contrast to studies that consider only warm-core cyclones, such as [230], this chapter compares cyclones that undergo a warm-core transition with those that retain a classical cold-core structure. Moreover, the comparison is performed at an early stage of the cyclone lifecycle, when both types of systems remain dynamically similar and are still characterized by a baroclinic structure. This approach differs from that of [223], who compared cyclones at a later stage when warm-core systems had already reached their mature phase. By focusing on the period preceding the transition and by contrasting the two cyclone types while they are still dynamically comparable, this chapter aims to identify factors that favor the development of a warm core, rather than characteristics that arise as a consequence of the transition.

The interpretation of these results is nonetheless subject to two main limitations. The warm-core cyclones dataset includes a heterogeneous mix of cyclone types, such as tropical-like cyclones, CYCLOP systems, and warm seclusions, which differ in their underlying dynamics. This diversity may dampen or blur the signals in key variables such as potential intensity, sea-surface temperature, potential vorticity anomalies, wind shear, and their trends. Additionally, the reliance on ERA5 reanalysis, while advantageous for its coverage and consistency, limits the ability to resolve small-scale, convection-driven processes that are central to cyclone evolution.

5.3 Future Research Direction

The limitations outlined in the previous section point toward several promising avenues for future investigation. While the present work has established a rigorous methodological framework and identified key physical mechanisms governing extreme precipitation and deep warm-core cyclones in the Euro-Mediterranean region, the constraints inherent to present-day analysis and the heterogeneity of cyclone classifications naturally motivate extensions that can deepen our mechanistic understanding and improve predictive capabilities.

A logical next step is to apply the diagnostic scaling framework developed in **Chapter 3** to convection-permitting model simulations that incorporate future climate scenarios. While the high computational cost and carbon footprint of such models often preclude basin-wide long-term simulations, the results of this thesis provide a strategic advantage: high-sensitivity "hotspots" have already been identified: southern Italy, Greece, the Iberian Peninsula, and France. Future efforts could focus on these sub-domains to assess how the balance between thermodynamic and dynamical contributions shifts under a stronger global warming signal.

To move beyond the diagnostic signals of soil moisture–precipitation coupling, a more comprehensive characterization of the convective environment is required. In principle, a definitive attribution of the feedback mechanisms discussed could be achieved through targeted numerical sensitivity experiments, such as artificially decoupling surface evaporative fluxes from soil moisture availability. While such experiments would provide an unambiguous test of the proposed feedback, conducting them at the spatial scale and resolution of the CHAPTER simulations would involve a prohibitive computational cost and carbon footprint, unjustified by the marginal scientific gains. As discussed above, these approaches would only be feasible over limited sub-domains. Consequently, future research should focus on strengthening the statistical evidence by integrating additional thermodynamic and dynamical indicators to better constrain the pre-convective environment. This more scalable approach would enhance the robustness of the relationships identified in **Chapter 3** and reinforce the physical interpretation of land–atmosphere coupling without relying on resource-intensive sensitivity experiments.

The results of **Chapter 4** highlight the environmental factors favoring DWCC intensification, yet the inherent diversity within this category remains an open challenge. Future research should repeat this analysis for specific sub-categories, namely Tropical-Like Cyclones (TLC/Medicanes), CYCLOPS systems, and warm seclusions. The present work supports the hypothesis that these systems can be more clearly differentiated using the environmental potential intensity to which they are associated. This investigation could benefit from transitioning from the use of ERA5 reanalysis to CHAPTER data. Using convection-permitting resolutions will provide the necessary precision to resolve the fine-scale thermodynamic and dynamical processes, such as inner-core convection and air-sea enthalpy exchange, that govern the evolution of Mediterranean tropical-like systems but are often smoothed out in coarser products.

Finally, a key operational question remains: can potential intensity serve as a reliable early indicator for DWCC formation and intensification? Future work should focus on identifying a potential intensity threshold in the early stages of cyclogenesis that distinguishes future warm-core systems from standard extratropical cyclones. By tracking the lifecycle of systems that exceed these thresholds, it could be possible to evaluate the skill of potential intensity as a forecasting tool. Such an approach holds significant promise for improving early warning systems and risk mitigation strategies in the vulnerable coastal regions of the Mediterranean.

References

[1] Agency European, Environment. Europe's state of water 2024: the need for improved water resilience. *EEA Report*, 2024.

[2] Frank Roux. Tropical cyclones: development and organization, encyclopedia of the environment. *Encyclopedia of the Environment*, 2025.

[3] Brian A Colle, James F Booth, and Edmund KM Chang. A review of historical and future changes of extratropical cyclones and associated impacts along the us east coast. *Current Climate Change Reports*, 1(3):125–143, 2015.

[4] Edgar Dolores Tesillos. *Changes in Extratropical Cyclone Dynamics in the North Atlantic in a Warming Climate*. Freie Universitaet Berlin (Germany), 2022.

[5] Mateusz Taszarek, John Allen, Tomáš Púčik, Pieter Groenemeijer, Bartosz Czernecki, Leszek Kolendowicz, Kostas Lagouvardos, Vasiliki Kotroni, and Wolfgang Schulz. A climatology of thunderstorms across europe from a synthesis of multiple data sources. *Journal of Climate*, 32(6):1813–1837, 2019.

[6] Kerry Emanuel. Tropical cyclone activity downscaled from noaa-cires reanalysis, 1908–1958. *Journal of Advances in Modeling Earth Systems*, 2(1), 2010.

[7] Laura A Bakkensen. Mediterranean hurricanes and associated damage estimates. *Journal of Extreme Events*, 4(02):1750008, 2017.

[8] Veronika Weilnhammer, Jonas Schmid, Isabella Mittermeier, Fabian Schreiber, Linmiao Jiang, Vedran Pastuhovic, Caroline Herr, and Stefanie Heinze. Extreme weather events in europe and their health consequences–a systematic review. *International Journal of Hygiene and Environmental Health*, 233:113688, 2021.

[9] Marian Mierla, Gheorghe Romanescu, Iulian Nichersu, and Ion Grigoras. Hydrological risk map for the danube delta—a case study of floods within the fluvial delta. *IEEE Journal of Selected Topics in Applied Earth Observations and Remote Sensing*, 8(1):98–104, 2014.

[10] Umberto Simeoni and Corinne Corbau. A review of the delta po evolution (italy) related to climatic changes and human impacts. *Geomorphology*, 107(1-2):64–71, 2009.

[11] Fekri A Hassan. Historical nile floods and their implications for climatic change. *Science*, 212(4499):1142–1145, 1981.

[12] Aurélie Maspataud, Marie-Hélène Ruz, and Stéphane Vanhée. Potential impacts of extreme storm surges on a low-lying densely populated coastline: the case of dunkirk area, northern france. *Natural hazards*, 66(3):1327–1343, 2013.

[13] Michalis I Vousdoukas, Evangelos Voukouvalas, Alessandro Annunziato, Alessio Giardino, and Luc Feyen. Projections of extreme storm surge levels along europe. *Climate Dynamics*, 47(9):3171–3190, 2016.

[14] Rut Romero-Martín, Marc Sanuy, and José A Jiménez. Unveiling the role of storm surges as a driver of flooding on the western mediterranean: a case study of the ebro delta. *Natural hazards*, 121(4):4961–4984, 2025.

[15] Munich Re. Winter storms in europe (ii): Analysis of 1999 losses and loss potentials. *Munich Re Group Rep*, 302(03109):72, 2002.

[16] Swiss Re. Storm over europe—an underestimated risk., 2000.

[17] Emmanouil Flaounas, Silvio Davolio, Shira Raveh-Rubin, Florian Pantillon, Mario Marcello Miglietta, Miguel Angel Gaertner, Maria Hatzaki, Victor Homar, Samira Khodayar, Gerasimos Korres, et al. Mediterranean cyclones: Current knowledge and open questions on dynamics, prediction, climatology and impacts. *Weather and Climate Dynamics*, 3(1):173–208, 2022.

[18] Wojciech Pilorz, Igor Laskowski, Artur Surowiecki, and Ewa Łupikasza. Fatalities related to sudden meteorological events across central europe from 2010 to 2020. *International Journal of Disaster Risk Reduction*, 88:103622, 2023.

[19] Lea Houtsonen and Arvo Peltonen. Natural disasters in europe. In *International Perspectives on Natural Disasters: Occurrence, Mitigation, and Consequences*, pages 263–280. Springer, 2004.

[20] R Sari Kovats and L Ebi Kristie. Heatwaves and public health in europe. *The European Journal of Public Health*, 16(6):592–599, 2006.

[21] Martin Hoerling, Jon Eischeid, Judith Perlwitz, Xiaowei Quan, Tao Zhang, and Philip Pegion. On the increased frequency of mediterranean drought. *Journal of climate*, 25(6):2146–2161, 2012.

[22] Joachim Hill, Jacques Megier, and Wolfgang Mehl. Land degradation, soil erosion and desertification monitoring in mediterranean ecosystems. *Remote sensing reviews*, 12(1-2):107–130, 1995.

[23] Juli G Pausas, Joan Llovet, Anselm Rodrigo, and Ramon Vallejo. Are wildfires a disaster in the mediterranean basin?–a review. *International Journal of wildland fire*, 17(6):713–723, 2008.

[24] Luca Montanarella. Trends in land degradation in europe. In *Climate and land degradation*, pages 83–104. Springer, 2007.

[25] S Bajocco, A De Angelis, L Perini, A Ferrara, and L Salvati. The impact of land use/land cover changes on land degradation dynamics: a mediterranean case study. *Environmental management*, 49(5):980–989, 2012.

[26] Riccardo Bonanno, Matteo Lacavalla, and Simone Sperati. A new high-resolution meteorological reanalysis italian dataset: Merida. *Quarterly Journal of the Royal Meteorological Society*, 145(721):1756–1779, 2019.

[27] Ashraf M Dewan. Hazards, risk, and vulnerability. In *Floods in a megacity: Geospatial techniques in assessing hazards, risk and vulnerability*, pages 35–74. Springer, 2013.

[28] Philipp Schmidt-Thomé. *Natural and technological hazards and risks affecting the spatial development of European regions*, volume 42. Geological survey of Finland, 2006.

[29] Brian Azzopardi, Mario V Balzan, Semia Cherif, Enrique Doblas-Miranda, Maria dos Santos, Philippe Dobrinski, Marianela Falder, Abed El Rahman Hassoun, Carlo Giupponi, Vally Vassiliki Koubi, et al. *Climate and environmental change in the Mediterranean basin–current situation and risks for the future. First Mediterranean assessment report*. MedECC, 2020.

[30] UNCTAD. *Review of maritime transport 2022*. UN, 2022.

[31] Department of Economic. *World Population Prospects 2024: Summary of Results*. Stylus Publishing, LLC, 2024.

[32] Philipp Schmidt-Thomé, Stefan Greiving, Hilkka Kallio, Mark Fleischhauer, and Jaana Jarva. Economic risk maps of floods and earthquakes for european regions. *Quaternary International*, 150(1):103–112, 2006.

[33] Brenden Jongman, Stefan Hochrainer-Stigler, Luc Feyen, Jeroen CJH Aerts, Reinhard Mechler, WJ Wouter Botzen, Laurens M Bouwer, Georg Pflug, Rodrigo Rojas, and Philip J Ward. Increasing stress on disaster-risk finance due to large floods. *Nature Climate Change*, 4(4):264–268, 2014.

[34] Laurent Schmitt, Dale Morris, G Mathias Kondolf, Laurent Schmitt, G Mathias Kondolf, Laurent Schmitt, and Dale Morris. Managing floods in large river basins in europe: the rhine river. In *Managing Flood Risk: Innovative Approaches from Big Floodplain Rivers and Urban Streams*, pages 75–89. Springer, 2018.

[35] Sandra Graus, Tiago Miguel Ferreira, Graça Vasconcelos, and Javier Ortega. Changing conditions: Global warming-related hazards and vulnerable rural populations in mediterranean europe. *Urban Science*, 8(2):42, 2024.

[36] Mohammad Ilbeigi and Sarath Chandra K Jagupilla. An empirical analysis of association between socioeconomic factors and communities' exposure to natural hazards. *Sustainability*, 12(16):6342, 2020.

[37] Yang Zhou, Ning Li, Wenxiang Wu, Jidong Wu, and Peijun Shi. Local spatial and temporal factors influencing population and societal vulnerability to natural disasters. *Risk analysis*, 34(4):614–639, 2014.

[38] Daniel Navarro, Carolina Cantergiani, Beñat Abajo, Izaskun Gomez de Salazar, and Efrén Feliu. Territorial vulnerability to natural hazards in europe: a composite indicator analysis and relation to economic impacts. *Natural Hazards*, pages 1–25, 2023.

[39] Christoph Clar. How demographic developments determine the management of hydrometeorological hazard risks in rural communities: The linkages between demographic and natural hazards research. *Wiley Interdisciplinary Reviews: Water*, 6(6):e1378, 2019.

[40] Alexandra Kovacs, Horaţiu Ştefănie, Camelia Botezan, Iulia Crăciun, and Alexandru Ozunu. Assesment of natural hazards in european countries with impact on young people. *International Multidisciplinary Scientific GeoConference: SGEM*, 17:73–80, 2017.

[41] Christian Henrik Alexander Kuran, Claudia Morsut, Bjørn Ivar Kruke, Marco Krüger, Lisa Segnestam, Kati Orru, Tor Olav Nævestad, Merja Airola, Jaana Keränen, Friedrich Gabel, et al. Vulnerability and vulnerable groups from an intersectionality perspective. *International Journal of Disaster Risk Reduction*, 50:101826, 2020.

[42] Jaime de Diego, Antonio Rúa, and Mercedes Fernández. Vulnerability variables and their effect on wildfires in galicia (spain). a panel data analysis. *Land*, 10(10):1004, 2021.

[43] Ilias Petrou, Pavlos Kassomenos, and Nikolaos Kyriazis. Assessing future heatwave-related mortality in greece using advanced machine learning and climate projections. *Atmosphere*, 16(9):1093, 2025.

[44] Ignazio Mongelli, URIBE Antonio AVILA, Joachim Maes, LAGUNA Jorge DURAN, Luc Feyen, MARTINEZ Juan Carlos CISCAR, et al. Regional economic climate risks in europe. *Publications Office of the European Union*, 2025.

[45] Alessia Trovato, Anthony Reid, Kudakwashe C Takarinda, Chiara Montaldo, Tom Decroo, Philip Owiti, Francesco Bongiorno, and Stefano Di Carlo. Dangerous crossing: demographic and clinical features of rescued sea migrants seen in 2014 at an outpatient clinic at augusta harbor, italy. *Conflict and Health*, 10(1):14, 2016.

[46] United Nations Human Rights Council. Mediterranean sea journeys for migrants have grown more deadly: Unhcr, 2022. Available at: https://news.un.org/en/story/2022/06/1120132 (Accessed: 21 July 2023).

[47] Noah S Diffenbaugh, Deepti Singh, Justin S Mankin, Daniel E Horton, Daniel L Swain, Danielle Touma, Allison Charland, Yunjie Liu, Matz Haugen, Michael Tsiang, et al. Quantifying the influence of global warming on unprecedented extreme climate events. *Proceedings of the National Academy of Sciences*, 114(19):4881–4886, 2017.

[48] Jean Calleja-Agius, Kathleen England, and Neville Calleja. The effect of global warming on mortality. *Early Human Development*, 155:105222, 2021.

[49] Wolfgang Cramer, Joël Guiot, Marianela Fader, Joaquim Garrabou, Jean-Pierre Gattuso, Ana Iglesias, Manfred A Lange, Piero Lionello, Maria Carmen Llasat, Shlomit Paz, et al. Climate change and interconnected risks to sustainable development in the mediterranean. *Nature Climate Change*, 8(11):972–980, 2018.

[50] Filippo Giorgi and Piero Lionello. Climate change projections for the mediterranean region. *Global and planetary change*, 63(2-3):90–104, 2008.

[51] J.G. Canadell, P.M.S. Monteiro, M.H. Costa, L. Cotrim da Cunha, P.M. Cox, A.V. Eliseev, S. Henson, M. Ishii, S. Jaccard, C. Koven, A. Lohila, P.K. Patra, S. Piao, J. Rogelj, S. Syampungani, S. Zaehle, and K. Zickfeld. *Global Carbon and other Biogeochemical Cycles and Feedbacks*, book section 12, page 673–816. Cambridge University Press, Cambridge, United Kingdom and New York, NY, USA, 2021.

[52] Christos Giannakopoulos, Philippe Le Sager, Marco Bindi, Marco Moriondo, Effie Kostopoulou, and CM Goodess. Climatic changes and associated impacts in the mediterranean resulting from a 2 c global warming. *Global and Planetary Change*, 68(3):209–224, 2009.

[53] Christoph Schär, Pier Luigi Vidale, Daniel Lüthi, Christoph Frei, Christian Häberli, Mark A Liniger, and Christof Appenzeller. The role of increasing temperature variability in european summer heatwaves. *Nature*, 427(6972):332–336, 2004.

[54] Stefan Rahmstorf and Dim Coumou. Increase of extreme events in a warming world. *Proceedings of the National Academy of Sciences*, 108(44):17905–17909, 2011.

[55] Manolis G Grillakis. Increase in severe and extreme soil moisture droughts for europe under climate change. *Science of The Total Environment*, 660:1245–1255, 2019.

[56] Marco Moriondo, P Good, R Durao, M Bindi, C Giannakopoulos, and J Corte-Real. Potential impact of climate change on fire risk in the mediterranean area. *Climate research*, 31(1):85–95, 2006.

[57] Parisa Hosseinzadehtalaei, Hossein Tabari, and Patrick Willems. Climate change impact on short-duration extreme precipitation and intensity–duration–frequency curves over europe. *Journal of Hydrology*, 590:125249, 2020.

[58] Robert Vautard, Andreas Gobiet, Stefan Sobolowski, Erik Kjellström, Annemiek Stegehuis, Paul Watkiss, Thomas Mendlik, Oskar Landgren, Grigory Nikulin, Claas Teichmann, et al. The european climate under a 2 c global warming. *Environmental Research Letters*, 9(3):034006, 2014.

[59] George Zittis, Adriana Bruggeman, and Jos Lelieveld. Revisiting future extreme precipitation trends in the mediterranean. *Weather and Climate Extremes*, 34:100380, 2021.

[60] Lorenzo Alfieri, P Burek, Luc Feyen, and Giovanni Forzieri. Global warming increases the frequency of river floods in europe. *Hydrology and Earth System Sciences*, 19(5):2247–2260, 2015.

[61] Alistair Hendry, Ivan D Haigh, Robert J Nicholls, Hugo Winter, Robert Neal, Thomas Wahl, Amélie Joly-Laugel, and Stephen E Darby. Assessing the characteristics and drivers of compound flooding events around the uk coast. *Hydrology and Earth System Sciences*, 23(7):3117–3139, 2019.

[62] Martin Beniston, Daniel Farinotti, Markus Stoffel, Liss M Andreassen, Erika Coppola, Nicolas Eckert, Adriano Fantini, Florie Giacona, Christian Hauck, Matthias Huss, et al. The european mountain cryosphere: a review of its current state, trends, and future challenges. *The Cryosphere*, 12(2):759–794, 2018.

[63] Wilfried Haeberli and Martin Beniston. Climate change and its impacts on glaciers and permafrost in the alps. *Ambio*, pages 258–265, 1998.

[64] Giacomo Strapazzon, Jürg Schweizer, Igor Chiambretti, Monika Brodmann Maeder, Hermann Brugger, and Ken Zafren. Effects of climate change on avalanche accidents and survival. *Frontiers in physiology*, 12:639433, 2021.

[65] Leone Cavicchia, Hans von Storch, and Silvio Gualdi. Mediterranean tropical-like cyclones in present and future climate. *Journal of Climate*, 27(19):7493–7501, 2014.

[66] Juan J González-Alemán, Salvatore Pascale, Jesús Gutierrez-Fernandez, Hiroyuki Murakami, Miguel A Gaertner, and Gabriel A Vecchi. Potential increase in hazard from mediterranean hurricane activity with global warming. *Geophysical Research Letters*, 46(3):1754–1764, 2019.

[67] RJ Nicholls and FMJ Hoozemans. The mediterranean: vulnerability to coastal implications of climate change. *Ocean & Coastal Management*, 31(2-3):105–132, 1996.

[68] Roderik SW van de Wal, Angélique Melet, Debora Bellafiore, Michalis Vousdoukas, Paula Camus, Christian Ferrarin, Gualbert Oude Essink, Ivan D Haigh, Piero Lionello, Arjen Luijendijk, et al. Sea level rise in europe: Impacts and consequences. *State of the Planet Discussions*, 2023:1–65, 2023.

[69] Michalis I Vousdoukas, Lorenzo Mentaschi, Evangelos Voukouvalas, Martin Verlaan, and Luc Feyen. Extreme sea levels on the rise along europe's coasts. *Earth's Future*, 5(3):304–323, 2017.

[70] Marco Bohnhoff, Patricia Martínez-Garzón, and Yehuda Ben-Zion. Global warming will increase earthquake hazards through rising sea levels and cascading effects, 2024.

[71] Jamie I Farquharson and Falk Amelung. Volcanic hazard exacerbated by future global warming-driven increase in heavy rainfall. *Royal Society Open Science*, 9(7):220275, 2022.

[72] Septimius Mara and Serban-Nicolae Vlad. Global climatic changes, a possible cause of the recent increasing trend of earthquakes since the 90's and subsequent lessons learnt. In *Earthquake research and analysis-new advances in seismology*. IntechOpen, 2013.

[73] B McGuire. Potential for a hazardous geospheric response to projected future climate changes. *Philosophical Transactions of the Royal Society A: Mathematical, Physical and Engineering Sciences*, 368(1919):2317–2345, 2010.

[74] Kerry Emanuel, Christopher DesAutels, Christopher Holloway, and Robert Korty. Environmental control of tropical cyclone intensity. *Journal of the atmospheric sciences*, 61(7):843–858, 2004.

[75] Jialin Lin, Taotao Qian, Peter Bechtold, Georg Grell, Guang J Zhang, Ping Zhu, Saulo R Freitas, Hannah Barnes, and Jongil Han. Atmospheric convection. *Atmosphere-Ocean*, 60(3-4):422–476, 2022.

[76] Kerry Emanuel. Tropical cyclones. *Annual review of earth and planetary sciences*, 31(1):75–104, 2003.

[77] Michio Yanai. Formation of tropical cyclones. *Reviews of Geophysics*, 2(2):367–414, 1964.

[78] Da-Lin Zhang and Lin Zhu. Roles of upper-level processes in tropical cyclogenesis. *Geophysical research letters*, 39(17), 2012.

[79] Kerry A Emanuel. An air-sea interaction theory for tropical cyclones. part i: Steady-state maintenance. *Journal of Atmospheric Sciences*, 43(6):585–605, 1986.

[80] John Molinari, Kelly Lombardo, and David Vollaro. Tropical cyclogenesis within an equatorial rossby wave packet. *Journal of the atmospheric sciences*, 64(4):1301–1317, 2007.

[81] Brian J Hoskins. Theory of extratropical cyclones. In *Extratropical Cyclones: The Erik Palmén Memorial Volume*, pages 63–80. Springer, 1990.

[82] Sverre Petterssen and SJ Smebye. On the development of extratropical cyclones. *Quarterly Journal of the Royal Meteorological Society*, 97(414):457–482, 1971.

[83] Melvyn A Shapiro and Daniel Keyser. Fronts, jet streams and the tropopause. In *Extratropical cyclones: the Erik Palmén memorial volume*, pages 167–191. Springer, 1990.

[84] JL Catto. Extratropical cyclone classification and its use in climate studies. *Reviews of Geophysics*, 54(2):486–520, 2016.

[85] Robert E Hart. A cyclone phase space derived from thermal wind and thermal asymmetry. *Monthly weather review*, 131(4):585–616, 2003.

[86] HA Flocas. Diagnostics of cyclogenesis over the aegean sea using potential vorticity inversion. *Meteorology and Atmospheric Physics*, 73(1-2):25–33, 2000.

[87] L Fita, R Romero, A Luque, K Emanuel, and C Ramis. Analysis of the environments of seven mediterranean tropical-like storms using an axisymmetric, nonhydrostatic, cloud resolving model. *Natural Hazards and Earth System Sciences*, 7(1):41–56, 2007.

[88] Emmanouil Flaounas, Shira Raveh-Rubin, Heini Wernli, Philippe Drobinski, and Sophie Bastin. The dynamical structure of intense mediterranean cyclones. *Climate Dynamics*, 44:2411–2427, 2015.

[89] A Buzzi, M D'isidoro, and S Davolio. A case-study of an orographic cyclone south of the alps during the map sop. *Quarterly Journal of the Royal Meteorological Society: A journal of the atmospheric sciences, applied meteorology and physical oceanography*, 129(591):1795–1818, 2003.

[90] Joan Campins, Ana Genovés, MA Picornell, and A Jansà. Climatology of mediterranean cyclones using the era-40 dataset. *International Journal of Climatology*, 31(11):1596–1614, 2011.

[91] Ron McTaggart-Cowan, Thomas J Galarneau, Lance F Bosart, and Jason A Milbrandt. Development and tropical transition of an alpine lee cyclone. part ii: Orographic influence on the development pathway. *Monthly weather review*, 138(6):2308–2326, 2010.

[92] M Tous, R Romero, and C Ramis. Surface heat fluxes influence on medicane trajectories and intensification. *Atmospheric research*, 123:400–411, 2013.

[93] Naveed Akhtar, Jennifer Brauch, Andreas Dobler, Karine Béranger, and Bodo Ahrens. Medicanes in an ocean–atmosphere coupled regional climate model. *Natural Hazards and Earth System Sciences*, 14(8):2189–2201, 2014.

[94] Ron McTaggart-Cowan, Thomas J Galarneau, Lance F Bosart, and Jason A Milbrandt. Development and tropical transition of an alpine lee cyclone. part i: Case analysis and evaluation of numerical guidance. *Monthly weather review*, 138(6):2281–2307, 2010.

[95] Shira Raveh-Rubin and Emmanouil Flaounas. A dynamical link between deep atlantic extratropical cyclones and intense mediterranean cyclones. *Atmospheric Science Letters*, 18(5):215–221, 2017.

[96] Emmanouil Flaounas, Suzanne L Gray, and Franziska Teubler. A process-based anatomy of mediterranean cyclones: from baroclinic lows to tropical-like systems. *Weather and Climate Dynamics*, 2(1):255–279, 2021.

[97] Christopher A Davis and Lance F Bosart. Baroclinically induced tropical cyclogenesis. *Monthly Weather Review*, 131(11):2730–2747, 2003.

[98] Christopher A Davis and Lance F Bosart. The tt problem: Forecasting the tropical transition of cyclones. *Bulletin of the American Meteorological Society*, 85(11):1657–1662, 2004.

[99] Ron McTaggart-Cowan, Glenn D Deane, Lance F Bosart, Christopher A Davis, and Thomas J Galarneau Jr. Climatology of tropical cyclogenesis in the north atlantic (1948–2004). *Monthly Weather Review*, 136(4):1284–1304, 2008.

[100] Ron McTaggart-Cowan, Thomas J Galarneau Jr, Lance F Bosart, Richard W Moore, and Olivia Martius. A global climatology of baroclinically influenced tropical cyclogenesis. *Monthly Weather Review*, 141(6):1963–1989, 2013.

[101] Piero Lionello, Jonas Bhend, A Buzzi, PM Della-Marta, SO Krichak, A Jansa, P Maheras, Antonella Sanna, IF Trigo, and R Trigo. Cyclones in the mediterranean region: climatology and effects on the environment. In *Developments in earth and environmental sciences*, volume 4, pages 325–372. Elsevier, 2006.

[102] Stephan Pfahl and Heini Wernli. Quantifying the relevance of cyclones for precipitation extremes. *Journal of Climate*, 25(19):6770–6780, 2012.

[103] Guy Delrieu, John Nicol, Eddy Yates, Pierre-Emmanuel Kirstetter, Jean-Dominique Creutin, Sandrine Anquetin, Charles Obled, Georges-Marie Saulnier, Véronique Ducrocq, Eric Gaume, et al. The catastrophic flash-flood event of 8–9 september 2002 in the gard region, france: a first case study for the cévennes–vivarais mediterranean hydrometeorological observatory. *Journal of hydrometeorology*, 6(1):34–52, 2005.

[104] David R Archer, Francois Leesch, and Kirsty Harwood. Learning from the extreme river tyne flood in january 2005. *Water and Environment Journal*, 21(2):133–141, 2007.

[105] Marco Borga, Paolo Boscolo, Francesco Zanon, and Marco Sangati. Hydrometeorological analysis of the 29 august 2003 flash flood in the eastern italian alps. *Journal of hydrometeorology*, 8(5):1049–1067, 2007.

[106] Cameron Do and Yuriy Kuleshov. Multi-hazard tropical cyclone risk assessment for australia. *Remote Sensing*, 15(3):795, 2023.

[107] Dori Nissenbaum, Ron Sarafian, Yinon Rudich, and Shira Raveh-Rubin. Six types of dust events in eastern mediterranean identified using unsupervised machine-learning classification. *Atmospheric Environment*, page 119902, 2023.

[108] Zhiwei Zhang and Xiao-Ming Li. Global ship accidents and ocean swell-related sea states. *Natural Hazards and Earth System Sciences*, 17(11):2041–2051, 2017.

[109] Charles A. Doswell. Severe convective storms in the european societal context. *Atmospheric Research*, 158–159:210–215, May 2015.

[110] PT Nastos, K Karavana Papadimou, and IT Matsangouras. Mediterranean tropical-like cyclones: Impacts and composite daily means and anomalies of synoptic patterns. *Atmospheric Research*, 208:156–166, 2018.

[111] Myles R Allen and William J Ingram. Constraints on future changes in climate and the hydrologic cycle. *Nature*, 419(6903):224–232, 2002.

[112] Caroline J. Muller, Paul A. O'Gorman, and Larissa E. Back. Intensification of precipitation extremes with warming in a cloud-resolving model. *Journal of Climate*, 24(11):2784–2800, June 2011.

[113] Martin S Singh and Paul A O'Gorman. Influence of entrainment on the thermal stratification in simulations of radiative-convective equilibrium. *Geophysical Research Letters*, 40(16):4398–4403, 2013.

[114] Jacob T Seeley and David M Romps. Why does tropical convective available potential energy (cape) increase with warming? *Geophysical Research Letters*, 42(23):10–429, 2015.

[115] Rowan T Sutton, Buwen Dong, and Jonathan M Gregory. Land/sea warming ratio in response to climate change: Ipcc ar4 model results and comparison with observations. *Geophysical research letters*, 34(2), 2007.

[116] GJ Boer. The ratio of land to ocean temperature change under global warming. *Climate dynamics*, 37(11-12):2253–2270, 2011.

[117] David P Rowell and Richard G Jones. Causes and uncertainty of future summer drying over europe. *Climate Dynamics*, 27(2):281–299, 2006.

[118] Michael P. Byrne and Paul A. O'Gorman. Trends in continental temperature and humidity directly linked to ocean warming. *Proceedings of the National Academy of Sciences*, 115(19):4863–4868, April 2018.

[119] Jiao Chen, Aiguo Dai, Yaocun Zhang, and Kristen L Rasmussen. Changes in convective available potential energy and convective inhibition under global warming. *Journal of Climate*, 33(6):2025–2050, 2020.

[120] Paola Arias, Nicolas Bellouin, Erika Coppola, Richard Jones, Gerhard Krinner, Jochem Marotzke, Vaishali Naik, Matthew Palmer, Gian-Kaspar Plattner, Joeri Rogelj, et al. Climate change 2021: the physical science basis. *Contribution of Working Group I to the Sixth Assessment Report of the Intergovernmental Panel on Climate Change; technical summary*, 2021.

[121] T Schneider. *The Global Circulation of the Atmosphere*, chapter The thermal stratification of the extratropical troposphere. Princeton University Press, 2007.

[122] Maofeng Liu, Gabriel A Vecchi, James A Smith, and Thomas R Knutson. Causes of large projected increases in hurricane precipitation rates with global warming. *NPJ climate and atmospheric science*, 2(1):38, 2019.

[123] Marta Martinkova and Jan Kysely. Overview of observed clausius-clapeyron scaling of extreme precipitation in midlatitudes. *Atmosphere*, 11(8):786, 2020.

[124] P Alpert, T Ben-Gai, A Baharad, Y Benjamini, D Yekutieli, M Colacino, L Diodato, C Ramis, V Homar, R Romero, et al. The paradoxical increase of mediterranean extreme daily rainfall in spite of decrease in total values. *Geophysical research letters*, 29(11):31–1, 2002.

[125] Peter Berg, Christopher Moseley, and Jan O Haerter. Strong increase in convective precipitation in response to higher temperatures. *Nature Geoscience*, 6(3):181–185, 2013.

[126] Filippo Giorgi, Csaba Torma, Erika Coppola, Nikolina Ban, Christoph Schär, and Samuel Somot. Enhanced summer convective rainfall at alpine high elevations in response to climate warming. *Nature Geoscience*, 9(8):584–589, 2016.

[127] María Carmen Llasat, Anna del Moral, Maria Cortès, and Tomeu Rigo. Convective precipitation trends in the spanish mediterranean region. *Atmospheric Research*, 257:105581, 2021.

[128] Raquel Romera, Miguel Ángel Gaertner, Enrique Sánchez, Marta Domínguez, Juan Jesús González-Alemán, and Mario Marcello Miglietta. Climate change projections of medicanes with a large multi-model ensemble of regional climate models. *Global and Planetary Change*, 151:134–143, 2017.

[129] L Apicella, S Puca, M Lagasio, AN Meroni, M Milelli, N Vela, V Garbero, L Ferraris, and A Parodi. The predictive capacity of the high resolution weather research and forecasting model: a year-long verification over italy. *Bulletin of Atmospheric Science and Technology*, 2(1):3, 2021.

[130] E Fiori, L Ferraris, L Molini, F Siccardi, D Kranzlmueller, and A Parodi. Triggering and evolution of a deep convective system in the mediterranean sea: Modelling and observations at a very fine scale. *Quarterly Journal of the Royal Meteorological Society*, 143(703):927–941, 2017.

[131] Andrea Rossa, Katharina Liechti, Massimiliano Zappa, Michael Bruen, Urs Germann, Günther Haase, Christian Keil, and Peter Krahe. The cost 731 action: A review on uncertainty propagation in advanced hydro-meteorological forecast systems. *Atmospheric Research*, 100(2-3):150–167, 2011.

[132] B Vié, G Molinié, O Nuissier, B Vincendon, Vincent Ducrocq, F Bouttier, and E Richard. Hydro-meteorological evaluation of a convection-permitting ensemble prediction system for mediterranean heavy precipitating events. *Natural Hazards and Earth System Sciences*, 12(8):2631–2645, 2012.

[133] Alexandre B Pieri, Jost von Hardenberg, Antonio Parodi, and Antonello Provenzale. Sensitivity of precipitation statistics to resolution, microphysics, and convective parameterization: A case study with the high-resolution wrf climate model over europe. *Journal of Hydrometeorology*, 16(4):1857–1872, 2015.

[134] Andreas F Prein, Wolfgang Langhans, Giorgia Fosser, Andrew Ferrone, Nikolina Ban, Klaus Goergen, Michael Keller, Merja Tölle, Oliver Gutjahr, Frauke Feser, et al. A review on regional convection-permitting climate modeling: Demonstrations, prospects, and challenges. *Reviews of geophysics*, 53(2):323–361, 2015.

[135] Philippe Lucas-Picher, Daniel Argüeso, Erwan Brisson, Yves Tramblay, Peter Berg, Aude Lemonsu, Sven Kotlarski, and Cécile Caillaud. Convection-permitting modeling with regional climate models: Latest developments and next steps. *Wiley Interdisciplinary Reviews: Climate Change*, 12(6):e731, 2021.

[136] Giorgos E Ntagkounakis, Panagiotis T Nastos, and Yiannis Kapsomenakis. Statistical downscaling of era5 reanalysis precipitation over the complex terrain of greece. *Environmental Sciences Proceedings*, 26(1):81, 2023.

[137] Daniele Dalla Torre, Nicola Di Marco, Andrea Menapace, Diego Avesani, Maurizio Righetti, and Bruno Majone. Suitability of era5-land reanalysis dataset for hydrological modelling in the alpine region. *Journal of Hydrology: Regional Studies*, 52:101718, 2024.

[138] Valentina Vannucchi, Stefano Taddei, Valerio Capecchi, Michele Bendoni, and Carlo Brandini. Dynamical downscaling of era5 data on the north-western mediterranean sea: From atmosphere to high-resolution coastal wave climate. *Journal of Marine Science and Engineering*, 9(2):208, 2021.

[139] A Reder, M Raffa, R Padulano, G Rianna, and P Mercogliano. Characterizing extreme values of precipitation at very high resolution: An experiment over twenty european cities. *Weather and Climate Extremes*, 35:100407, 2022.

[140] Erika Coppola, Stefan Sobolowski, E Pichelli, F Raffaele, B Ahrens, I Anders, Nikolina Ban, Sophie Bastin, Michael Belda, D Belusic, et al. A first-of-its-kind multi-model convection permitting ensemble for investigating convective phenomena over europe and the mediterranean. *Climate Dynamics*, 55:3–34, 2020.

[141] Ramchandra Karki, Lars Gerlitz, Udo Schickhoff, Thomas Scholten, Jürgen Böhner, et al. Quantifying the added value of convection-permitting climate simulations in complex terrain: a systematic evaluation of wrf over the himalayas. *Earth System Dynamics*, 8(3):507–528, 2017.

[142] Steven C Sherwood, Sandrine Bony, and Jean-Louis Dufresne. Spread in model climate sensitivity traced to atmospheric convective mixing. *Nature*, 505(7481):37–42, 2014.

[143] Minh T Ha, Sophie Bastin, Philippe Drobinski, Lluís Fita, Jan Polcher, Olivier Bock, Marjolaine Chiriaco, Danijel Belušić, Cécile Caillaud, A Dobler, et al. Precipitation frequency in med-cordex and euro-cordex ensembles from 0.44° to convection-permitting resolution: impact of model resolution and convection representation. *Climate Dynamics*, pages 1–26, 2022.

[144] Kevin E Trenberth, Toshio Koike, and Kazutoshi Onogi. Progress and prospects for reanalysis for weather and climate. *Eos, Transactions American Geophysical Union*, 89(26):234–235, 2008.

[145] Hans Hersbach, Bill Bell, Paul Berrisford, Shoji Hirahara, András Horányi, Joaquín Muñoz-Sabater, Julien Nicolas, Carole Peubey, Raluca Radu, Dinand Schepers, et al. The era5 global reanalysis. *Quarterly Journal of the Royal Meteorological Society*, 146(730):1999–2049, 2020.

[146] William C Skamarock, Joseph B Klemp, Jimy Dudhia, David O Gill, Dale M Barker, Michael G Duda, Xiang-Yu Huang, Wei Wang, Jordan G Powers, et al. A description of the advanced research wrf version 3. *NCAR technical note*, 475:113, 2008.

[147] Christoph Bollmeyer, JD Keller, Christian Ohlwein, Sabrina Wahl, Susanne Crewell, P Friederichs, A Hense, J Keune, S Kneifel, IJQJotRMS Pscheidt, et al. Towards a high-resolution regional reanalysis for the european cordex domain. *Quarterly Journal of the Royal Meteorological Society*, 141(686):1–15, 2015.

[148] Per Dahlgren, Tomas Landelius, Per Kållberg, and Stefan Gollvik. A high-resolution regional reanalysis for europe. part 1: Three-dimensional reanalysis with the regional high-resolution limited-area model (hirlam). *Quarterly Journal of the Royal Meteorological Society*, 142(698):2119–2131, 2016.

[149] S Schimanke, M Ridal, P Le Moigne, L Berggren, P Undén, R Randriamampianina, U Andrea, E Bazile, A Bertelsen, P Brousseau, et al. Cerra sub-daily regional reanalysis data for europe on single levels from 1984 to present. *Copernicus Climate Change Service (C3S) Climate Data Store (CDS)*, 2021.

[150] Martin Ridal, Eric Bazile, Patrick Le Moigne, Roger Randriamampianina, Semjon Schimanke, Ulf Andrae, Lars Berggren, Pierre Brousseau, Per Dahlgren, Lisette Edvinsson, et al. Cerra, the copernicus european regional reanalysis system. *Quarterly Journal of the Royal Meteorological Society*, 2024.

[151] Emily Gleeson, Eoin Whelan, and John Hanley. Met éireann high resolution reanalysis for ireland. *Advances in Science and Research*, 14:49–61, 2017.

[152] Sabrina Wahl, Christoph Bollmeyer, Susanne Crewell, Clarissa Figura, Petra Friederichs, Andreas Hense, Jan D Keller, and Christian Ohlwein. A novel convective-scale regional reanalysis cosmo-rea2: Improving the representation of precipitation. *Meteorologische Zeitschrift*, 26(4):345–361, 2017.

[153] Ines Maria Luisa Cerenzia, Antonio Giordani, Tiziana Paccagnella, and Andrea Montani. Towards a convection-permitting regional reanalysis over the italian domain. *Meteorological Applications*, 29(5):e2092, 2022.

[154] Antonio Giordani, Ines Maria Luisa Cerenzia, Tiziana Paccagnella, and Silvana Di Sabatino. Sphera, a new convection-permitting regional reanalysis over italy: Improving the description of heavy rainfall. *Quarterly Journal of the Royal Meteorological Society*, 149(752):781–808, 2023.

[155] Mario Raffa, Alfredo Reder, Gian Franco Marras, Marco Mancini, Gabriella Scipione, Monia Santini, and Paola Mercogliano. Vhr-rea_it dataset: very high resolution dynamical downscaling of era5 reanalysis over italy by cosmo-clm. *Data*, 6(8):88, 2021.

[156] Jost von Hardenberg, Antonio Parodi, Alexandre B Pieri, and Antonello Provenzale. Impact of microphysics and convective parameterizations on dynamical downscaling for the european domain. In *Engineering Geology for Society and Territory-Volume 1: Climate Change and Engineering Geology*, pages 209–213. Springer, 2015.

[157] Song-You Hong, Yign Noh, and Jimy Dudhia. A new vertical diffusion package with an explicit treatment of entrainment processes. *Monthly weather review*, 134(9):2318–2341, 2006.

[158] Michael J Iacono, Eli J Mlawer, Shepard A Clough, and Jean-Jacques Morcrette. Impact of an improved longwave radiation model, rrtm, on the energy budget and thermodynamic properties of the ncar community climate model, ccm3. *Journal of Geophysical Research: Atmospheres*, 105(D11):14873–14890, 2000.

[159] Michael J Iacono, Jennifer S Delamere, Eli J Mlawer, Mark W Shephard, Shepard A Clough, and William D Collins. Radiative forcing by long-lived greenhouse gases: Calculations with the aer radiative transfer models. *Journal of Geophysical Research: Atmospheres*, 113(D13), 2008.

[160] Eli J Mlawer, Steven J Taubman, Patrick D Brown, Michael J Iacono, and Shepard A Clough. Radiative transfer for inhomogeneous atmospheres: Rrtm, a validated correlated-k model for the longwave. *Journal of Geophysical Research: Atmospheres*, 102(D14):16663–16682, 1997.

[161] Tatiana G Smirnova, John M Brown, and Stanley G Benjamin. Performance of different soil model configurations in simulating ground surface temperature and surface fluxes. *Monthly Weather Review*, 125(8):1870–1884, 1997.

[162] Tatiana G Smirnova, John M Brown, Stanley G Benjamin, and Dongsoo Kim. Parameterization of cold-season processes in the maps land-surface scheme. *Journal of Geophysical Research: Atmospheres*, 105(D3):4077–4086, 2000.

[163] Jongil Han and Hua-Lu Pan. Revision of convection and vertical diffusion schemes in the ncep global forecast system. *Weather and Forecasting*, 26(4):520–533, 2011.

[164] H Pan. Implementing a mass flux convection parameterization package for the ncep medium-range forecast model. *NMC Office Note*, 40, 1995.

[165] Joaquín Muñoz-Sabater, Emanuel Dutra, Anna Agustí-Panareda, Clément Albergel, Gabriele Arduini, Gianpaolo Balsamo, Souhail Boussetta, Margarita Choulga, Shaun Harrigan, Hans Hersbach, et al. Era5-land: A state-of-the-art global reanalysis dataset for land applications. *Earth system science data*, 13(9):4349–4383, 2021.

[166] Dirk Nikolaus Karger, Adam M Wilson, Colin Mahony, Niklaus E Zimmermann, and Walter Jetz. Global daily 1 km land surface precipitation based on cloud cover-informed downscaling. *Scientific Data*, 8(1):307, 2021.

[167] Richard C Cornes, Gerard van der Schrier, Else JM van den Besselaar, and Philip D Jones. An ensemble version of the e-obs temperature and precipitation data sets. *Journal of Geophysical Research: Atmospheres*, 123(17):9391–9409, 2018.

[168] Aart Overeem, Else van den Besselaar, Gerard van der Schrier, Jan Fokke Meirink, Emiel van der Plas, and Hidde Leijnse. Euradclim: the european climatological high-resolution gauge-adjusted radar precipitation dataset. *Earth System Science Data Discussions*, 2022:1–34, 2022.

[169] Xiaojing Wu, Jianbin Su, Weiwei Ren, Haishen Lü, and Fei Yuan. Statistical comparison and hydrological utility evaluation of era5-land and imerg precipitation products on the tibetan plateau. *Journal of Hydrology*, 620:129384, 2023.

[170] Matthew J Menne, Imke Durre, Russell S Vose, Byron E Gleason, and Tamara G Houston. An overview of the global historical climatology network-daily database. *Journal of atmospheric and oceanic technology*, 29(7):897–910, 2012.

[171] Nynke Hofstra, Malcolm Haylock, Mark New, and Phil D Jones. Testing e-obs european high-resolution gridded data set of daily precipitation and surface temperature. *Journal of Geophysical Research: Atmospheres*, 114(D21), 2009.

[172] Moritz Bandhauer, Francesco Isotta, Mónika Lakatos, Cristian Lussana, Line Båserud, Beatrix Izsák, Olivér Szentes, Ole Einar Tveito, and Christoph Frei. Evaluation of daily precipitation analyses in e-obs (v19. 0e) and era5 by comparison to regional high-resolution datasets in european regions. *International Journal of Climatology*, 42(2):727–747, 2022.

[173] Elizabeth E Ebert. Fuzzy verification of high-resolution gridded forecasts: a review and proposed framework. *Meteorological Applications: A journal of forecasting, practical applications, training techniques and modelling*, 15(1):51–64, 2008.

[174] Andrea Rossa, Pertti Nurmi, and Elizabeth Ebert. Overview of methods for the verification of quantitative precipitation forecasts. In *Precipitation: Advances in measurement, estimation and prediction*, pages 419–452. Springer, 2008.

[175] Nigel M Roberts and Humphrey W Lean. Scale-selective verification of rainfall accumulations from high-resolution forecasts of convective events. *Monthly Weather Review*, 136(1):78–97, 2008.

[176] Bradley Efron. Bootstrap methods: another look at the jackknife. In *Breakthroughs in statistics: Methodology and distribution*, pages 569–593. Springer, 1992.

[177] Alessandro Dosio, Hans-Jürgen Panitz, Martina Schubert-Frisius, and Daniel Lüthi. Dynamical downscaling of cmip5 global circulation models over cordex-africa with cosmo-clm: evaluation over the present climate and analysis of the added value. *Climate Dynamics*, 44:2637–2661, 2015.

[178] Kirsten Warrach-Sagi, Thomas Schwitalla, Volker Wulfmeyer, and Hans-Stefan Bauer. Evaluation of a climate simulation in europe based on the wrf–noah model system: precipitation in germany. *Climate Dynamics*, 41:755–774, 2013.

[179] Francesco A Isotta, Christoph Frei, Viktor Weilguni, M Percec Tadic, Pierre Lassegues, Bruno Rudolf, Valentina Pavan, Carlo Cacciamani, Gabriele Antolini, Sara M Ratto, et al. The climate of daily precipitation in the alps: development and analysis of a high-resolution grid dataset from pan-alpine rain-gauge data. *Int. J. Climatol*, 34(5):1657–1675, 2014.

[180] David A Lavers, Adrian Simmons, Freja Vamborg, and Mark J Rodwell. An evaluation of era5 precipitation for climate monitoring. *Quarterly Journal of the Royal Meteorological Society*, 148(748):3152–3165, 2022.

[181] Pauline Rivoire, Olivia Martius, and Philippe Naveau. A comparison of moderate and extreme era-5 daily precipitation with two observational data sets. *Earth and Space Science*, 8(4):e2020EA001633, 2021.

[182] E. Galanaki, K. Lagouvardos, V. Kotroni, E. Flaounas, and A. Argiriou. Thunderstorm climatology in the mediterranean using cloud-to-ground lightning observations. *Atmospheric Research*, 207:136–144, July 2018.

[183] Enrico Arnone, József Bór, Olivier Chanrion, Veronika Barta, Stefano Dietrich, Carl-Fredrik Enell, Thomas Farges, Martin Füllekrug, Antti Kero, Roberto Labanti, Antti Mäkelä, Keren Mezuman, Anna Odzimek, Martin Popek, Marco Prevedelli, Marco Ridolfi, Serge Soula, Diego Valeri, Oscar van der Velde, Yoav Yair, Ferruccio Zanotti, Przemyslaw Zoladek, and Torsten Neubert. Climatology of transient luminous events

and lightning observed above europe and the mediterranean sea. *Surveys in Geophysics*, 41(2):167–199, November 2019.

[184] H J Punge and M Kunz. Hail observations and hailstorm characteristics in europe: A review. *Atmospheric Research*, 176:159–184, 2016.

[185] Andrew J Dowdy, Joshua Soderholm, Jordan Brook, Andrew Brown, and Hamish McGowan. Quantifying hail and lightning risk factors using long-term observations around australia. *Journal of Geophysical Research: Atmospheres*, 125(21):2020JD033101, 2020.

[186] F Silvestro, S Gabellani, F Delogu, R Rudari, and G Boni. Exploiting remote sensing land surface temperature in distributed hydrological modelling: the example of the continuum model. *Hydrology and Earth System Sciences*, 17(1):39–62, 2013.

[187] F Silvestro, L Rossi, L Campo, A Parodi, E Fiori, R Rudari, and L Ferraris. Impact-based flash-flood forecasting system: Sensitivity to high resolution numerical weather prediction systems and soil moisture. *Journal of Hydrology*, 572:388–402, 2019.

[188] Víctor Resco de Dios and Rachael H Nolan. Some challenges for forest fire risk predictions in the21st century. *Forests*, 12(4):469, 2021.

[189] Mortimer M Müller, Lena Vilà-Vilardell, and Harald Vacik. Towards an integrated forest fire danger assessment system for the european alps. *Ecological Informatics*, 60:101151, 2020.

[190] Nicolò Perello, Andrea Trucchia, Mirko D'Andrea, Giorgio Meschi, Farzad Ghasemiazma, Silvia Degli Esposti, Paolo Fiorucci, Luca Ferraris, Andrea Gollini, and Dario Negro. Fuel-aware forest fire danger rating system risico: a comparative study for italy. *International Journal of Wildland Fire*, 34(9):WF25023, 2025.

[191] Marcos Francos and Xavier Úbeda. Prescribed fire management. *Current Opinion in Environmental Science & Health*, 21:100250, 2021.

[192] Martina Lagasio, Antonio Parodi, Luca Pulvirenti, Agostino N Meroni, Giorgio Boni, Nazzareno Pierdicca, Frank S Marzano, Lorenzo Luini, Giovanna Venuti, Eugenio Realini, et al. A synergistic use of a high-resolution numerical weather prediction model and high-resolution earth observation products to improve precipitation forecast. *Remote Sensing*, 11(20):2387, 2019.

[193] Zhaoxia Pu. Surface data assimilation and near-surface weather prediction over complex terrain. *Data Assimilation for Atmospheric, Oceanic and Hydrologic Applications (Vol. III)*, pages 219–240, 2017.

[194] Nikolina Ban, Cécile Caillaud, Erika Coppola, Emanuela Pichelli, Stefan Sobolowski, Marianna Adinolfi, Bodo Ahrens, Antoinette Alias, Ivonne Anders, Sophie Bastin, et al. The first multi-model ensemble of regional climate simulations at kilometer-scale resolution, part i: evaluation of precipitation. *Climate Dynamics*, 57:275–302, 2021.

[195] Emanuela Pichelli, Erika Coppola, Stefan Sobolowski, Nikolina Ban, Filippo Giorgi, Paolo Stocchi, Antoinette Alias, Danijel Belušić, Segolene Berthou, Cecile Caillaud, et al. The first multi-model ensemble of regional climate simulations at kilometer-scale resolution part 2: historical and future simulations of precipitation. *Climate Dynamics*, 56:3581–3602, 2021.

[196] Alban Farchi, Patrick Laloyaux, Massimo Bonavita, and Marc Bocquet. Using machine learning to correct model error in data assimilation and forecast applications. *Quarterly Journal of the Royal Meteorological Society*, 147(739):3067–3084, 2021.

[197] Bogdan Bochenek and Zbigniew Ustrnul. Machine learning in weather prediction and climate analyses—applications and perspectives. *Atmosphere*, 13(2):180, 2022.

[198] Iman Gourdazi, Davide Fazzini, Claudia Pasquero, Agostino Meroni, and Matteo Borgnino. A machine learning-based backward extension of imerg daily precipitation over the greater alpine region. *Atmospheric Research*, 2026.

[199] Lars Isaksen, M Bonavita, R Buizza, M Fisher, J Haseler, M Leutbecher, and Laure Raynaud. Ensemble of data assimilations at ecmwf. *ECMWF Technical Memoranda*, 2010.

[200] SE Theis, A Hense, and U Damrath. Probabilistic precipitation forecasts from a deterministic model: A pragmatic approach. *Meteorological Applications*, 12(3):257–268, 2005.

[201] Isaac M Held and Brian J Soden. Robust responses of the hydrological cycle to global warming. *Journal of climate*, 19(21):5686–5699, 2006.

[202] David M Romps. Response of tropical precipitation to global warming. *Journal of the Atmospheric Sciences*, 68(1):123–138, 2011.

[203] Paul A O'Gorman. Precipitation extremes under climate change. *Current climate change reports*, 1(2):49–59, 2015.

[204] Paul A O'Gorman and Tapio Schneider. The physical basis for increases in precipitation extremes in simulations of 21st-century climate change. *Proceedings of the National Academy of Sciences*, 106(35):14773–14777, 2009.

[205] Masahiro Sugiyama, Hideo Shiogama, and Seita Emori. Precipitation extreme changes exceeding moisture content increases in miroc and ipcc climate models. *Proceedings of the National Academy of Sciences*, 107(2):571–575, 2010.

[206] Stephan Pfahl, Paul A O'Gorman, and Erich M Fischer. Understanding the regional pattern of projected future changes in extreme precipitation. *Nature Climate Change*, 7(6):423–427, 2017.

[207] Martin S. Singh and Paul A. O'Gorman. Influence of microphysics on the scaling of precipitation extremes with temperature. *Geophysical Research Letters*, 41(16):6037–6044, August 2014.

[208] Lewis D Grasso. The differentiation between grid spacing and resolution and their application to numerical... *Bulletin of the American Meteorological Society*, 81(3), 2000.

[209] William C Skamarock. Evaluating mesoscale nwp models using kinetic energy spectra. *Monthly weather review*, 132(12):3019–3032, 2004.

[210] Kelly Lombardo and Miranda Bitting. A climatology of convective precipitation over europe. *Monthly Weather Review*, 152(7):1555–1585, 2024.

[211] Kevin E Trenberth, Aiguo Dai, Roy M Rasmussen, and David B Parsons. The changing character of precipitation. *Bulletin of the American Meteorological Society*, 84(9):1205–1218, 2003.

[212] Theodore G Shepherd. Atmospheric circulation as a source of uncertainty in climate change projections. *Nature Geoscience*, 7(10):703–708, 2014.

[213] Simone Fatichi, Valeriy Y Ivanov, Athanasios Paschalis, Nadav Peleg, Peter Molnar, Stefan Rimkus, Jongho Kim, Paolo Burlando, and Enrica Caporali. Uncertainty partition challenges the predictability of vital details of climate change. *Earth's Future*, 4(5):240–251, 2016.

[214] Elizabeth J Kendon, Nikolina Ban, Nigel M Roberts, Hayley J Fowler, Malcolm J Roberts, Steven C Chan, Jason P Evans, Giorgia Fosser, and Jonathan M Wilkinson. Do convection-permitting regional climate models improve projections of future precipitation change? *Bulletin of the American Meteorological Society*, 98(1):79–93, 2017.

[215] Emma E Aalbers, Geert Lenderink, Erik van Meijgaard, and Bart JJM van den Hurk. Local-scale changes in mean and heavy precipitation in western europe, climate change or internal variability? *Climate Dynamics*, 50(11):4745–4766, 2018.

[216] Syukuro Manabe, Richard T Wetherald, and Ronald J Stouffer. Summer dryness due to an increase of atmospheric co2 concentration. *Climatic Change*, 3(4):347–386, 1981.

[217] S Manabe and RT Wetherald. Large-scale changes of soil wetness induced by an increase in atmospheric carbon dioxide. *Journal of Atmospheric Sciences*, 44(8):1211–1236, 1987.

[218] Elfatih A. B. Eltahir. A soil moisture–rainfall feedback mechanism: 1. theory and observations. *Water Resources Research*, 34(4):765–776, April 1998.

[219] Christoph Schär, Daniel Lüthi, Urs Beyerle, and Erdmann Heise. The soil–precipitation feedback: A process study with a regional climate model. *Journal of Climate*, 12(3):722–741, March 1999.

[220] Kirsten L. Findell and Elfatih A. B. Eltahir. Atmospheric controls on soil moisture–boundary layer interactions. part i: Framework development. *Journal of Hydrometeorology*, 4(3):552–569, June 2003.

[221] Sonia I Seneviratne, Thierry Corti, Edouard L Davin, Martin Hirschi, Eric B Jaeger, Irene Lehner, Boris Orlowsky, and Adriaan J Teuling. Investigating soil moisture–climate interactions in a changing climate: A review. *Earth-Science Reviews*, 99(3-4):125–161, 2010.

[222] Fengfei Song, Guang J Zhang, V Ramanathan, and L Ruby Leung. Trends in surface equivalent potential temperature: A more comprehensive metric for global warming and weather extremes. *Proceedings of the National Academy of Sciences*, 119(6):e2117832119, 2022.

[223] M Tous and R Romero. Meteorological environments associated with medicane development. *International Journal of Climatology*, 33(1):1–14, 2013.

[224] Francesco Ragone, Monica Mariotti, Antonio Parodi, Jost Von Hardenberg, and Claudia Pasquero. A climatological study of western mediterranean medicanes in numerical simulations with explicit and parameterized convection. *Atmosphere*, 9(10):397, 2018.

[225] Wei Zhang, Gabriele Villarini, Enrico Scoccimarro, and Francesco Napolitano. Examining the precipitation associated with medicanes in the high-resolution era-5 reanalysis data. *International Journal of Climatology*, 41:E126–E132, 2021.

[226] Alba de la Vara, Jesús Gutiérrez-Fernández, Juan Jesús González-Alemán, and Miguel A Gaertner. Characterization of medicanes with a minimal number of geopotential levels. *International Journal of Climatology*, 41(5):3300–3316, 2021.

[227] Mario Marcello Miglietta and Richard Rotunno. Development mechanisms for mediterranean tropical-like cyclones (medicanes). *Quarterly Journal of the Royal Meteorological Society*, 145(721):1444–1460, 2019.

[228] George Varlas, Ioannis Pytharoulis, Gert-Jan Steeneveld, Petros Katsafados, and Anastasios Papadopoulos. Investigating the impact of sea surface temperature on the development of the mediterranean tropical-like cyclone "ianos" in 2020. *Atmospheric Research*, 291:106827, 2023.

[229] Jesús Gutiérrez-Fernández, Mario Marcello Miglietta, Juan J González-Alemán, and Miguel Angel Gaertner. A new refinement of mediterranean tropical-like cyclones characteristics. *Geophysical Research Letters*, 51(8):e2023GL106429, 2024.

[230] Leone Cavicchia, Hans von Storch, and Silvio Gualdi. A long-term climatology of medicanes. *Climate Dynamics*, 43:1183–1195, 2014.

[231] Mario Marcello Miglietta, Emmanouil Flaounas, Juán Jesus González-Alemán, Giulia Panegrossi, Miguel Angel Gaertner, Florian Pantillon, Claudia Pasquero, David Schultz, Leo Pio D'Adderio, Stavros Dafis, et al. Defining medicanes: Bridging the knowledge gap between tropical and extratropical cyclones in the mediterranean. *Bulletin of the American Meteorological Society*, 2025.

[232] Kerry Emanuel. Genesis and maintenance of" mediterranean hurricanes". *Advances in Geosciences*, 2:217–220, 2005.

[233] Lluís Fita and Emmanouil Flaounas. Medicanes as subtropical cyclones: the december 2005 case from the perspective of surface pressure tendency diagnostics and atmospheric water budget. *Quarterly Journal of the Royal Meteorological Society*, 144(713):1028–1044, 2018.

[234] Edoardo Mazza, Uwe Ulbrich, and Rupert Klein. The tropical transition of the october 1996 medicane in the western mediterranean sea: A warm seclusion event. *Monthly Weather Review*, 145(7):2575–2595, 2017.

[235] Emmanouil Flaounas, Leonardo Aragão, Lisa Bernini, Stavros Dafis, Benjamin Doiteau, Helena Flocas, Suzanne L. Gray, Alexia Karwat, John Kouroutzoglou, Piero Lionello, et al. A composite approach to produce reference datasets for extratropical cyclone tracks: Application to mediterranean cyclones. *Weather and Climate Dynamics Discussions*, 2023:1–32, 2023.

[236] Hans Hersbach, Bill Bell, Paul Berrisford, Shoji Hirahara, András Horányi, Joaquín Muñoz-Sabater, Julien Nicolas, Carole Peubey, Raluca Radu, Dinand Schepers, et al. The era5 global reanalysis. *Quarterly Journal of the Royal Meteorological Society*, 146(730):1999–2049, 2020.

[237] Yonatan Givon, Or Hess, Emmanouil Flaounas, Jennifer L Catto, Michael Sprenger, and Shira Raveh-Rubin. Process-based classification of mediterranean cyclones using potential vorticity. *EGUsphere*, 2023:1–36, 2023.

[238] MM Miglietta, S Laviola, A Malvaldi, D Conte, V Levizzani, and C Price. Analysis of tropical-like cyclones over the mediterranean sea through a combined modeling and satellite approach. *Geophysical Research Letters*, 40(10):2400–2405, 2013.

[239] MA Picornell, Joan Campins, and Agustí Jansà. Detection and thermal description of medicanes from numerical simulation. *Natural Hazards and Earth System Sciences*, 14(5):1059–1070, 2014.

[240] Guido Cioni, P Malguzzi, and A Buzzi. Thermal structure and dynamical precursor of a mediterranean tropical-like cyclone. *Quarterly Journal of the Royal Meteorological Society*, 142(697):1757–1766, 2016.

[241] Robin Noyelle, Uwe Ulbrich, Nico Becker, and Edmund P Meredith. Assessing the impact of sea surface temperatures on a simulated medicane using ensemble simulations. *Natural Hazards and Earth System Sciences*, 19(4):941–955, 2019.

[242] Miguel Ángel Gaertner, Juan Jesús González-Alemán, Raquel Romera, Marta Domínguez, Victoria Gil, Enrique Sánchez, Clemente Gallardo, Mario Marcello Miglietta, Kevin JE Walsh, Dmitry V Sein, et al. Simulation of medicanes over the mediterranean sea in a regional climate model ensemble: impact of ocean–atmosphere coupling and increased resolution. *Climate dynamics*, 51:1041–1057, 2018.

[243] Kevin Walsh, Filippo Giorgi, and Erika Coppola. Mediterranean warm-core cyclones in a warmer world. *Climate dynamics*, 42:1053–1066, 2014.

[244] Stephen T Garner, Isaac M Held, Thomas Knutson, and Joseph Sirutis. The roles of wind shear and thermal stratification in past and projected changes of atlantic tropical cyclone activity. *Journal of climate*, 22(17):4723–4734, 2009.

[245] Gabriel A Vecchi, Stephan Fueglistaler, Isaac M Held, Thomas R Knutson, and Ming Zhao. Impacts of atmospheric temperature trends on tropical cyclone activity. *Journal of climate*, 26(11):3877–3891, 2013.

[246] Allison A Wing, Kerry Emanuel, and Susan Solomon. On the factors affecting trends and variability in tropical cyclone potential intensity. *Geophysical Research Letters*, 42(20):8669–8677, 2015.

[247] Kerry Emanuel. 100 years of progress in tropical cyclone research. *Meteorological Monographs*, 59:15–1, 2018.

[248] Jing Xu, Yuqing Wang, and Chi Yang. Factors affecting the variability of maximum potential intensity (mpi) of tropical cyclones over the north atlantic. *Journal of Geophysical Research: Atmospheres*, 124(13):6654–6668, 2019.

[249] Marja Bister and Kerry A Emanuel. Low frequency variability of tropical cyclone potential intensity 1. interannual to interdecadal variability. *Journal of Geophysical Research: Atmospheres*, 107(D24):ACL–26, 2002.

[250] Daniel M Gilford. pypi (v1. 3): Tropical cyclone potential intensity calculations in python. *Geoscientific Model Development*, 14(5):2351–2369, 2021.

[251] Shuguang Wang, Suzana J Camargo, Adam H Sobel, and Lorenzo M Polvani. Impact of the tropopause temperature on the intensity of tropical cyclones: An idealized study using a mesoscale model. *Journal of the Atmospheric Sciences*, 71(11):4333–4348, 2014.

[252] Stavros Dafis, Chantal Claud, Vassiliki Kotroni, Konstantinos Lagouvardos, and Jean-François Rysman. Insights into the convective evolution of mediterranean tropical-like cyclones. *Quarterly Journal of the Royal Meteorological Society*, 146(733):4147–4169, 2020.

[253] CD Thorncroft and HA Flocas. A case study of saharan cyclogenesis. *Monthly weather review*, 125(6):1147–1165, 1997.

[254] Panagiotis Maheras, HA Flocas, Ioannis Patrikas, and Chr Anagnostopoulou. A 40 year objective climatology of surface cyclones in the mediterranean region: spatial and temporal distribution. *International Journal of Climatology: A Journal of the Royal Meteorological Society*, 21(1):109–130, 2001.

[255] Helena A Flocas, Ian Simmonds, John Kouroutzoglou, Kevin Keay, Maria Hatzaki, Vicky Bricolas, and Demosthenes Asimakopoulos. On cyclonic tracks over the eastern mediterranean. *Journal of Climate*, 23(19):5243–5257, 2010.

[256] Uwe Ulbrich, Piero Lionello, Danijel Belušić, Jucundus Jacobeit, Peter Knippertz, Franz G Kuglitsch, Gregor C Leckebusch, Jürg Luterbacher, Maurizio Maugeri, Panagiotis Maheras, et al. *The Climate of the Mediterranean Region*, chapter Climate of the Mediterranean: synoptic patterns, temperature, precipitation, winds, and their extremes. Elsevier, 2012.

[257] Marco Reale and Piero Lionello. Synoptic climatology of winter intense precipitation events along the mediterranean coasts. *Natural Hazards and Earth System Sciences*, 13(7):1707–1722, 2013.

[258] Khaled Ammar, Mossad El-Metwally, Mansour Almazroui, and MM Abdel Wahab. A climatological analysis of saharan cyclones. *Climate dynamics*, 43:483–501, 2014.

[259] Veronika N Maslova, Elena N Voskresenskaya, Andrey S Lubkov, Aleksandr V Yurovsky, Viktor Y Zhuravskiy, and Vladislav P Evstigneev. Intense cyclones in the black sea region: change, variability, predictability and manifestations in the storm activity. *Sustainability*, 12(11):4468, 2020.

[260] Isabel F Trigo, Trevor D Davies, and Grant R Bigg. Objective climatology of cyclones in the mediterranean region. *Journal of climate*, 12(6):1685–1696, 1999.

[261] Piero Lionello, Isabel F Trigo, Victoria Gil, Margarida LR Liberato, Katrin M Nissen, Joaquim G Pinto, Christoph C Raible, Marco Reale, Annalisa Tanzarella, Ricardo M Trigo, et al. Objective climatology of cyclones in the mediterranean region: a consensus view among methods with different system identification and tracking criteria. *Tellus A: Dynamic Meteorology and Oceanography*, 68(1):29391, 2016.

[262] G Kotsias, CJ Lolis, N Hatzianastassiou, N Bakas, P Lionello, and A Bartzokas. Objective climatology and classification of the mediterranean cyclones based on the era5 data set and the use of the results for the definition of seasons. *Theoretical and Applied Climatology*, 152(1):581–597, 2023.

[263] Emmanouil Flaounas, Philippe Drobinski, and Sophie Bastin. Dynamical downscaling of ipsl-cm5 cmip5 historical simulations over the mediterranean: benefits on the representation of regional surface winds and cyclogenesis. *Climate dynamics*, 40(9):2497–2513, 2013.

[264] Laura A Bakkensen, Doo-Sun R Park, and Raja Shanti Ranjan Sarkar. Climate costs of tropical cyclone losses also depend on rain. *Environmental Research Letters*, 13(7):074034, 2018.

[265] Rongshui Qin, Nima Khakzad, and Jiping Zhu. An overview of the impact of hurricane harvey on chemical and process facilities in texas. *International journal of disaster risk reduction*, 45:101453, 2020.

[266] Shanshan Wen, Buda Su, Yanjun Wang, Thomas Fischer, Xiucang Li, Yizhou Yin, Gao Chao, Run Wang, and Tong Jiang. Economic sector loss from influential tropical cyclones and relationship to associated rainfall and wind speed in china. *Global and Planetary Change*, 169:224–233, 2018.

[267] Paul R Field and Robert Wood. Precipitation and cloud structure in midlatitude cyclones. *Journal of climate*, 20(2):233–254, 2007.

[268] Vineel Yettella and Jennifer E Kay. How will precipitation change in extratropical cyclones as the planet warms? insights from a large initial condition climate model ensemble. *Climate Dynamics*, 49(5-6):1765–1781, 2017.

[269] Catherine M Naud, James F Booth, Matthew Lebsock, and Mircea Grecu. Observational constraint for precipitation in extratropical cyclones: Sensitivity to data sources. *Journal of Applied Meteorology and Climatology*, 57(4):991–1009, 2018.

[270] Emmanouil Flaounas, Vassiliki Kotroni, Konstantinos Lagouvardos, Suzanne L Gray, Jean-François Rysman, and Chantal Claud. Heavy rainfall in mediterranean cyclones. part i: contribution of deep convection and warm conveyor belt. *Climate dynamics*, 50(7):2935–2949, 2018.

[271] Manuel Lonfat, Frank D Marks Jr, and Shuyi S Chen. Precipitation distribution in tropical cyclones using the tropical rainfall measuring mission (trmm) microwave imager: A global perspective. *Monthly Weather Review*, 132(7):1645–1660, 2004.

[272] Rong Du, Guosheng Zhang, and Bin Huang. Observed surface wind field structure of severe tropical cyclones and associated precipitation. *Remote Sensing*, 15(11):2808, 2023.

[273] Edgar Dolores-Tesillos, Franziska Teubler, and Stephan Pfahl. Future changes in north atlantic winter cyclones in cesm-le–part 1: Cyclone intensity, potential vorticity anomalies, and horizontal wind speed. *Weather and Climate Dynamics*, 3(2):429–448, 2022.

[274] Claudio Sanchez, Suzanne Gray, Ambrogio Volonte, Florian Pantillon, Segolene Berthou, and Silvio Davolio. How a warmer mediterranean preconditions the upper-level environment for the development of medicane ianos. *EGUsphere*, 2023:1–35, 2023.

[275] Kerry Emanuel, Tommaso Alberti, Stella Bourdin, Suzana J Camargo, Davide Faranda, Emmanouil Flaounas, Juan Jesus Gonzalez-Aleman, Chia-Ying Lee, Mario Marcello Miglietta, Claudia Pasquero, et al. Cyclops: A unified framework for surface flux-driven cyclones outside the tropics. *Weather and Climate Dynamics*, 6(3):901–926, 2025.

[276] John Kaplan and Mark DeMaria. Large-scale characteristics of rapidly intensifying tropical cyclones in the north atlantic basin. *Weather and forecasting*, 18(6):1093–1108, 2003.

[277] Russell L Elsberry and Richard A Jeffries. Vertical wind shear influences on tropical cyclone formation and intensification during tcm-92 and tcm-93. *Monthly Weather Review*, 124(7):1374–1387, 1996.

[278] Martin LM Wong and Johnny CL Chan. Tropical cyclone intensity in vertical wind shear. *Journal of the atmospheric sciences*, 61(15):1859–1876, 2004.

[279] Richard Anthes. *Tropical cyclones: their evolution, structure and effects*, volume 19. Springer, 2016.

[280] John Kaplan and Mark DeMaria. A simple empirical model for predicting the decay of tropical cyclone winds after landfall. *Journal of Applied Meteorology and Climatology*, 34(11):2499–2512, 1995.

[281] Wei Mei and Claudia Pasquero. Spatial and temporal characterization of sea surface temperature response to tropical cyclones. *Journal of Climate*, 26(11):3745–3765, 2013.

[282] Wei Mei, Claudia Pasquero, and François Primeau. The effect of translation speed upon the intensity of tropical cyclones over the tropical ocean. *Geophysical Research Letters*, 39(7), 2012.

[283] Fabrizio d'Ortenzio, Daniele Iudicone, Clement de Boyer Montegut, Pierre Testor, David Antoine, Salvatore Marullo, Rosalia Santoleri, and Gurvan Madec. Seasonal variability of the mixed layer depth in the mediterranean sea as derived from in situ profiles. *Geophysical Research Letters*, 32(12), 2005.

[284] Francisco Pastor, Jose Antonio Valiente, and Samiro Khodayar. A warming mediterranean: 38 years of increasing sea surface temperature. *Remote sensing*, 12(17):2687, 2020.

[285] Andrea Pisano, Salvatore Marullo, Vincenzo Artale, Federico Falcini, Chunxue Yang, Francesca Elisa Leonelli, Rosalia Santoleri, and Bruno Buongiorno Nardelli. New evidence of mediterranean climate change and variability from sea surface temperature observations. *Remote Sensing*, 12(1):132, 2020.

[286] Mohamed Shaltout and Anders Omstedt. Recent sea surface temperature trends and future scenarios for the mediterranean sea. *Oceanologia*, 56(3):411–443, 2014.

[287] Geoffrey K Vallis, Pablo Zurita-Gotor, Cameron Cairns, and Joseph Kidston. Response of the large-scale structure of the atmosphere to global warming. *Quarterly Journal of the Royal Meteorological Society*, 141(690):1479–1501, 2015.

[288] Martin Stendel, Jennifer Francis, Rachel White, Paul D Williams, and Tim Woollings. The jet stream and climate change. In *Climate change*, pages 327–357. Elsevier, 2021.

[289] Woosok Moon, Baek-Min Kim, Gun-Hwan Yang, and John S Wettlaufer. Wavier jet streams driven by zonally asymmetric surface thermal forcing. *Proceedings of the National Academy of Sciences*, 119(38):e2200890119, 2022.

[290] Russell Blackport and James A Screen. Insignificant effect of arctic amplification on the amplitude of midlatitude atmospheric waves. *Science advances*, 6(8):eaay2880, 2020.

[291] Jesús Gutiérrez-Fernández, Mario Marcello Miglietta, Juan Jesús González-Alemán, and Miguel Ángel Gaertner. Characteristics of medicanes using era-5 reanalysis. In *EGU General Assembly Conference Abstracts*, pages EGU–483, 2023.

[292] R Romero and K Emanuel. Medicane risk in a changing climate. *Journal of Geophysical Research: Atmospheres*, 118(12):5992–6001, 2013.

[293] Jean-Pierre Chaboureau, Florian Pantillon, Dominique Lambert, Evelyne Richard, and Chantal Claud. Tropical transition of a mediterranean storm by jet crossing. *Quarterly Journal of the Royal Meteorological Society*, 138(664):596–611, 2012.

[294] Mika Rantanen, Jouni Räisänen, Victoria A Sinclair, Juha Lento, and Heikki Järvinen. The extratropical transition of hurricane ophelia (2017) as diagnosed with a generalized omega equation and vorticity equation. *Tellus A: Dynamic Meteorology and Oceanography*, 72(1):1–26, 2020.

[295] Lars R Schade and Kerry A Emanuel. The ocean's effect on the intensity of tropical cyclones: Results from a simple coupled atmosphere–ocean model. *Journal of the atmospheric sciences*, 56(4):642–651, 1999.

[296] Swen Jullien, Patrick Marchesiello, Christophe E Menkes, Jerome Lefevre, Nicolas C Jourdain, Guillaume Samson, and Matthieu Lengaigne. Ocean feedback to tropical cyclones: climatology and processes. *Climate dynamics*, 43:2831–2854, 2014.

[297] Benjamin R Johnston, William J Randel, and Jeremiah P Sjoberg. Evaluation of tropospheric moisture characteristics among cosmic-2, era5 and merra-2 in the tropics and subtropics. *Remote Sensing*, 13(5):880, 2021.

[298] Christopher J Slocum, Muhammad Naufal Razin, John A Knaff, and Justin P Stow. Does era5 mark a new era for resolving the tropical cyclone environment? *Journal of Climate*, 35(21):7147–7164, 2022.

[299] Florian Pantillon, Silvio Davolio, Elenio Avolio, Carlos Calvo-Sancho, Diego Saul Carrió, Stavros Dafis, Emanuele Silvio Gentile, Juan Jesus Gonzalez-Aleman, Suzanne Gray, Mario Marcello Miglietta, et al. The crucial representation of deep convection for the cyclogenesis of medicane ianos. *Weather and Climate Dynamics*, 5(3):1187–1205, 2024.

[300] Rémi Gandoin and Jorge Garza. Underestimation of strong wind speeds offshore in era5: evidence, discussion and correction. *Wind Energy Science*, 9(8):1727–1745, 2024.

[301] Marie-Noëlle Bouin and Cindy Lebeaupin Brossier. Surface processes in the 7 november 2014 medicane from air–sea coupled high-resolution numerical modelling. *Atmospheric Chemistry and Physics*, 20(11):6861–6881, 2020.

[302] Christopher Velden, John Knaff, Derrick Herndon, Alexis Mouche, Jeffrey Hawkins, Giulia Panegrossi, Ad Stoffelen, Joseph Courtney, Taiga Tsukada, and Anne-Claire Fontan. Recent innovations in satellite-based applications and their impacts on tropical cyclone analyses and forecasts. *Journal of the European Meteorological Society*, 2:100011, 2025.

[303] M Tous, Giuseppe Zappa, R Romero, Len Shaffrey, and Pier Luigi Vidale. Projected changes in medicanes in the hadgem3 n512 high-resolution global climate model. *Climate Dynamics*, 47(5):1913–1924, 2016.

[304] Gabriel A Vecchi and Brian J Soden. Effect of remote sea surface temperature change on tropical cyclone potential intensity. *Nature*, 450(7172):1066–1070, 2007.

[305] Mingfang Ting, Suzana J Camargo, Cuihua Li, and Yochanan Kushnir. Natural and forced north atlantic hurricane potential intensity change in cmip5 models. *Journal of Climate*, 28(10):3926–3942, 2015.

Appendix A

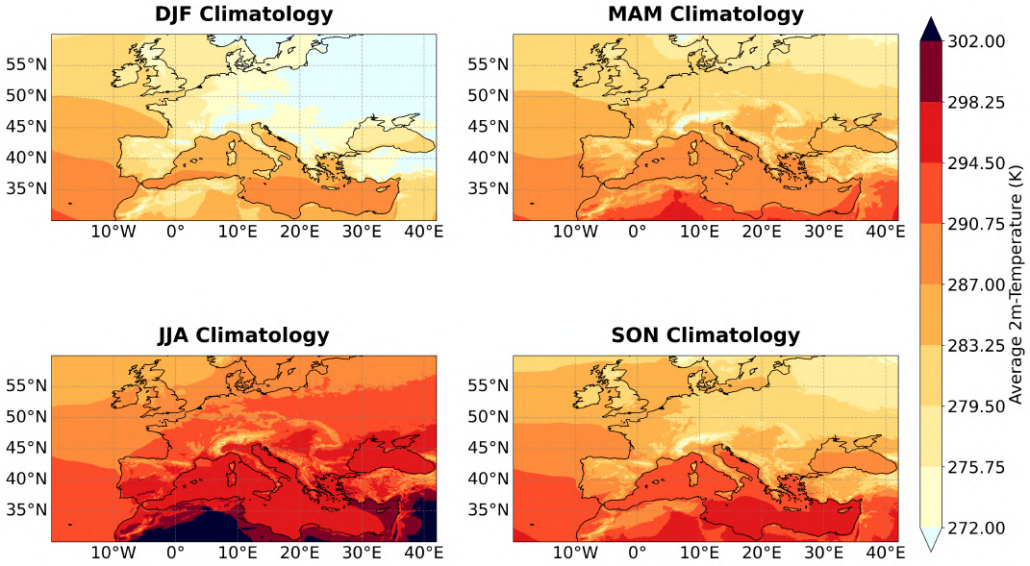

Fig. A.1 Seasonal climatology of 2m temperature between 1981 and 2022.

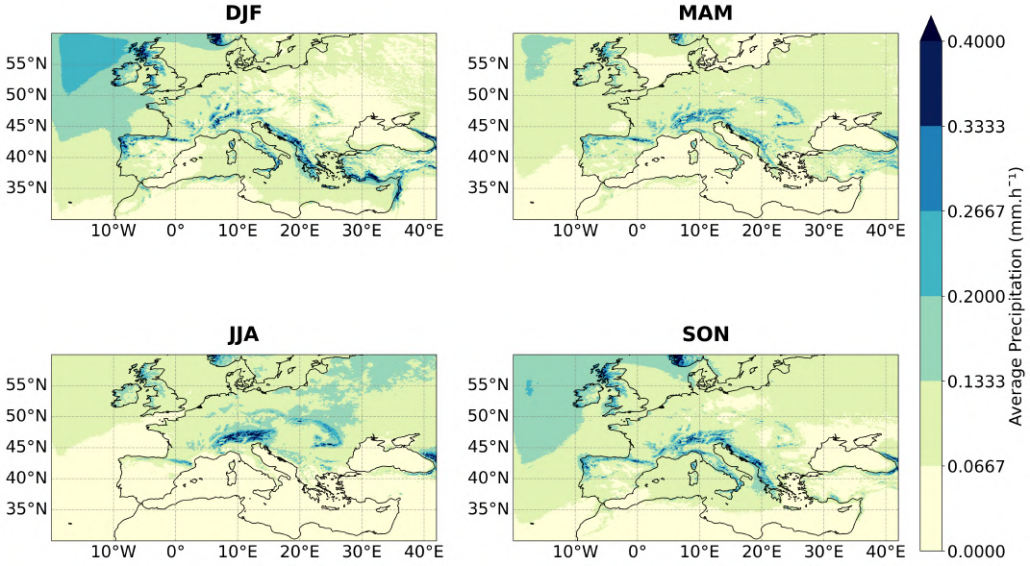

Fig. A.2 Seasonal climatology of hourly accumulated precipitation between 1981 and 2022.

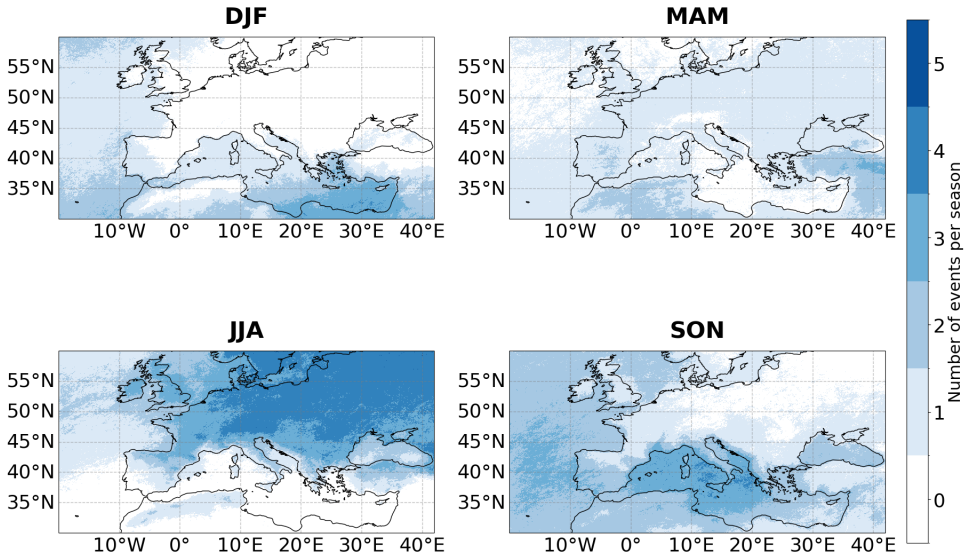

Fig. A.3 Season distribution of the 5h with the most intense extreme precipitation per year over the period 1981-2022 for each location.

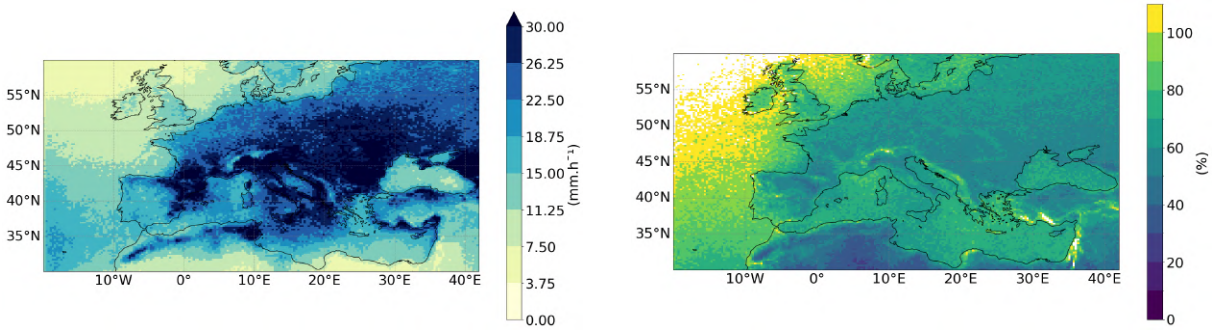

(a) Scaling with precipitation efficiency ε=1

(b) Precipitation efficiency ε

Fig. A.4 Left: Mean top-5 annual precipitation extremes scaling ($mm.h^{-1}$), averaged over the period 1981–2022. Right: fraction of the annual maximum precipitation (**fig. 3.3.a**) divided by the corresponding scaling (**sup. fig. A.4.a**). Data have been upscaled at 0.24° using a box average.

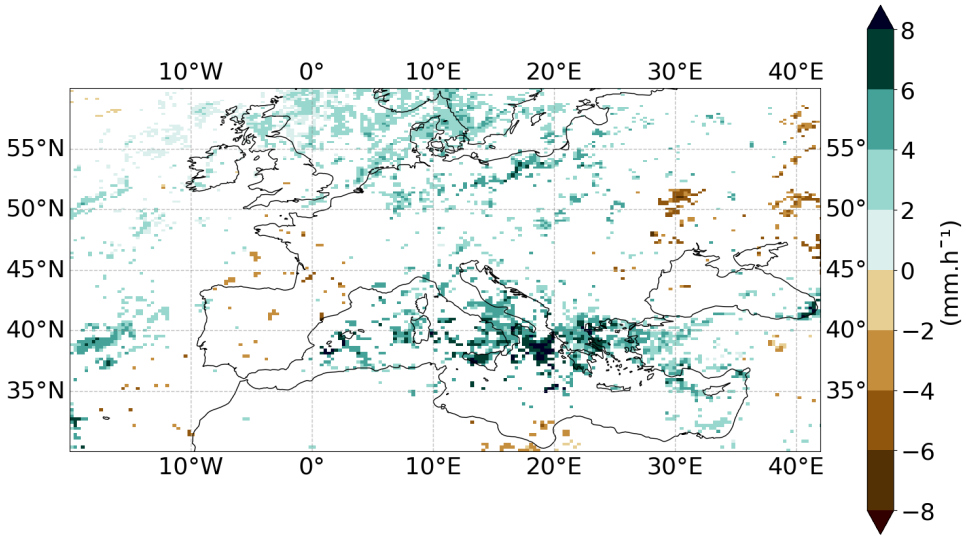

Fig. A.5 Like **fig. 3.4.a** but only trends statistically different from 0 are plotted.

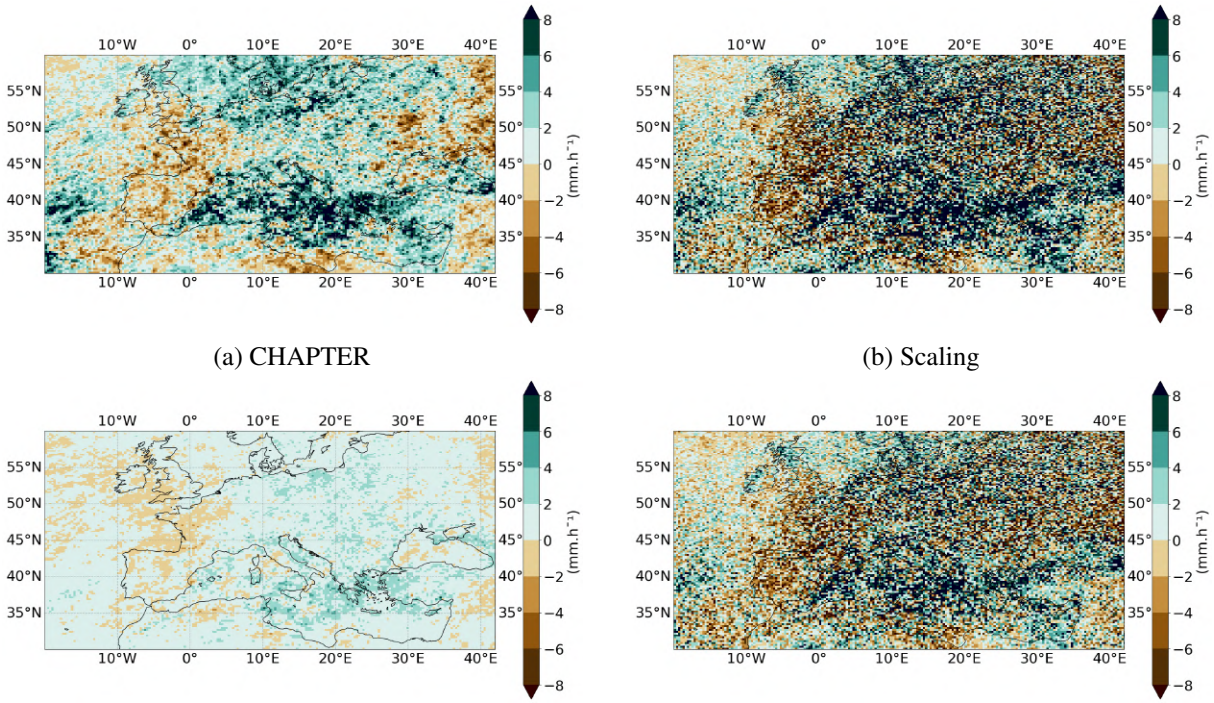

(a) CHAPTER

(b) Scaling

(c) Changes in thermodynamic scaling (omega constant).

(d) Changes in dynamic scaling (temperature constant).

Fig. A.6 Changes in maximum annual hourly precipitation (top, left), precipitation extremes scaling (top, right), the thermodynamic scaling (center, left), and the dynamic scaling (center, right), derived from a linear regression for the period 1981-2022. The unit is $mm.h^{-1}$. Data have been upscaled at 0.24° using a box average.

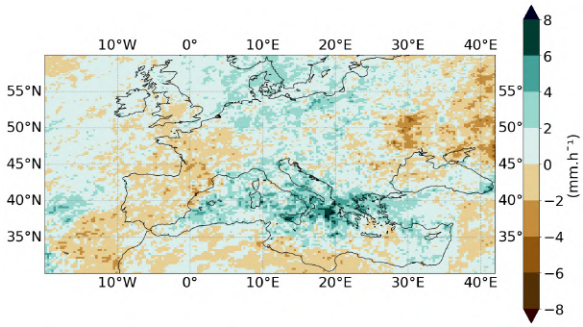

(a) CHAPTER

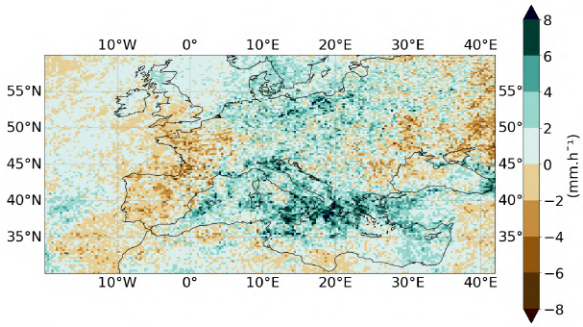

(b) Scaling

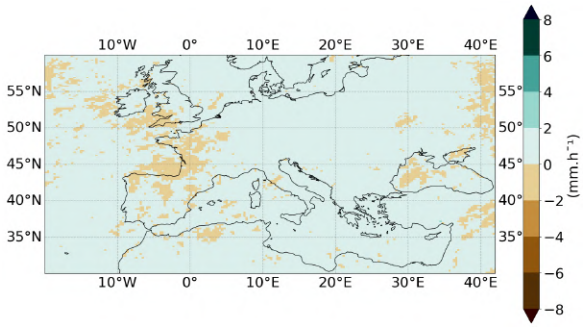

(c) Changes in thermodynamic scaling (omega constant).

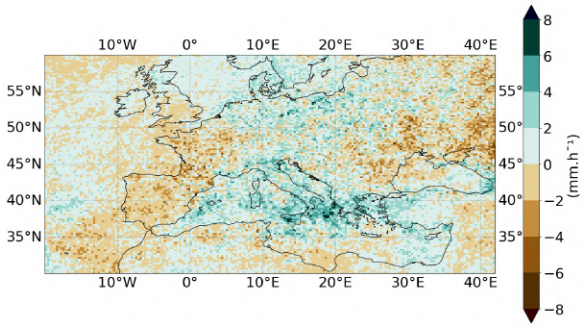

(d) Changes in dynamic scaling (temperature constant).

Fig. A.7 Changes in mean top-10 annual hourly precipitation (top, left), precipitation extremes scaling (top, right), the thermodynamic scaling (center, left), and the dynamic scaling (center, right), derived from a linear regression for the period 1981-2022. The unit is $mm.h^{-1}$. Data have been upscaled at 0.24° using a box average.

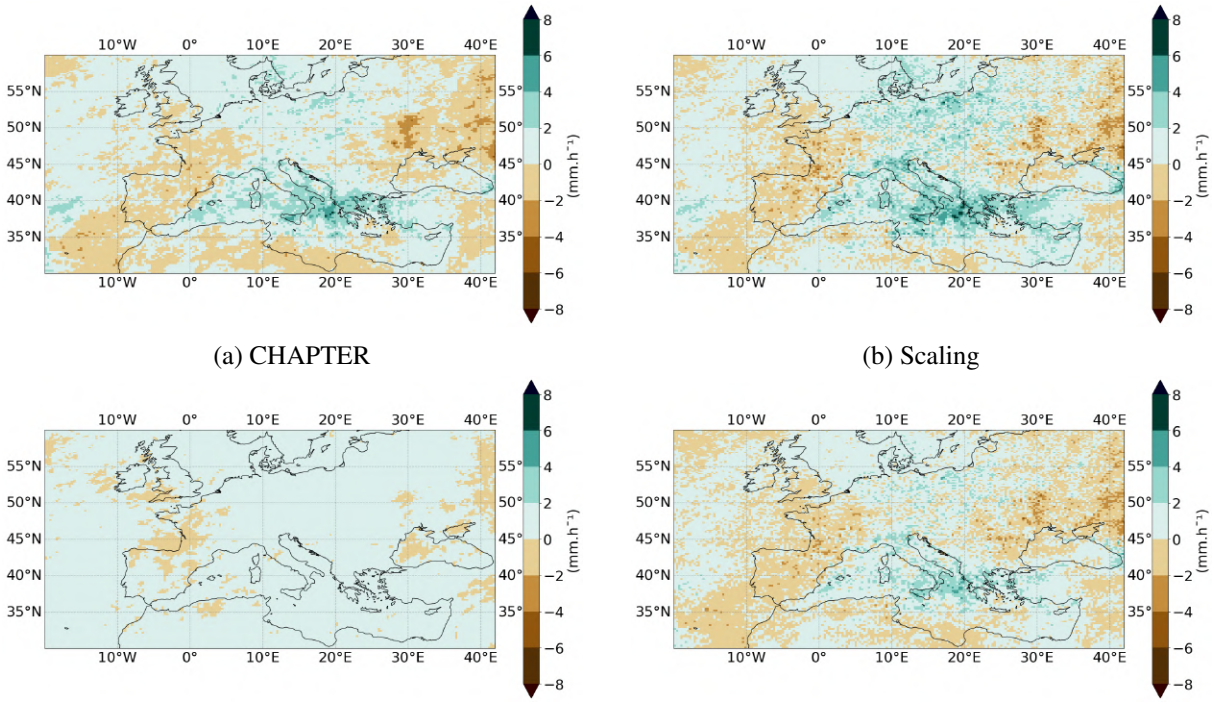

(a) CHAPTER

(b) Scaling

(c) Changes in thermodynamic scaling (omega constant).

(d) Changes in dynamic scaling (temperature constant).

Fig. A.8 Changes in mean top-20 annual hourly precipitation (top, left), precipitation extremes scaling (top, right), the thermodynamic scaling (center, left), and the dynamic scaling (center, right), derived from a linear regression for the period 1981-2022. The unit is $mm.h^{-1}$. Data have been upscaled at 0.24° using a box average.

	Model output	Scaling	Scaling w/ cnst W	Scaling w/ cnst T
Maximum Annual Hourly Precipitation				
Mean ($mm.hr^{-1}.y^{-1}$)	0.036	0.070	0.027	0.034
Spatial correlation	1	0.59	0.52	0.55
Mean top-5 annual hourly precipitation				
Mean ($mm.hr^{-1}.y^{-1}$)	0.022	0.045	0.017	0.021
Spatial correlation	1	0.73	0.58	0.70
Mean top-10 annual hourly precipitation				
Mean ($mm.hr^{-1}.y^{-1}$)	0.016	0.034	0.013	0.016
Spatial correlation	1	0.78	0.60	0.76
Mean top-20 annual hourly precipitation				
Mean ($mm.hr^{-1}.y^{-1}$)	0.010	0.025	0.009	0.010
Spatial correlation	1	0.82	0.62	0.82

Table A.1 Spatial mean and spatial correlation of the trends in precipitation output and the scaled precipitation over 1981-2022.

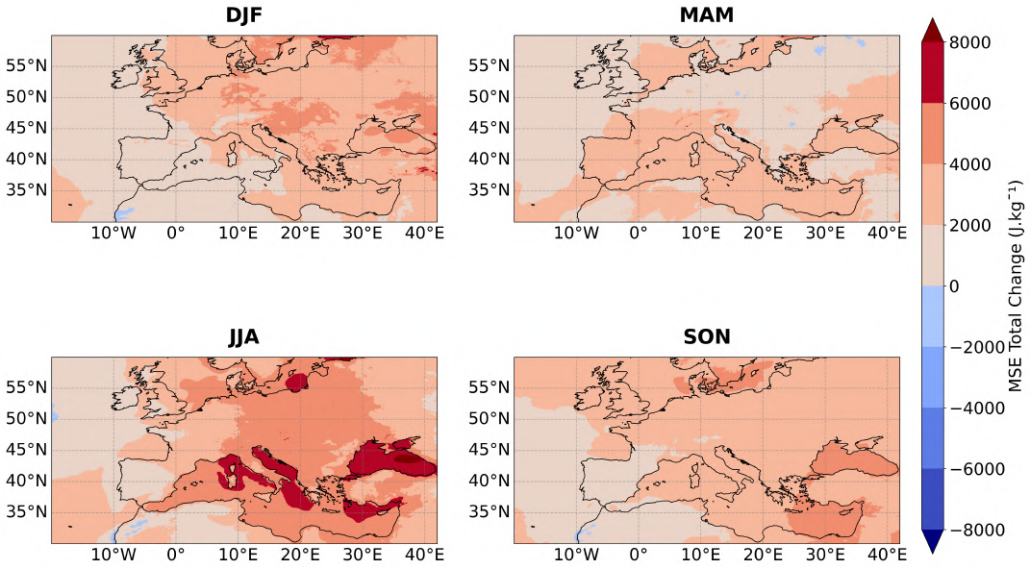

Fig. A.9 Seasonal total change of surface MSE between 1981 and 2022.

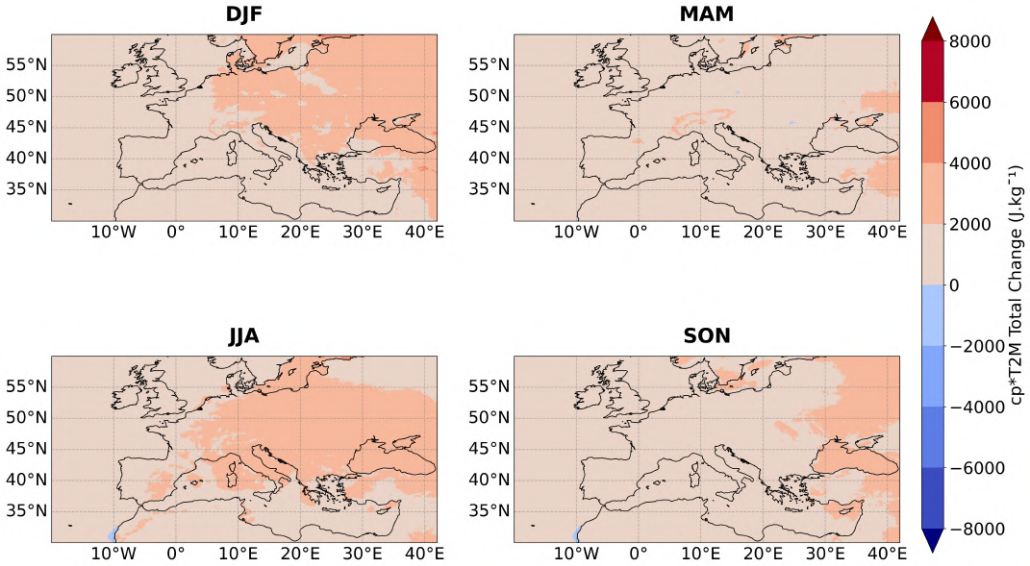

Fig. A.10 Seasonal total change of the temperature component of surface MSE ($c_p \times t_{2m}$) between 1981 and 2022.

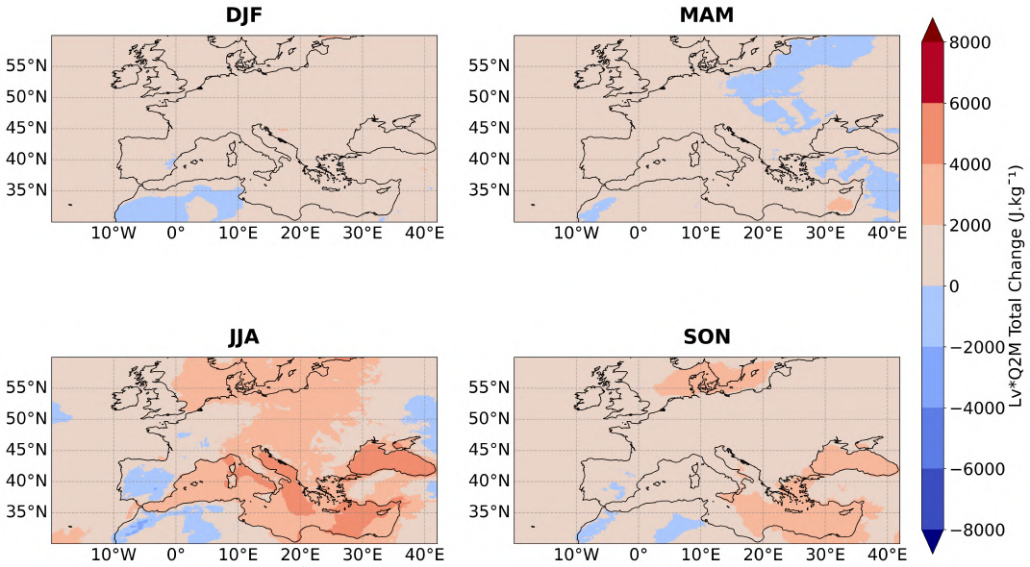

Fig. A.11 Seasonal total change of the specific humidity component of surface MSE ($L_v \times q_{2m}$) between 1981 and 2022.

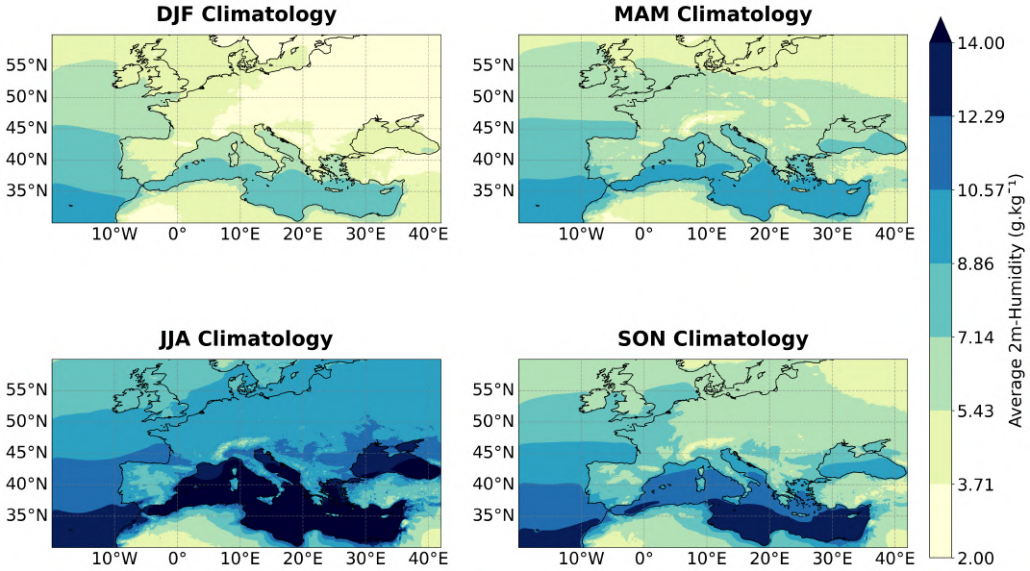

Fig. A.12 Seasonal climatology of 2m specific humidity between 1981 and 2022.

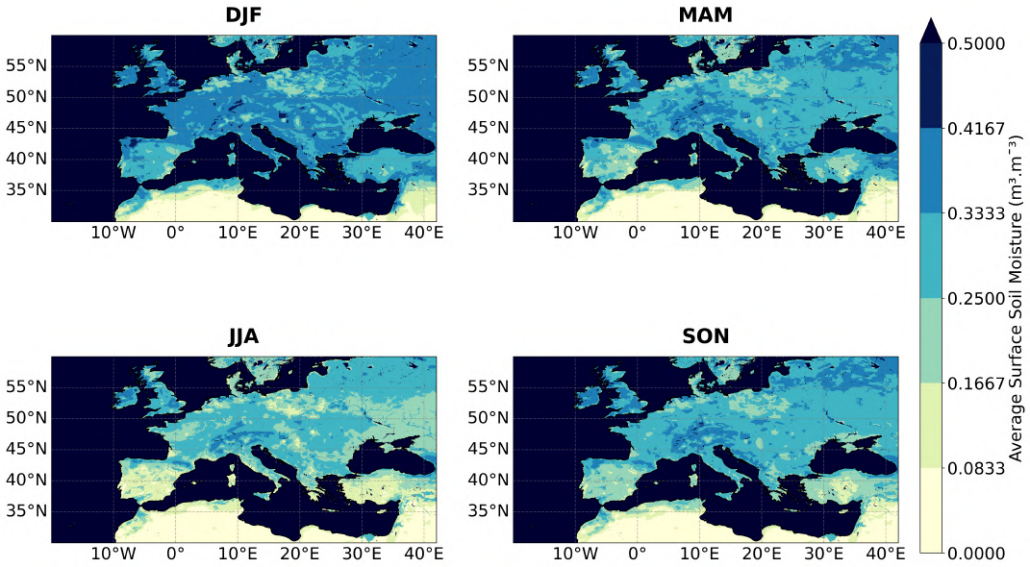

Fig. A.13 Seasonal climatology of the first-level soil moisture between 1981 and 2022.

Appendix B

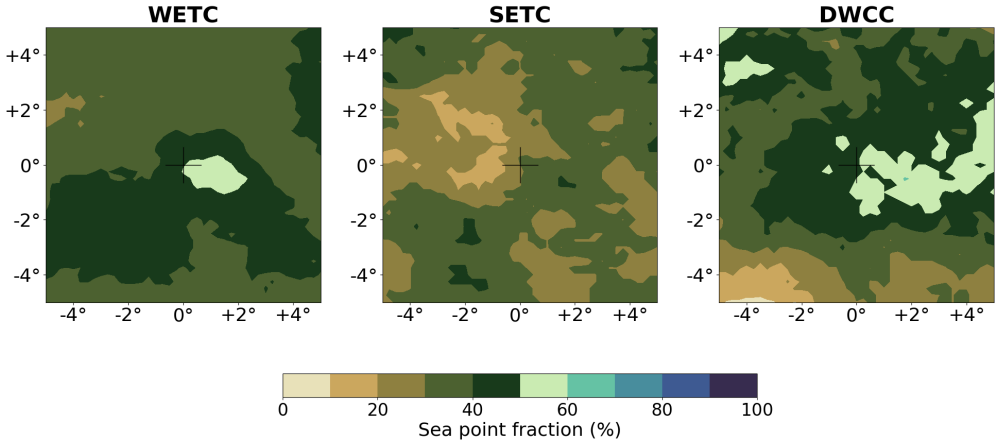

Fig. B.1 Fraction of cyclones' points over the sea 36h before the time of the minimum SLP.

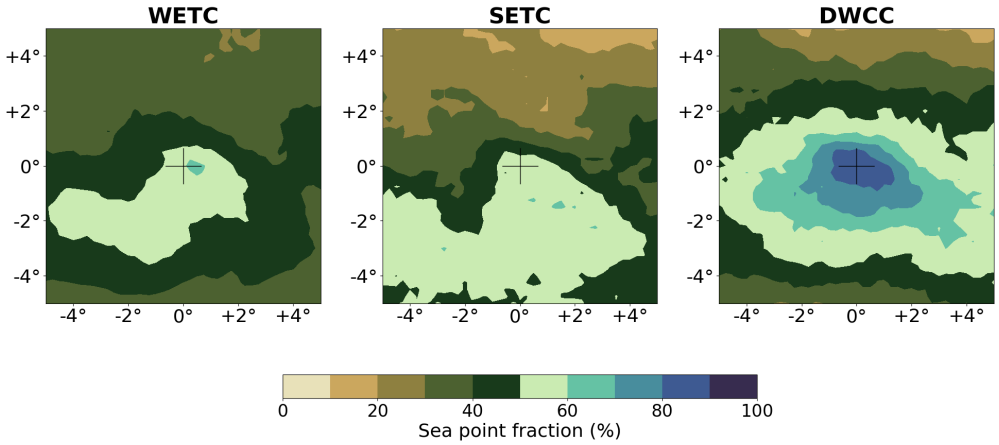

Fig. B.2 Fraction of cyclones' points over the sea at the time of the minimum SLP.

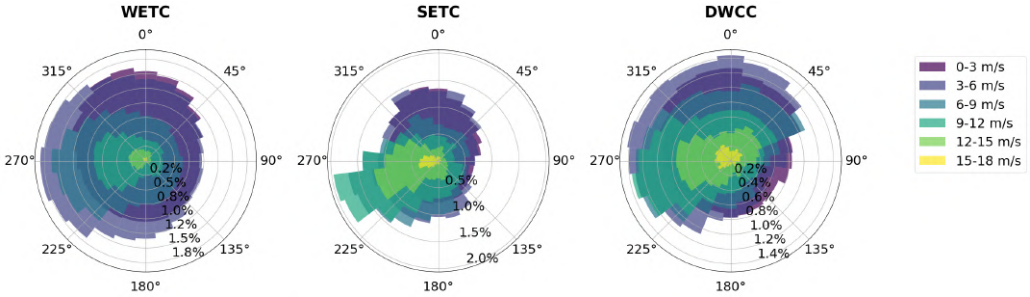

Fig. B.3 Wind rose at time of maximum cyclones' intensity for WETC (left), SETC (middle), and DWCC (right).

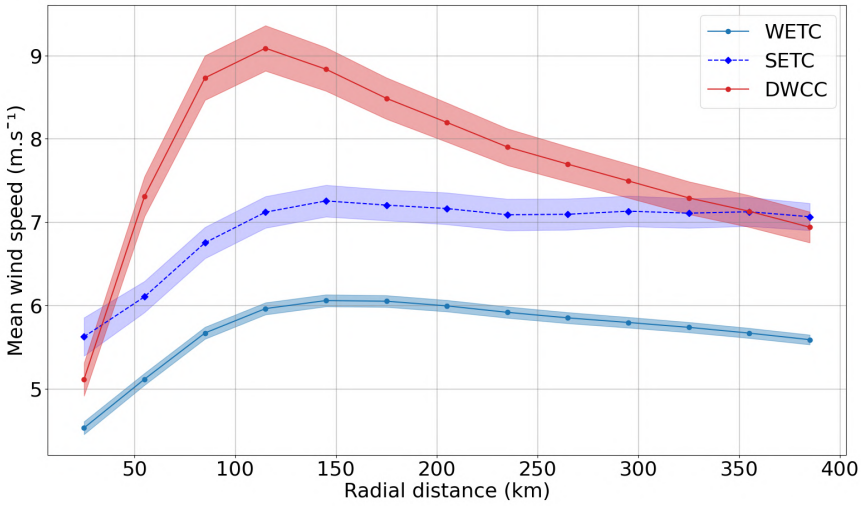

Fig. B.4 Azimuthally averaged wind speed at time of maximum cyclones intensity for WETC (light blue solid line), SETC (dark blue dashed line), and DWCC (red solid line). Shading around the solid line indicates the standard error of the mean.

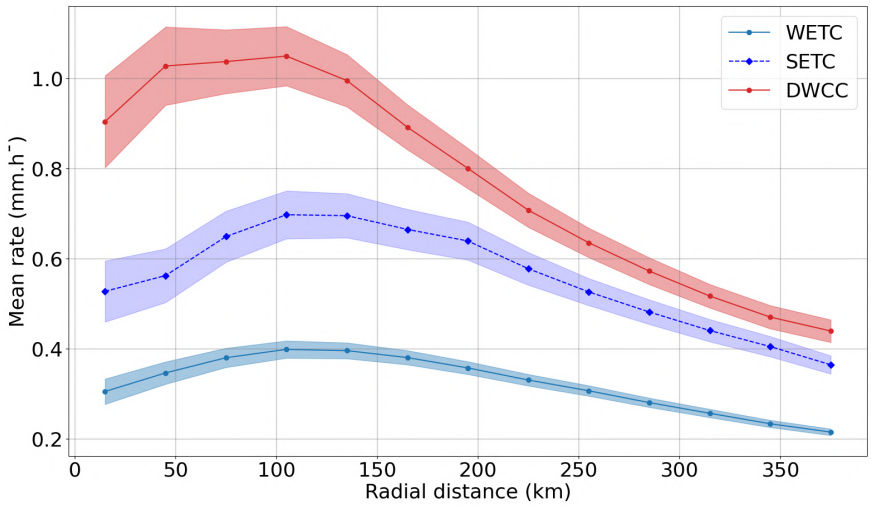

Fig. B.5 Azimuthally averaged precipitation at time of maximum cyclones intensity for WETC (light blue solid line), SETC (dark blue dashed line), and DWCC (red solid line). Shading around the solid line indicates the standard error of the mean.

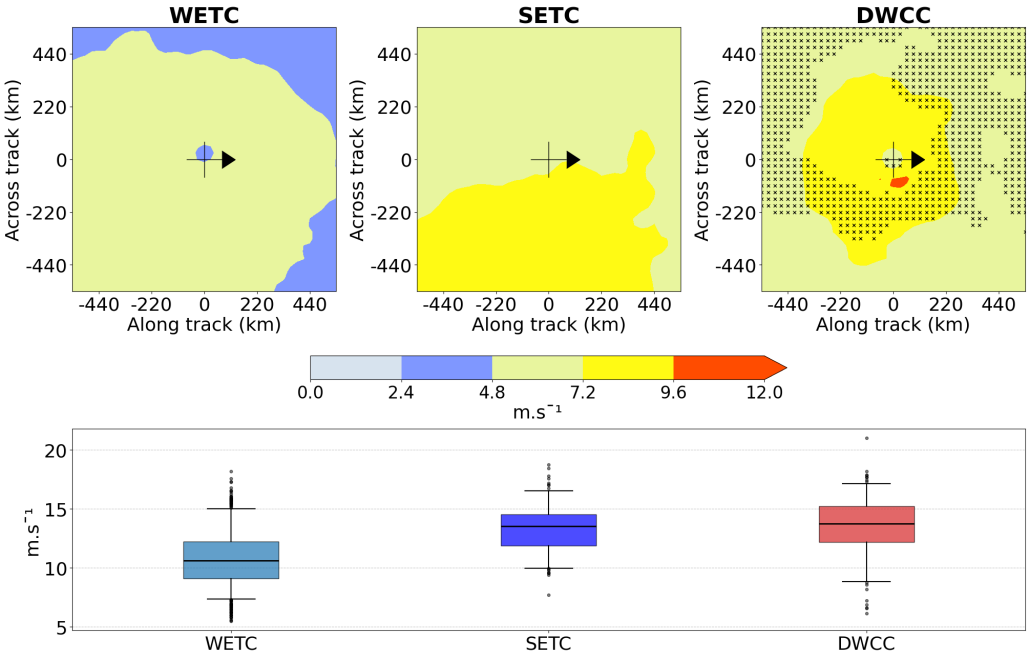

Fig. B.6 10m surface wind for the different cyclone classes. Top: 2D composites centered on the cyclone and oriented along the direction of propagation of the cyclones, at the time of minimum SLP. The markers in the right panel indicate regions where DWCC composited surface wind is not significantly different from SETC (95% confidence level). Bottom: boxplots of the mean surface wind for each cyclone, where the mean is computed on the 10% highest values over the 10°x10° box for each cyclone. Boxplots show the median value (horizontal line), the interquartile range (colored area), the 5th and 95th percentiles (whiskers), and outliers.

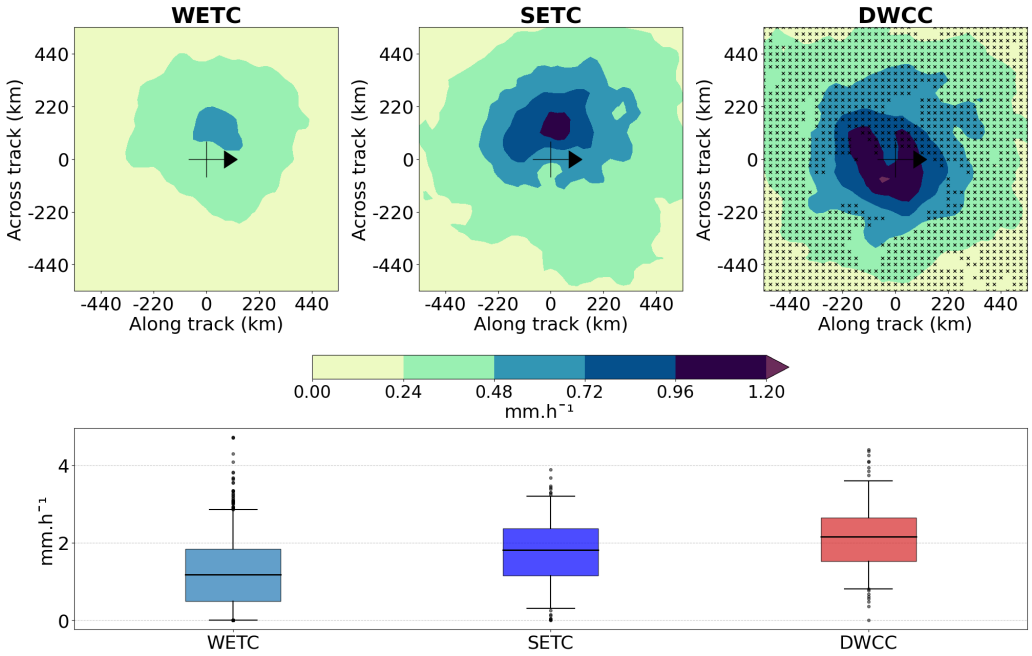

Fig. B.7 Hourly precipitation for the different cyclone classes. Top: 2D composites centered on the cyclones and oriented along the direction of propagation of the cyclones, at the time of minimum SLP. The markers in the right panel indicate regions where DWCC composited hourly precipitation is not significantly different from SETC (95% confidence level). Bottom: boxplots of the mean hourly precipitation for each cyclone, where the mean is computed on the 10% highest values over the 10°x10° box for each cyclone. Boxplots show the median value (horizontal line), the interquartile range (colored area), the 5th and 95th percentiles (whiskers), and outliers.

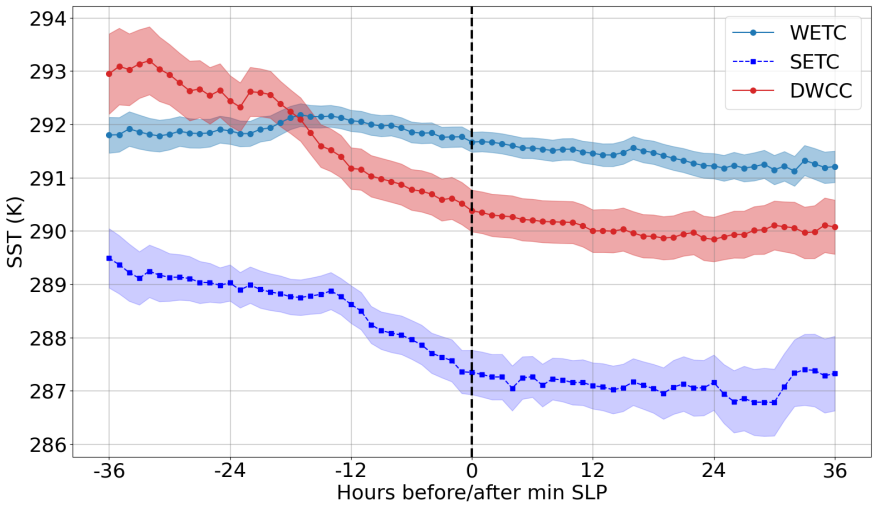

Fig. B.8 Composite time evolution of the mean SST for WETC (light blue solid line), SETC (dark blue dashed line), and DWCC (red solid line) with respect to their minimum SLP (black dashed line). The mean has been computed in a 4° by 4° box centered on each cyclone. Shading around the solid line indicates the standard error of the mean.

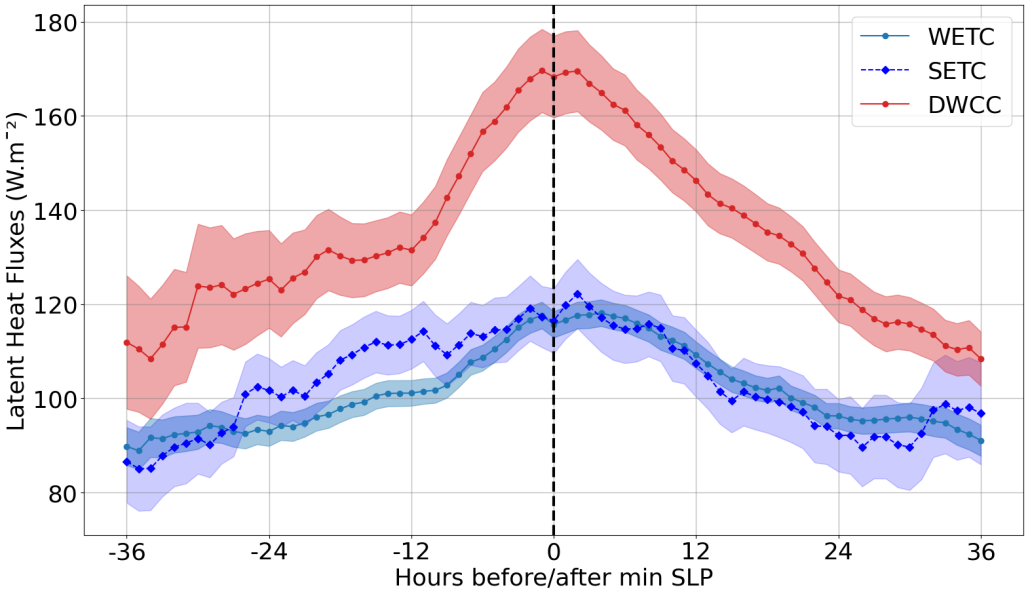

Fig. B.9 Composite time evolution of the mean air-sea latent heat flux for WETC (light blue solid line), SETC (dark blue dashed line), and DWCC (red solid line) with respect to their minimum SLP (black dashed line). The mean has been computed in a 4° by 4° box centered on each cyclone. Only the points over the sea are considered. Shading around the solid line indicates the standard error of the mean.

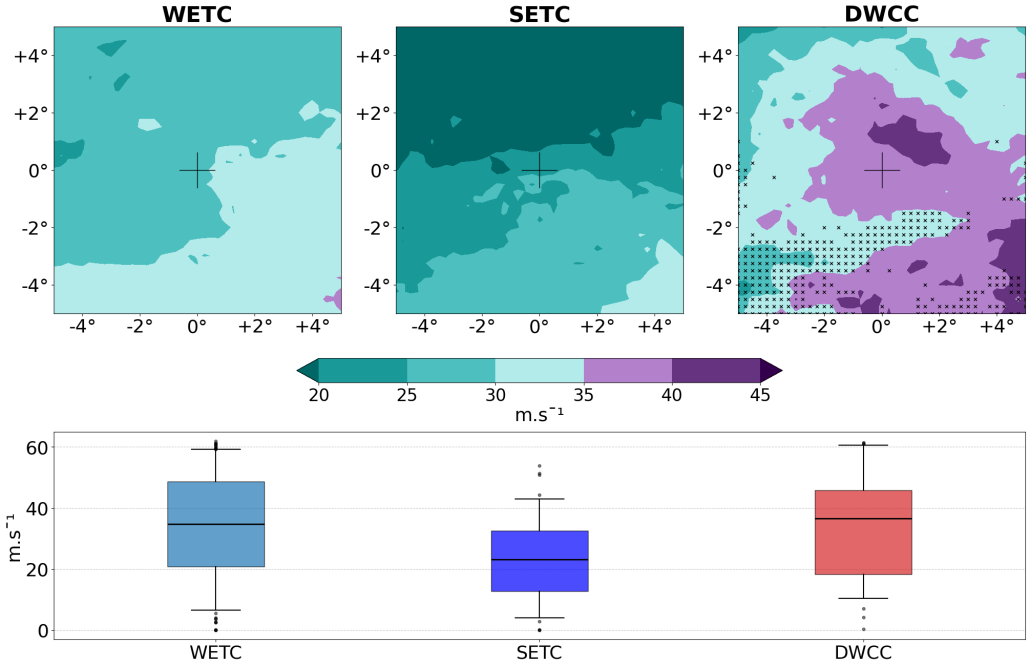

Fig. B.10 Climatological PI for the different cyclone classes. Top: 2D composites centered on the cyclones, 36h before the time of minimum SLP. The markers in the right panel indicate regions where DWCC composited climatological PI is not significantly different from SETC (95% confidence level). The purple colors represent values of PI above 35 $m\ s^{-1}$, value below which tropical cyclones typically don't form [6]. Bottom: boxplots of the mean climatological PI for each cyclone, where the mean is computed on the 10% highest values over the 10°x10° box for each cyclone. Boxplots show the median value (horizontal line), the interquartile range (colored area), the 5th and 95th percentiles (whiskers), and outliers.

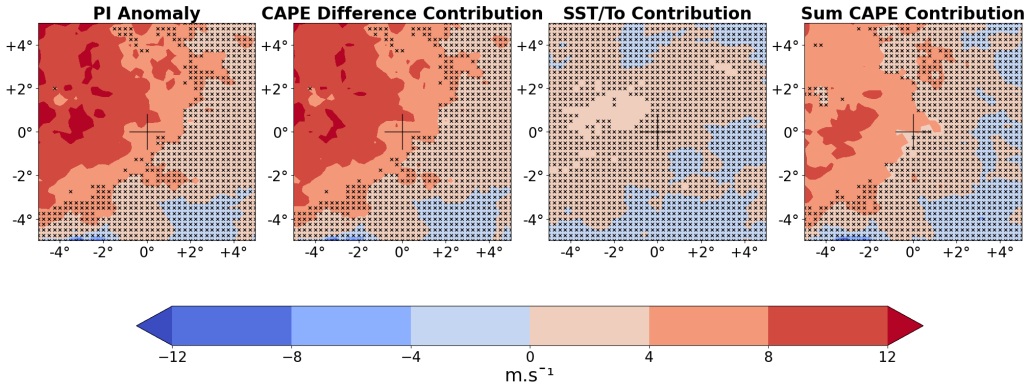

Fig. B.11 2D composites of PI anomalies ($m.s^{-1}$) for DWCC 36h before their minimum SLP. From the left: PI anomaly as the difference between the actual PI (**fig. 4.10**) and the climatological PI (**sup. fig. B.10**); difference between the PI computed with all climatological values but the actual difference in CAPE and the climatological PI; difference between the PI computed with all climatological values but the actual efficiency factor ($\frac{SST}{T_o}$) and the climatological PI; sum of the contributions to the anomaly created by the CAPE difference presented in **fig. 4.11**. The difference between the second and the fourth subplots shows the non-linearities at play in the total contribution of the CAPE difference to the final PI anomaly. The markers indicate the anomalies that are not significantly different from 0 at a 95% confidence level.

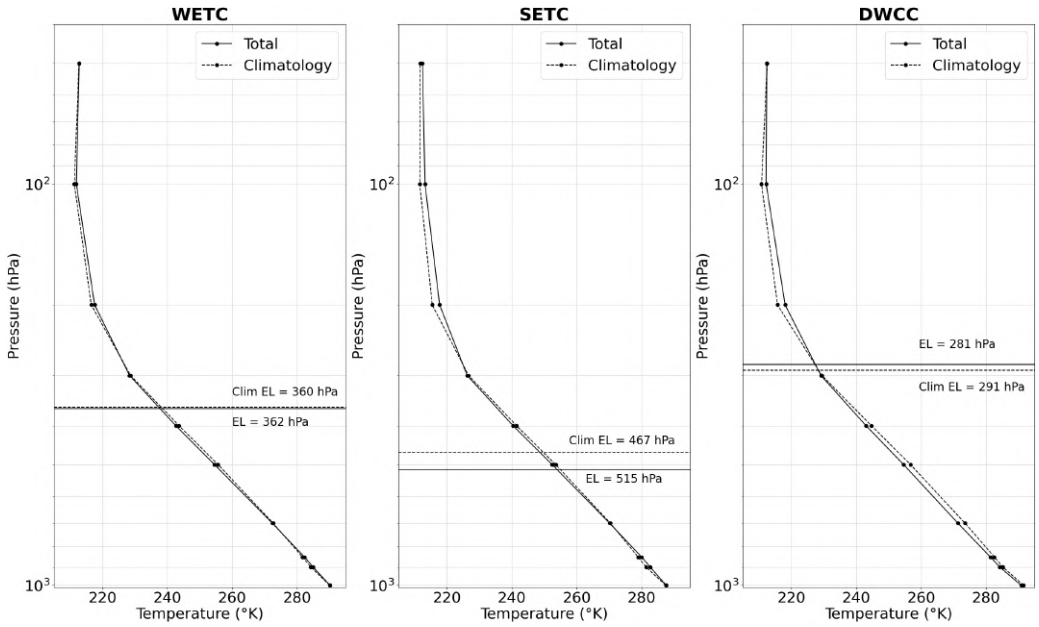

Fig. B.12 Temperature profiles 36h before the time of minimum SLP. The value is the mean temperature over a 10° by 10° box centered on the cyclone, but only the points over the sea are considered. The equilibrium level (EL) averaged over the same box is also indicated. For all variables, dashed lines correspond to climatological values and full lines indicate the actual values emerging from the composites. It can be appreciated how DWCC present the biggest anomaly in mid-tropospheric temperatures, compared to WETC and SETC.

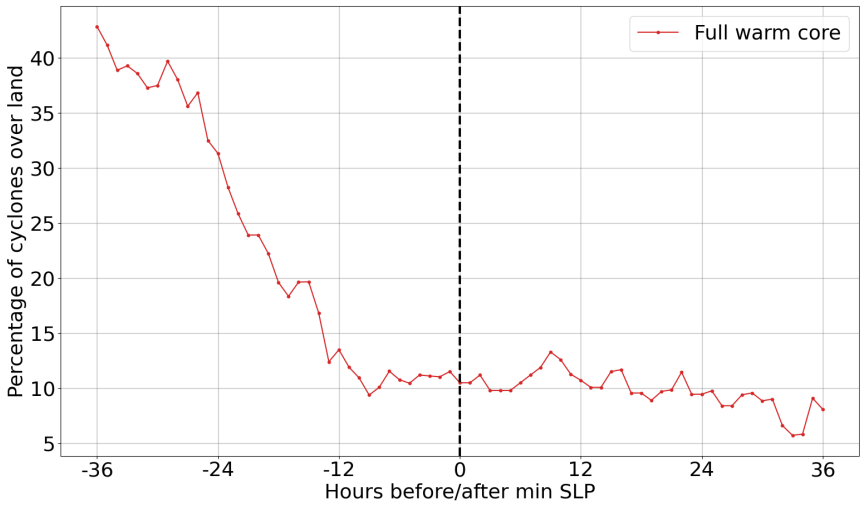

Fig. B.13 Time evolution of the percentage of cyclones over land with respect to time of minimum SLP (black dashed line).

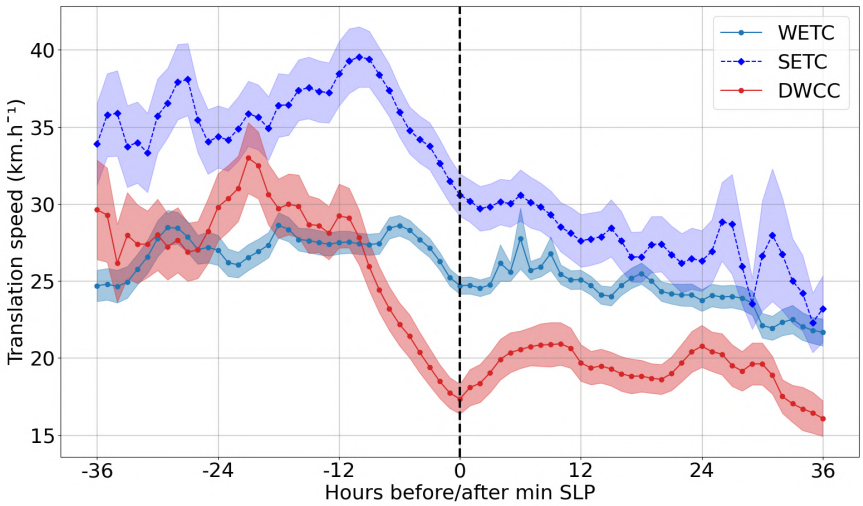

Fig. B.14 Composite time evolution of the translation speed for WETC (light blue solid line), SETC (dark blue dashed line), and DWCC (red solid line) with respect to their minimum SLP (black dashed line). Shading around the solid line indicates the standard error of the mean.

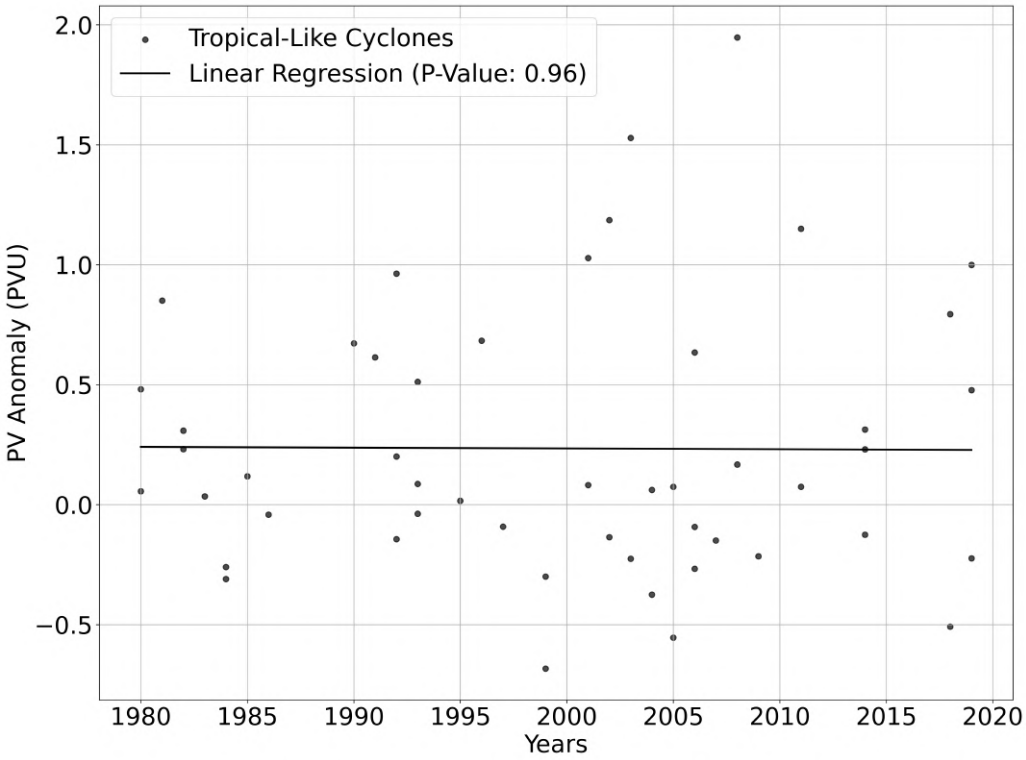

Fig. B.15 Time series of the PV anomaly average computed in a 4° by 4° box centered on each IETC, 36h before their minimum SLP.